TÉCNICO LISBOA

Review and simulation of the electrochemical response of cobalt hydroxide electrodes for energy storage

Gabriel Garcia Carvalho

Thesis to obtain the Master of Science Degree in

Chemical Engineering

Supervisors: Prof. Maria de Fátima Grilo da Costa Montemor

Prof. Maria Teresa Oliveira de Moura e Silva

Examination Committee

Chairperson: Teresa Duarte (DEQ)

Jury: Fátima Montemor (DEQ)

Jury: Sónia Eugénio (C2C-NewCap)

21 January 2021

I declare that this document is an original work of my own authorship and that it fulfils all the requirements of the Code of Conduct and Good Practices of the *Universidade de Lisboa*

Acknowledgments

I would like thank my supervisors Professor Fátima Montemor and Professor Maria Teresa Moura e Silva for accompanying, guiding, and supporting me throughout my work, indulging me with their knowledge in the exciting and promising research field that is energy storage.

I would also like to express my gratitude to Dr. Alberto Adán Más who kindly assisted me with his experience, and all of my lab colleagues who I shared great moments with.

Finally, this work would have not been possible if it wasn't for the love and support of my parents who provided me the resources to study in a school of excellence such as the Instituto Superior Técnico.

Abstract

The pseudocapacitive mechanisms related to cobalt hydroxide nanofoams have been studied within the scope of supercapacitors' use for energy storage. A comprehensive review has been conducted highlighting the positioning and evolution of electrochemical systems, focusing in the materials and major working principles of devices such as dielectric capacitors, electrolytic capacitors, and supercapacitors (under which EDLCs and pseudocapacitors are included). To further understand the application and functionalization of cobalt hydroxide nanofoams, a review about 3D electrode architectures was made, exposing the most important parameters and operating conditions related to the purpose, synthesis, and use of these nanostructures. Additionally, a computational MATLAB simulation was developed towards understanding the mathematical theoretical models present in literature that best define the electrochemical response of pseudocapacitive materials, further promoting the knowledge about pseudocapacitors and their placement in the electrochemical energy storage field.

Resumo

Os mecanismos pseudocapacitivos relacionados a nanoespumas de hidróxido de cobalto foram estudados no âmbito do uso de supercondensadores para armazenamento de energia. Foi conduzida uma revisão compreensiva da literatura, destacando o posicionamento e evolução de dispositivos eletroquímicos, com foco nos materiais e principais princípios de funcionamento de dispositivos como condensadores dielétricos, condensadores eletrolíticos e supercondensadores (*EDLCs* e pseudocondensadores). De modo a melhor entender a aplicação e funcionalização de nanoespumas de hidróxido de cobalto, foi realizada uma revisão sobre estruturas 3D de elétrodos, realçando os parâmetros e condições operatórias mais importantes relacionadas com o propósito, a síntese, e o uso destas nano-estruturas. Além disso, uma simulação computacional foi desenvolvida em MATLAB no sentido de compreender os modelos teóricos presentes na literatura que melhor definem a resposta eletroquímica de materiais pseudocapacitativos, promovendo o conhecimento sobre pseudocondensadores e a sua importância no campo de investigação de armazenamento de energia na eletroquímica.

Index

List of Figures

List of Variables

Q	C	Charge
ΔQ	C	Stored charge
C	F	Capacitance
Ψ	V	Potential
ΔΨ	V	Potential window
ε_0	-	Relative permittivity of vacuum
ε_r	-	Relative permittivity of a dielectric material
S	m^2	Electrode surface area
b	m	Dielectric thickness
p	-	Probability of Boltzmann distribution
E	J	Energy
k	$m^2\ kg\ s^{-2}\ K^{-1}$	Boltzmann constant
T	K	Temperature
n_i	M	Molar concentration of component i
n_0	M	Molar bulk concentration
x	m	Distance from electrode surface
z_i	-	Valency of component i
e	C	Charge of a proton
ρ_i	$C\ m^{-2}$	Charge density of component i
L	m	Pore depth
A	m	Inner pore radius
A_0	m	Ion's radius
B	m	Outer pore radius
d	m	Distance of counterions to electrode surface
m	g	Generated mass at electrode
M	$mol\ g^{-1}$	Molar mass
F	$C\ mol^{-1}$	Faraday's constant

List of Acronyms

IEA	International Energy Agency
DHC	District heating and cooling
EC	Electrochemical capacitor
EDLC	Electrochemical double layer capacitor
EDL	Electrochemical double layer
CV	Cyclic voltammetry
AAO	Anodic aluminium oxide
IHP	Inner Helmholtz plane
OHP	Outer Helmholtz plane
AC	Activated carbon
CDC	Carbide derived carbon
CNT	Carbon nanotubes
SWCNT	Single-wall carbon nanotubes
MWCNT	Multi-wall carbon nanotubes
CDV	Chemical vapor deposition
TMO	Transition metal oxide
MOH	Metal oxide/hydroxide
MO	Metal oxide
MH	Metal hydroxide
DHBT	Dynamic hydrogen bubble template
OER	Oxygen evolution reaction

1. Introduction

1.1. Overview

World population has been growing every year as economic growth and better life standards continue to increase. Energy demand presses the world towards smarter cities and efficient energy supply systems which steadily face greener and more renewable alternatives rather than the conventional fossil counterparts. With the exciting potential and increasing domination of renewable energy sources, the management of the available produced energy becomes a greater challenge due to their intermittent nature, thus limiting the scope of their use. Once answered by storing wood logs and now by storing electrons, this challenge can only be addressed with highly efficient storage systems that prevent needless wastes of energy while opening the door to a wider array of future applications.

Energy storage has been growing worldwide with the creation of market incentives clearing the way for its expansion. More than ever, the energy demand is present in our everyday life, focusing in the small devices and technologies the world has grown dependent on. The pace for technology will not slowdown. Faster cell phones and computers will be made. Cars will be electrified. Smart cities will expand, and communications will improve. The production of energy will grow and the demand for fast and efficient ways to store it will continue to follow.

1.2. The need for energy storage

By 2018, behind-the-meter storage deployment had doubled compared to the latter year, considerably overtaking the grid-scale applications. Energy consumers are increasingly investing in systems deployed closer to them and within a higher control. Increasing proximity and access to storage technologies allows the better management of the energy at a much faster rate than the rate at which the grid-scale deployment is evolving (Figure 1).

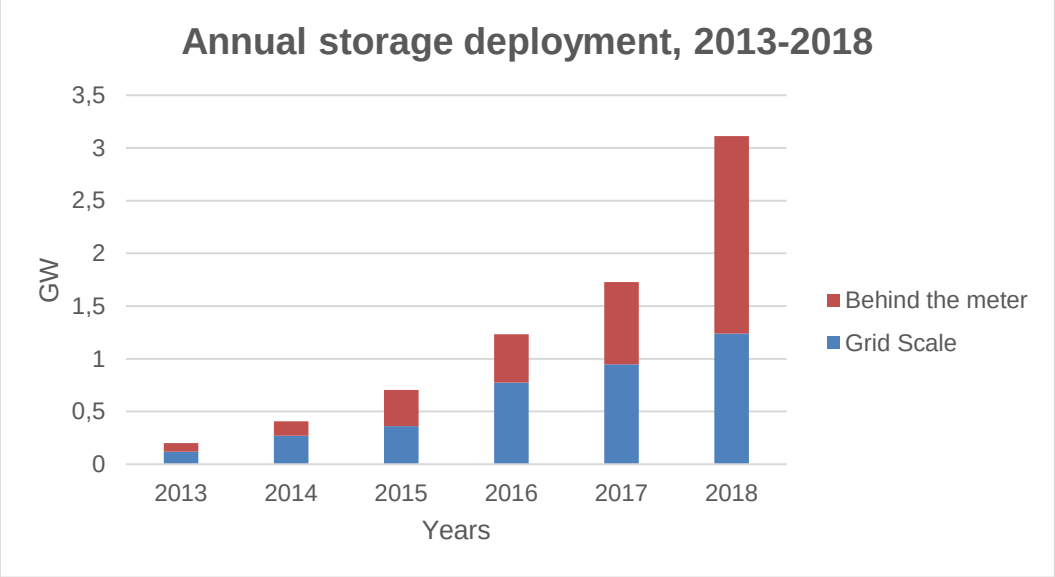

Figure 1 - IEA, Annual storage deployment, 2013-2018, IEA, Paris [1]

The growing worldwide capacity reflects in the ongoing investment of renewable energy sources with accompanying decreasing costs of operation and deployment, creating room for the further expansion of storage technologies. Investment in renewable power sources has increased past fossil fuels since 2006. After 2011, global investment has somewhat stabilized with ups and downs in the power sector due to related government policy changes. Nevertheless, the investment in renewables clearly surpasses the fossil counterparts and further statistical evidence supports that claim for the next years [2]. Following the conclusions made by the International Energy Agency (IEA), the growth of renewables can be seen stalling at first glance (Figure 2a). However, energy capacity today is less expensive than it was in the past, therefore, by normalizing the costs of renewables to the established costs of 2018, a considerable growth can be observed from 2010 to 2018 (Figure 2b).

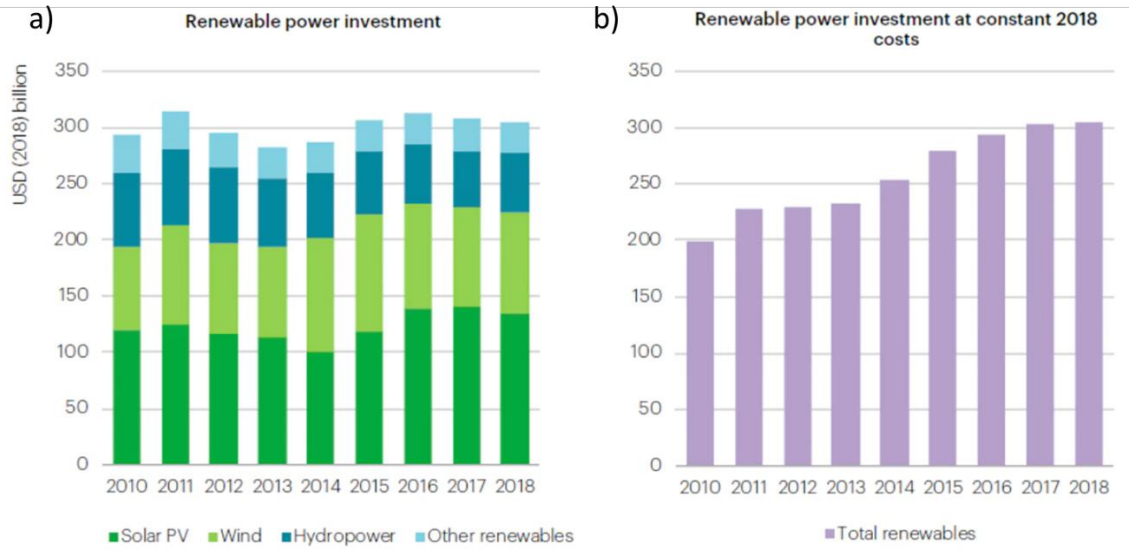

Figure 2 - Investment in renewables a) Renewable power investment, b) at 2018 costs (3)

To further support the argument of increasing dominance of renewable power sources over fossil fuel systems, by looking at the general evolution of capital costs of these technologies, and using 2010 as a starting base, with the exception of hydropower, renewables have overall evolved to be the best investment bets as their costs decrease while fossil fuels oscillate over horizontal asymptotes (Figure 3).

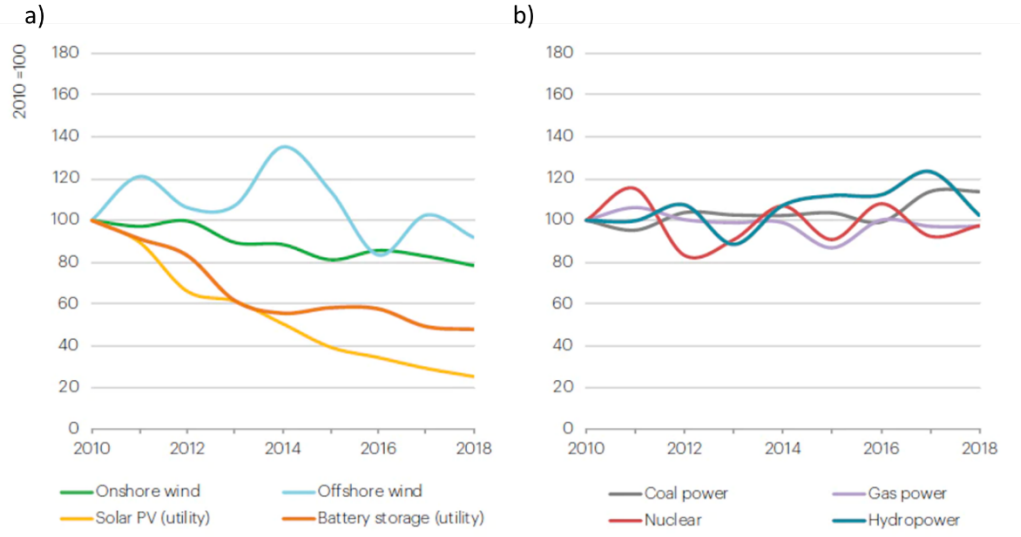

Figure 3 - Change in global average capital costs for newly commissioned power capacity (4)

With this data, it is clear that the energy transition conveniently points to the continuous growth of both renewable energy sources and the increasing need of efficient energy storage systems. In the next

section of this work an overall panorama of the most well-known modern energy storage systems will be further elaborated.

1.3. Energy storage methods

Energy storage systems can be categorized in chemical, electrical, electrochemical, mechanical, and thermal (Figure 4). Each method stores energy under different principles, respectively applied according to their operating conditions which results in their deployment in different situations.

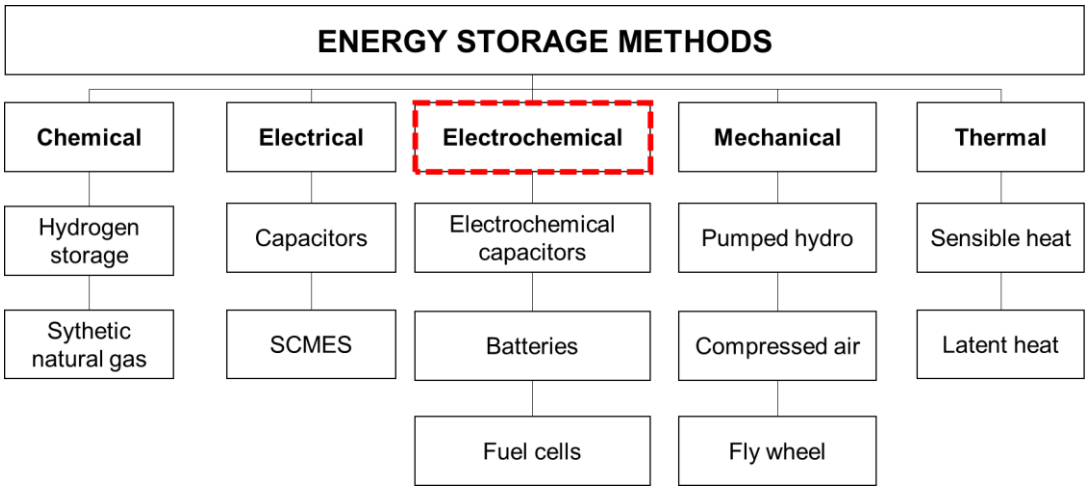

Figure 4 - Classification of energy storage methods

1.3.1. Mechanical

Mechanical energy storage takes advantage of the kinetic and potential energy of solids and fluids to use the physical forces applied to them (like gravity or decompression) as basic working principles of charge and discharge. These systems are often associated with machines of many moving parts which require periodic maintenance to prevent the occurrence of possible damages and material degradation at short and long terms. In addition, mechanical systems are usually deployed in medium to large-scale dimensions, limiting their application to the proportional energy consumers. The most dominant mechanical storage technology is pumped hydro (also referred to as hydropower), consisting in the most significant method of energy storage in world, making up 96,2% of the worldwide storage capacity [(5)]. Its moving parts are few and limited to the turbines and pumps used in the water charge and discharge processes. Hydropower is a prime example of the scale that mechanical systems can successfully reach.

1.3.2. Thermal

Thermal energy storage saves energy in the form of heat, making use of the heat transfer phenomena to store and release the heat when necessary. This energy can take the form of sensible heat (changes in temperature, and thus, in the energy state) or latent heat (phase transformations that

involve greater amounts of heat transfer at constant temperature). These are ingenious systems used in house ambient and district heating and cooling applications (DHC) that go as far as supplying energy to entire villages and cities. Thermal energy storage is highly limited by the materials that are used as mediums of heat transfer. These materials degrade and lose thermal conduction properties over time. Therefore, the optimization and choosing of the heat transfer materials is often the fundamental factor for the efficient application of thermal energy systems.

1.3.3. Electrical

Electrical systems store energy in the form of electricity by manipulating the flow of charged particles in ionic fluids between the electrodes of a capacitor or through magnetic shifts in superconducting magnets. Due to the inherently low energy capacity of these electrical devices, their applications usually extend to small-scale dimensions and are accompanied with other energy storage devices with higher energy density. Nevertheless, these systems are among the most high-power systems in energy storage due to their incredible fast rates of charge and discharge, such is the case of capacitors which will be further explored in the upcoming sections of this work.

1.3.4. Chemical

Chemical energy storage systems store energy with endothermic reactions and discharge the respective energy with reversible exothermic reactions. In the great majority of cases, this charge/discharge system translates in the dissociation of a chemical compound followed by its respective synthesis. Chemical systems are very pertinent for long-term energy storage applications due to having almost no loss of energy throughout the storing period which is a consequent advantage of the fact of the energy being stored by the formation of chemical compounds that will not acquire or release energy unless put in the convenient conditions for the endothermic/exothermic reactions that create/break those important chemical bonds.

1.3.5. Electrochemical

Electrochemical energy storage systems, just like the name indicates, combine electrical and chemical processes that involve electrochemical reactions with electron transfer through conducting electrodes to store the energy. Unlike capacitors, electrochemical systems require an electrolyte and rely on redox reactions occurring in the bulk or at the surface of an electrode which depends on the application and the type of the device. These devices include batteries, ultra-batteries, and redox-based supercapacitors. It is extremely relevant for this work to fully understand the functioning of batteries and redox supercapacitors in order to acknowledge the advantages and disadvantages of each when it comes to develop highly versatile, powerful, and energetic electrochemical devices.

1.4. Electrochemical capacitors

1.4.1. Overview

Electrochemical capacitors (ECs), otherwise known as supercapacitors or ultracapacitors, are the strategic establishment of a complementary response between high-energy (batteries) and high-power density devices (capacitors). Neither batteries or capacitors are able to provide simultaneously large yields of energy while maintaining fast rates of charge and discharge. Conventional batteries can reach energy capacities around 100 Wh/kg, greatly surpassing conventional capacitors, but display much lower power density. Therefore, these two classes of devices are specialized in complementary applications where either energy or power densities are of utmost importance, batteries typically being used to store high quantities of energy while capacitors fill the needs in terms of power requirements. Nevertheless, a gap is left in the array of electrochemical applications as the two referenced extremes dominate the electrochemical energy storage field. This gap opens several investigation opportunities to create solutions between the battery and conventional capacitors. This raised the interest on different devices assemblies, included in the ECs family: the redox supercapacitor, the pseudocapacitors, the electrochemical double layer supercapacitors (EDLCs) and the hybrid devices (combine a battery type electrode with a supercapacitor type electrode) that can potentially translate into more versatile systems with increased energy density while providing good power capacity (Figure 5).

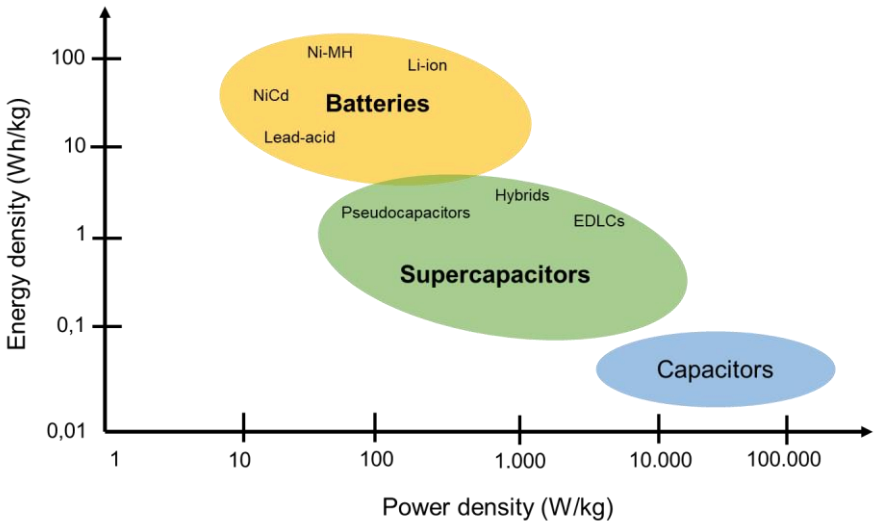

Figure 5 - Ragone plot of power and energy densities of energy storage devices

1.4.2. Work objectives

The perfect electrochemical energy storage device would be the one with very high energy and power densities with optimal parameters such as high operating lives and being constituted by environmentally friendly materials in compact architectures, exploring the best features of batteries and capacitors. This

research field is still evolving and there are important gaps of knowledge to be filled, namely in what concerns the type of materials and prediction of these devices' response. This dissertation intends to provide a contribution to this important knowledge gap.

ECs can be viewed from different perspectives which depend on the device's assembly. Although hybrid devices are commonly referred to as supercapacitors, some authors [6] make pertinent distinctions when the behaviour is closer to the capacitor-like (the conventional electrochemical double layer - EDL) or to the battery-like behaviours, going as far as naming them as *supercapacitors* or *supercapattery*, respectively. This distinction limits the scope of the *supercapacitor* notion to the ones that are closer to the conventional EDL device.

ECs, and in particular pseudocapacitors, are widely studied not only for the fact they are ruled by different capacitance-inducing mechanisms but also due to their high-capacitance resulting from fast reversible redox reactions, further bridging the simple physical capacitance of pure EDLCs with the redox chemical processes that were traditionally associated to batteries. In short, understanding ECs is of upmost importance as they pose complex electrochemical responses amongst the systems for high power applications in energy storage. Depending on the charge storage mechanisms, ECs can be further divided in different types of systems which will be further elaborated in the next chapter – *State of the art* of supercapacitors. Studying the relationships and models that govern these highly capacitive devices has raised the relevance of different critical parameters, such as diffusion coefficients and porosity densities, which determine the electrochemical performance of the device. Furthermore, this understanding contributes to the efficient and sustaining optimization of ECs.

The intention of this work is to deliver an extensive *state of the art* about supercapacitors to further improve the theoretical and practical knowledge for electrochemical energy storage. Furthermore, special focus is given to the production and functionalization of pseudocapacitive nanofoam structures made of cobalt hydroxide. The work intends to better comprehend the routes for production of these materials and the mechanism governing their electrochemical response, by reviewing the current literature and conducting computational simulations (with MATLAB software) to predict the electrochemical response of this system.

2. State of the art: from capacitors to supercapacitors

2.1. Dielectric capacitors

2.1.1. Overview

The most conventional and simple capacitors are the dielectric capacitors which are often named according to the dielectric they are composed of (e.g. vacuum, glass, ceramic, and film capacitors). The assembly of dielectric capacitors consists of two metal electrodes (i.e. polarized or non-polarized, depending on the application) with surfaces opposite to each other, pressing the dielectric material between them. The electrodes are connected externally by a circuit that provides the energy source during charge and receives the stored energy throughout discharge, when the process is reversed. The dielectric is a material with polarizable molecules that face the charged electrodes with respective opposite charges. It is crucial for the dielectric to be an efficient insulator so no current flows through the media, staying stored electrostatically in the electrode's surface [7].

The use of dielectric capacitors date to the 18th century when the storage effect was accidentally discovered by Ewald Georg von Kleist. The German physicist touched a wire immersed inside a glass jar of water which he held with his hand. Upon touching the wire, he received a powerful shock, experiencing first-hand the effect of a fully charged dielectric capacitor. What von Kleist did not realize before being shocked, was that the glass jar acted as a dielectric material while the water and his hand acted as conductors. By touching the wire, the physicist had closed the external circuit between the water and his hand holding the jar which discharged the static current that was presently stored. Later, Pieter van Musschenbroek created a device, based on the phenomenon discovered by von Kleist, named as Leiden Jar (Leiden being the German city where Musschenbroek conducted his research work) consisting in the first historical assembly of a dielectric capacitor (Figure 6).

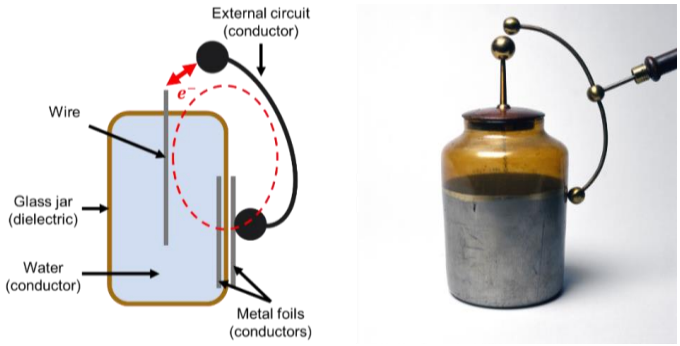

Figure 6 - Leiden Jar and its working principle (image in the right from ref. (8))

2.1.2. Mechanism

Capacitors are one of the most trivial forms of electrical energy storage, with a very simple working principle. During the charging process an electric potential is applied by an external power source, creating the electrical field through the dielectric which consequently has its molecules polarized. Once the electric potential is removed, the charge is fully stored in the conductors. The capacitor remains charged until the circuit is connected again, resulting in its discharge. The dielectric is strictly necessary for the capacitor to maintain its load since any current flow between the electrodes will ultimately lead to its full discharge. In the figure presented below (Figure 7) a schematic of the three stages of charge of a dielectric capacitor is represented with the logical orientation of the polarizable dielectric molecules.

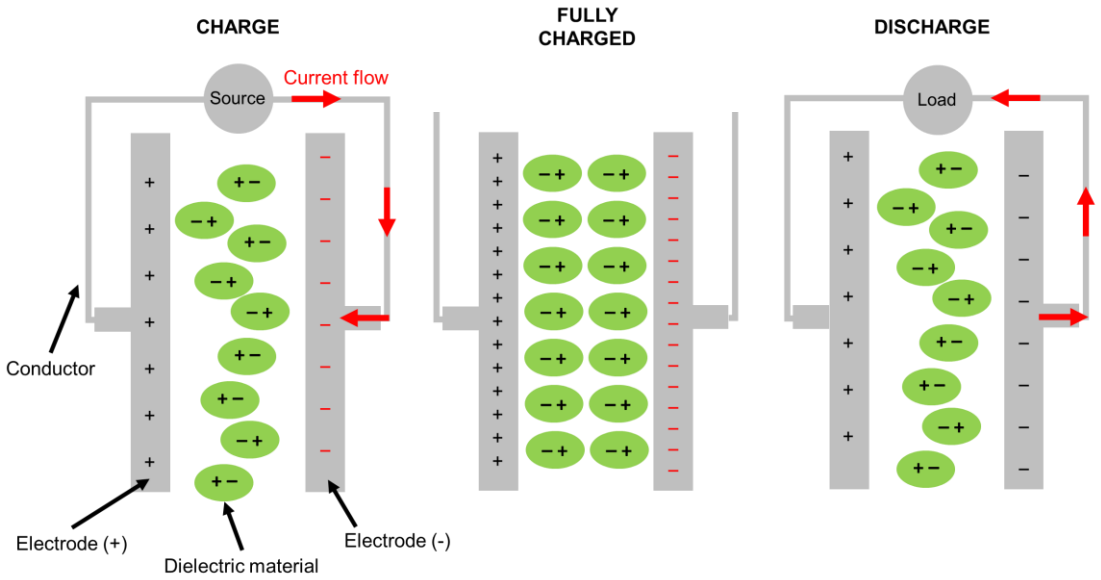

Figure 7 - Representation of the charge/discharge processes of a dielectric capacitor

The energy yield of a capacitor is fairly limited by being a predominantly physical process, as no chemical reactions occur. Notwithstanding, where the electrostatic charge storage lacks in energy density gains in power capacity. These devices are able to charge and discharge at very high rates (a few milliseconds) sustaining power densities around 1 to 10 kW/kg, incredibly higher than conventional batteries. The total stored electric charge of a capacitor can be calculated using equation [1] that proportionally relates the stored energy and the potential window of the system with the capacitance of the device. The capacitance is defined as the amount of charge the capacitor can store when facing a certain applied electrical potential. Numerically, capacitance is the amount of stored charge per 1 V.

$$\Delta Q = C.\Delta\psi \qquad [1]$$

ΔQ is the stored charge (coulombs, C), C is the capacitance (farad, F) and $\Delta\psi$ is the potential window (volt, V). Thus, capacitance is used as a performance indicator when comparing different capacitors: higher the capacitance, higher the device's ability to store more energy electrostatically. The capacitance

of the dielectric material is what ultimately defines the energy efficiency of the system and can be defined by the properties present in equation [2].

$$C = \varepsilon_0 . \varepsilon_r . S / b \qquad [2]$$

ε_0 and ε_r are the electrical relative permittivity of vacuum and dielectric material, respectively. S is the surface area of the electrode metal plates and b the thickness of the dielectric material. These properties are schematically represented in Figure 8.

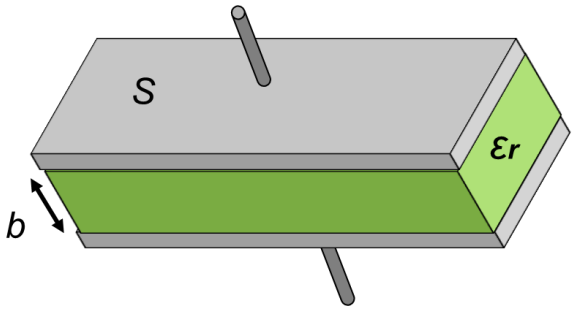

Figure 8 - Representation of a dielectric capacitor and parameters of equation [2]

2.1.3. Dielectric permittivity

According to equation [2], a good dielectric capacitor has a dielectric media with high permittivity, a good response to the polarization effect, a very thin thickness, and a big surface area. In the following figure several known dielectric materials are listed along with their relative permittivity (Figure 9).

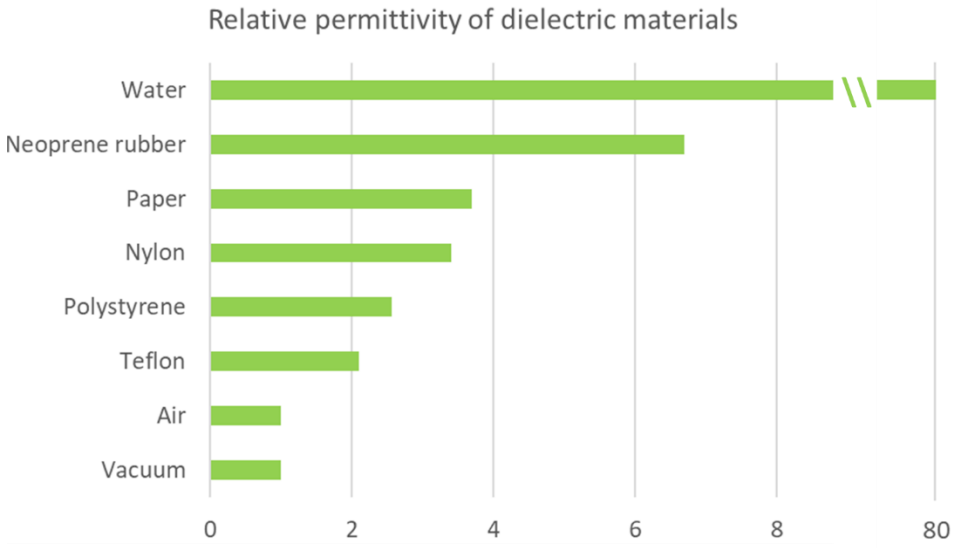

Figure 9 - Relative permittivity of known dielectric materials

2.1.4. Characterization

The pure electrostatic behaviour of a dielectric capacitor can be observed with cyclic voltammetry (CV), which is a potentiometry method that forces the device through at least two potential sweeps (forward and backward sweep) while measuring the intensity of the current. The shape of cyclic voltammograms (the respective curves obtained by CV) can indicate several details regarding the studied energy storage systems, more specifically, the type of mechanisms based on which the energy is stored by the devices. Dielectric capacitors are commonly recognized by their simplistic rectangular shaped curves (Figure 10), indicating the full capacitive property of the device and complete absence of chemical-derived processes.

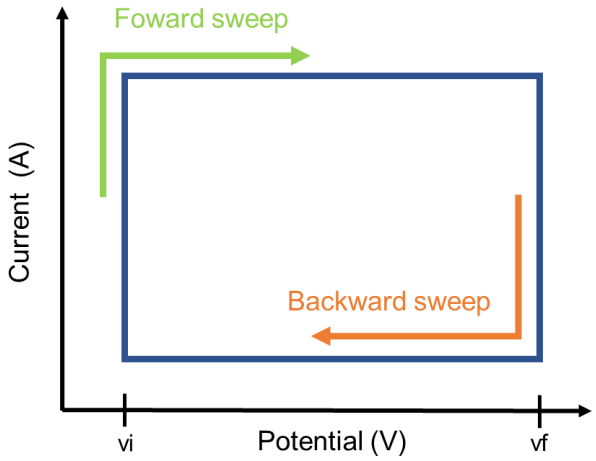

Figure 10 - Typical CV curve of a dielectric capacitor (vi is the initial potential, vf final potential)

In electrochemical studies of capacitors, the voltammograms usually differ from the pure rectangular shaped curves due to the presence of other phenomena that occur in the interface of the electrode's surface and the media's bulk, often linked with different types of parasitic chemical reactions and diffusion mechanisms that rule the electrochemical systems. Nonetheless, as far as dielectric capacitors are concerned, the peak current value is achieved almost instantly as soon as the potential window starts to be swept, and drops in the same fashion when the sweep is inverted, thus indicating the almost instant charge and discharge rate of dielectric capacitors.

2.1.5. Applications

A common assembly of dielectric capacitors is usually the cylindrical geometry (Figure 11) where electrodes and dielectric materials are very thin, pressed against each other and rolled over a centre axis, forming the cylindrical format. This geometry and method of assembling a capacitor not only allows a very compact structure, and inexpensive shelling, but also a very high interface area, which, according

to equation [2], contributes to the higher capacitance of the device. This cylindrical layout is only one of several creative ways (Figure 12) to optimize the surface area and compactness of the capacitor.

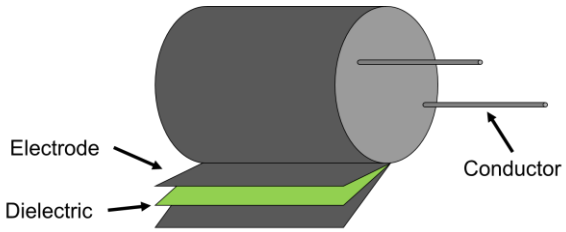

Figure 11 - Common cylindrical architecture of a dielectric capacitor

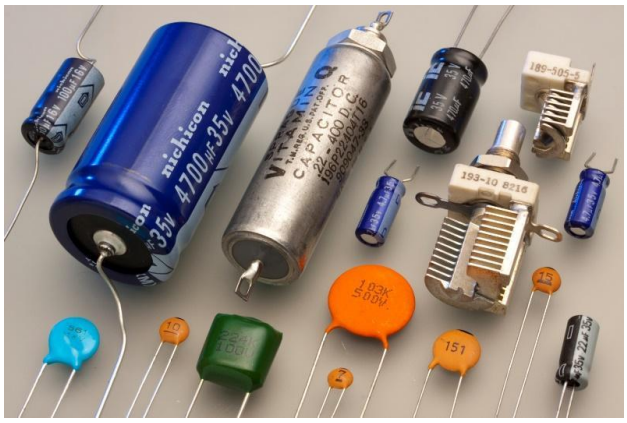

Figure 12 - Different assemblies of conventional capacitors (9)

Even though capacitors considerably lack energy density, they can be used to store energy in electronic devices when batteries are being changed, keeping the device powered until the full-fledged energy source is re-established by the battery. They can also be used to rectify current fluctuations in systems where the possible release of electric sparks may happen, acting as absorbers and bypass pathways that preserve the life of electronic devices. The distance between electrode plates, or the presence of the dielectric material itself, changes the capacitance of the device, meaning capacitors can also be useful sensors and control-specific systems by simply manipulating those variables. An interesting case-study is the application of dielectric capacitors in airplanes, where they are used as weight or pressure sensors (Figure 13) with the variation of the distance between their electrodes, or, as fuel indicators (Figure 14) by using the fuel as a dielectric material.

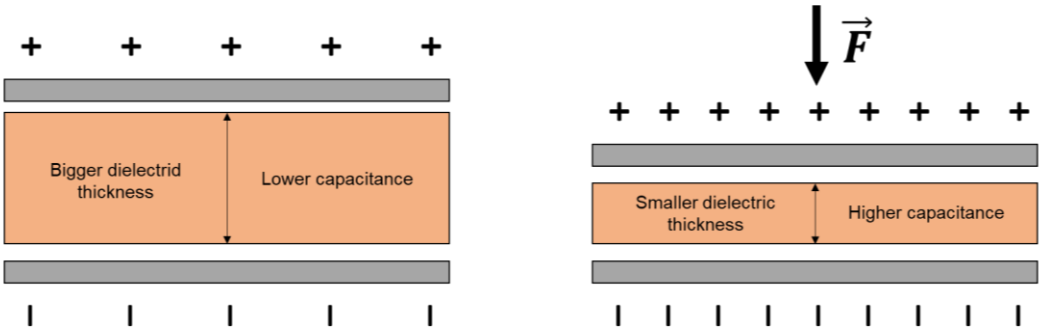

Figure 13 - Dielectric capacitors as weight/pressure sensors

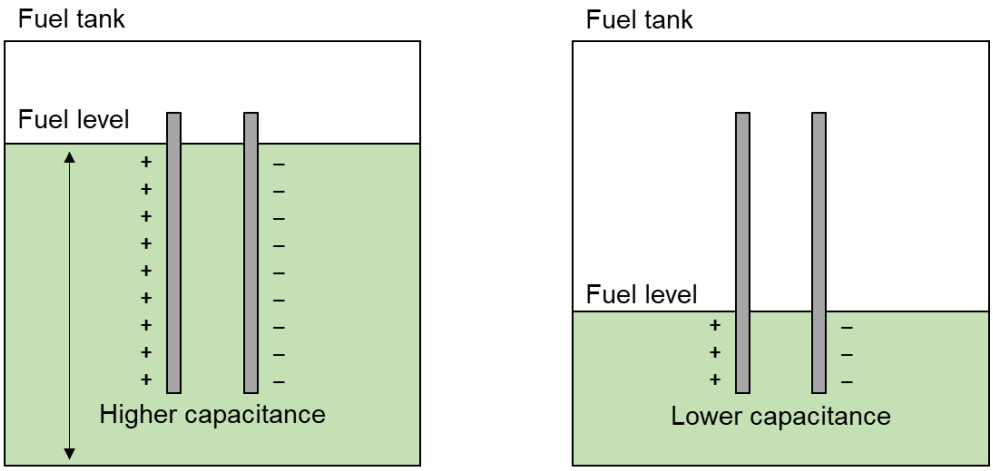

Figure 14 - Dielectric capacitors as fuel-meters

2.2. Electrolytic capacitors

2.2.1. Overview

Electrolytic capacitors store electrostatic charge just like dielectric capacitors. The fundamental working principle of these devices is that a metal electrode can be anodized with the objective of creating thin films of metal oxide at its surface, isolating the electrode. This process is an effective passivation of the metallic material which can be obtained by submitting the electrode to a very specific potential that allows the formation of oxygen in the anode and hydrogen in the cathode, thus, enabling the synthesis of a metal oxide adjacent to the electrode surface. The name of this capacitor results from the great similarity of the device's layout to one of an electrolytic cell, where an electrolyte is pressed in the middle of two polarized electrodes. In Figure 15 is presented a scheme that displays the general structure of a positively charged anodized electrode.

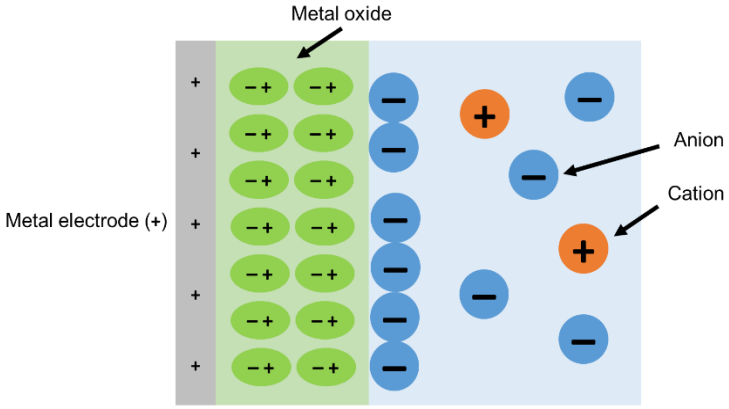

Figure 15 - Electrolytic capacitor (anodization)

While conventional capacitors attempts to assemble devices with thin dielectric thickness while maintaining high surface area (as well as other optimization parameters like permittivity), electrolytic capacitors hold this concept to higher stakes as the anodization of the metal into metal oxide consists in very thin coatings of dielectric material, considerably improving the overall capacitance. The study and research around electrolytic capacitors attempt to investigate new metals and better operating conditions to improve the process of metal passivation. Once the anodization is complete, and thus the thin metal-oxide dielectric coating is formed, the charge mechanism of the electrolytic capacitor is very much the same as of the dielectric counterpart.

2.2.2. Anodization process

The anodization process begins by submitting the target electrode to a very specific voltage which favours oxidation reactions at the positive electrode (anode oxidation - anodization) and reduction in the

negative electrode, thereby defined as cathode. Reaction (I) is the formation of hydrogen in the cathode, which occurs due to the negative charge build-up at the respective electrode.

$$2H^+ + 2e^- \rightarrow H_2 \qquad (I)$$

Simultaneously, the metal of the positive electrode is oxidized by the present hydroxide ions in solution, creating the anodized metal (II).

$$M + nH_2O \rightarrow MO_n + n2H^+ + n2e^- \qquad (II)$$

Where M is the exposed metal material of the electrode and n the stoichiometric number of water molecules necessary for the anodization to proceed. Reaction (II) is the overall sum of three reactions that occur in the anode. A prime example of an anodization process is the formation of anodic aluminium oxides (AAO) whose formation reactions are represented by reactions (III) and (IV) summed up by the overall reaction (V), which is analogous to (II).

$$Al \rightarrow Al^{3+} + 3e^- \qquad (III)$$

$$2Al^{3+} + 3OH^- \rightarrow Al_2O_3 + 3H^+ \qquad (IV)$$

$$2Al + 3H_2O \rightarrow Al_2O_3 + 6H^+ + 6e^- \qquad (V)$$

The anodization process is often referred to as *passivation* due to the non-reactive properties of the resulting oxides. What ultimately sets passivation different from a corrosion process (also enabled by metal oxidation) are the potential and alkalinity conditions upon which the oxidation occurs. These conditions can be studied by a Pourbaix diagram (Figure 16) which represents the regions and boundaries at which different forms of a metal oxide exist in a certain metal-solution pair system.

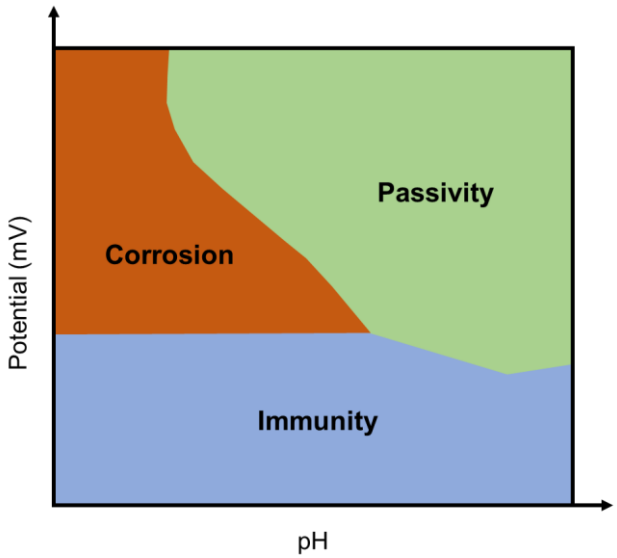

Figure 16 - Schematic format of the Pourbaix diagram of a metal-solution system

The passivation of a metal is a well-known technique with several different applications. Among the most studied materials is aluminium [10-12], magnesium [13-15], niobium [16-18], and titanium [19-21]. The applications and focus of these investigations range from metal coating for biomedical applications, corrosion protection, synthesis of porous films, metal self-colouring, and, evidently, energy storage.

2.3. Electrochemical double-layer capacitors

2.3.1. Overview

Named after the double-layer effect first described by Helmholtz, electrochemical double-layer capacitors (EDLCs) are a type of supercapacitors that store energy electrostatically through the reversible adsorption of electrolyte ions at the electrode's surface. EDLCs differ from conventional capacitors due to the local polarization of the electrolyte's ions and the consequent formation of the double-layer planes [22]. The double-layer is a complex molecular phenomenon that several different models have attempted to describe by understanding the behaviour of the electrolyte's components and their realistic interactions with the electrode's surface. The development of these models is a continuation of the conclusions of the first theories concerning the double-layer, attempting to answer the present flaws and deviations from reality the best way possible by formulating new assumptions and considerations regarding the properties of the electrolyte's components.

2.3.2. Helmholtz model

The separation of charges was first discovered by Hermann von Helmholtz who observed the creation of a layered interface between electrodes' surface and electrolyte bulk phase. Helmholtz developed the understanding that ions of the opposite charge simply neutralize the counter charge at a distance d which is the distance from the ion's centre to the surface of the electrode of opposite polarity to the ions. The layer defined by d is classically named as the *Helmholtz layer* which separates solid phase (electrode) from the electrolyte's bulk. Figure 17 schematically represents the Helmholtz model.

The separation of charges that results from the ion neutralization represents a local case of dielectric capacitance as charge is stored electrostatically within the Helmholtz layer. This created a potential gradient between the electrode's surface and the ions, ψ_0 being the electrode's potential and ψ the potential across the Helmholtz layer. Therefore, equation [2] can be applied to quantify the layer's capacitance. This compact counter-ion model is considered to be rigid as it does not accurately describe the reality of the double-layer, disregarding the effects of other components in the diffuse layer and the existence of adsorption processes at the surface of the charged conductor. It is also important to refer that the ions are in a solvent-rich phase that should be pertinently considered in order to optimize the double-layer model as the presence of solvent molecules should increasingly affect the thickness of the Helmholtz layer d, and, consequently, the layer's capacitance. The Helmholtz model is thereby a

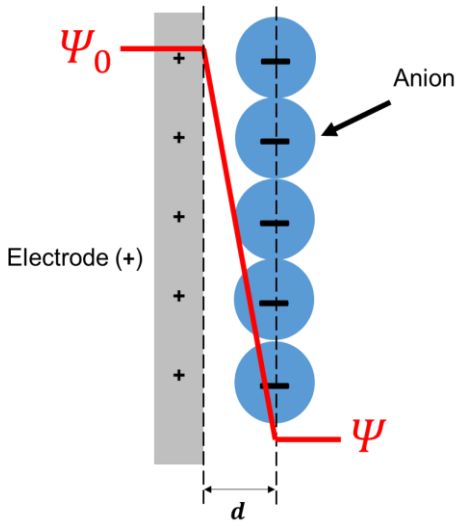

Figure 17 - Helmholtz model

highly simplistic theory that was set as a primary approach towards the complex phenomena that is the double-layer. The following theories that try to explain the EDL will consider other essential parameters and system properties that overall improve the layer's theoretical approximation with nature's behaviour.

2.3.3. Gouy-Chapman model

Gouy and Chapman state that the potential between the electrode's surface and the ion's counter-charge is not entirely accurate with the dielectric capacitor model, admitted by Helmholtz, but rather in line with the diffusion of the solvated ions that diffuse towards the electrode surface. While the model admits that the electrode charge is neutralized with ions of the opposite charge, it also suggests that the counterions, present within the diffuse layer (name hereby given to the double-layer), diffuse through the electrolyte according to their kinetic energy, setting the double-layer thickness through an assumed Boltzmann distribution [3].

$$p = e^{E/(kT)} \qquad [3]$$

p is the probability of a state of energy E at temperature T occurring and k is Boltzmann constant. Figure 18 represents the diffuse layer suggested by Gouy-Chapman model, explicitly stating that the potential varies exponentially like the Boltzmann distribution mathematically defines.

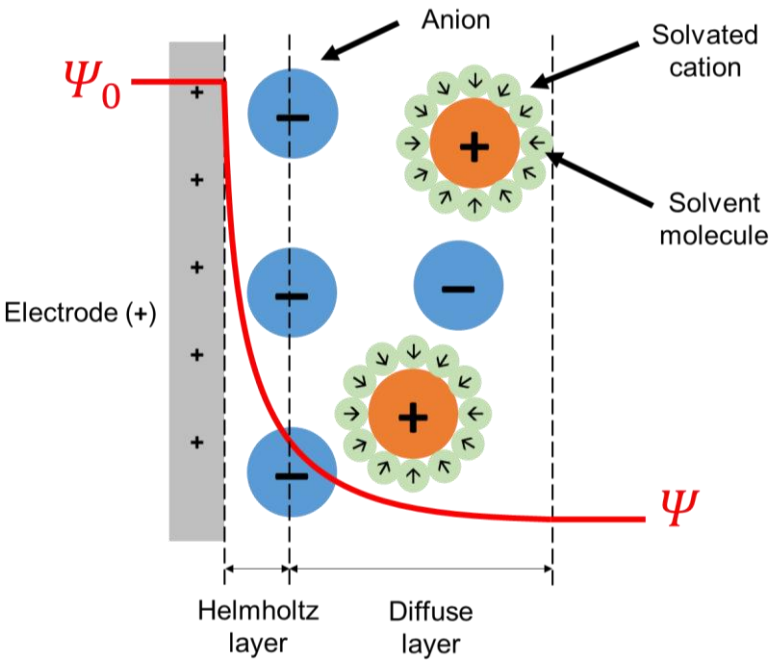

Figure 18 - Gouy-Chapman model

According to the Helmholtz model, the only pertinent layer is defined by the approximated distance from the ion's centre to the charged conductor's surface. However, Gouy-Chapman model states that

the diffuse layer can be mathematically calculated by integrating the expression that results [23] from the combination of Boltzmann distribution, adapted in the form of equation [4], with Poisson's equation of electric surface potential [5].

$$n_i(x) = n_0 e^{E/(kT)} \quad [4]$$

$$\varepsilon_r \varepsilon_0 \frac{d^2\psi(x)}{dx^2} = -\rho_i(x) \quad [5]$$

$n_i(x)$ is the molar concentration of component i at x distance from the electrode surface, n_0 is the molar bulk concentration and ε_r is the relative permittivity of the electrolyte. The energy (E) can explicitly highlight the valency and potential of its state with:

$$E = -z_i e \psi(x) \quad [6]$$

where z_i is the ion's valency and e is the charge of a proton. In equation [5], $\rho_i(x)$ is the charge density at distance x and can be defined with the following expression:[8]

$$\rho_i(x) = \sum_i n_i(x) z_i e \quad [7]$$

Equation [8] can be obtained by combining equations [4], [5] and [7], finally creating evidence of a relationship between the thickness of the diffuse layer, the valency, and the concentration.

$$\varepsilon_r \varepsilon_0 \frac{d^2\psi(x)}{dx^2} = -\sum_i n_i(x) z_i e \quad [8]$$

According to equation [8], the distance (thickness) from the diffuse layer to the electrode surface increases with the valency and concentration of the ions in the electrolyte. In fact, according to literature [24] this model deviates from reality when applied to cases with highly charged double layers where the thickness of the layers is greater than the thickness calculated from integrating equation [8], revealing a fundamental limitation in the Gouy-Chapman model.

2.3.4. Gouy-Chapman-Stern model

Another limitation in the Gouy-Chapman model is that it does not consider the size of the ions as a resisting factor in their approach towards the surface of the electrode. It approximates every component as point charges [24] only limited by their kinetic energy during diffusion. Stern's modification of this model states that the Helmholtz notion of a primary layer is incomplete, and that Gouy-Chapman diffuse layer does not apply as close to the surface as it claims. This model thereby assumes the existence of specific adsorption of ions between the immediate counterions in the charged electrode, explaining that between the counterions and the diffuse layer rests two planes defined by the opposite charged ions. Taking the example of a positively charged electrode, this model theorizes that the negative ions that neutralize its charge (specific adsorption) define the inner Helmholtz plane (IHP) while the non-specifically adsorbed solvated ions define the outer Helmholtz plane (OHP). The distance from the electrode surface to the OHP is thereby named as the *Stern layer* and sets a much more realistic dielectric-like behaviour before

the diffuse layer of Gouy-Chapman model is established. Gouy-Chapman-Stern model (Figure 19) answers the limitation of the unreliability of the previous theory regarding highly charged double layers as it further pushes the boundary of the diffuse layer away from the surface of the electrode. Gouy-Chapman-Stern model combines the two previously presented models into one. Note that the distance from the electrode surface to the IHP is the Helmholtz layer.

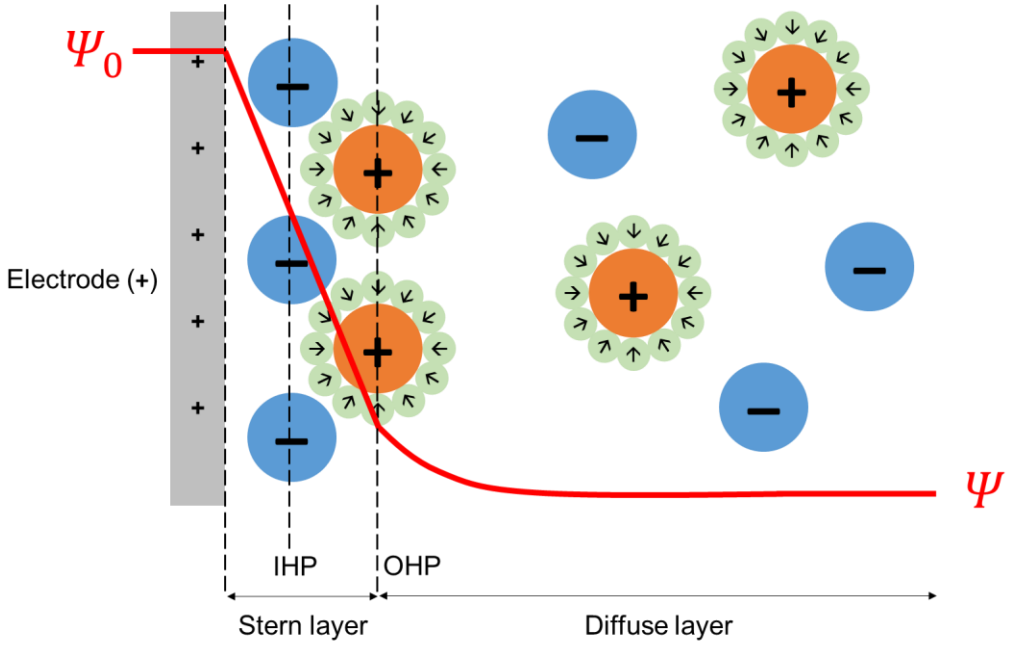

Figure 19 - Gouy-Chapman-Stern model

2.3.5. Modern adaptations of classical theories

These classical theories of EDL are based in qualitative premises, lacking the quantitative understanding of the double layer effect. Nevertheless, these models have established the necessary foundations that allowed the development of new modern theories which attempt to answer the inaccuracies of the classical models. Huang et al. [25] made a thorough review of the classical and modern models alike, exposing the important factors considered by some and neglected by others. Among the considerable deviations, one of vital factors noted by literature, that remain unspecified by classical models, is the porosity effect in the electrode's surface. Porosity considerably alters the relationship between capacitance and surface area in a non-linear manner, unlike Helmholtz ideals assumed by equation [2]. These 3D structures will be further explored in the following section about pseudocapacitors, yet, it is important to expose the consequences of surface curvature and electrode porosity in the behaviour of EDL in electrochemical capacitors.

In a given active material, specific surface area (SSA) increases with the degree of porosity. Equation [2] states that the capacitance varies linearly with the area, which is inaccurate with nature. Dimensions like pore volume and depth must be included in EDL capacitance models for porous

electrodes. Considering the case of cylindrical pores, Huang et al. further exposes modifications with equation [9].

$$C = \frac{2\pi\varepsilon_r\varepsilon_0 L}{ln\,(B/A)} \qquad [9]$$

This equation includes parameters A and B which are geometrical length variables of the cylindrical volume of Figure 20, while L is the depth of the pore which cannot be visible in the figure due to the absence of the depth dimension in the 2D representation.

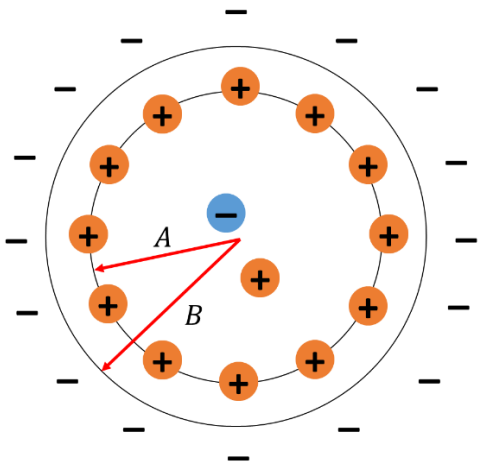

Figure 20 - Cylindrical EDLC pore geometry. A the inner radius and B the outer radius [25]

The above figure represents a negatively charged carbon-based electrode mesopore holding solvated positive counterions by the pore walls (orange), as Helmholtz model suggests. Huang et al. further demonstrated the pore size effect in carbon-based EDLCs capacitance by normalizing equation [9] into the form of equation [10] in order to experimentally fit the porous model.

$$\frac{C}{S} = \frac{\varepsilon_r\varepsilon_0}{B\;ln\,(B/(B-d))} \qquad [10]$$

d is the distance of the counterions from the electrode surface (length of IHP). In the same paper, equation [10] was adapted to the nanopore scale in the form of equation [11], where A_0 is the radius of the ion, thus assuming that the distance of the ion's centre to the electrode's surface is its own radius.

$$\frac{C}{S} = \frac{\varepsilon_r\varepsilon_0}{B\;ln\,(B/A_0)} \qquad [11]$$

By data fitting equations [10] and [11], Huang et al. demonstrated that these equations fit experimental values with remarkable accuracy thus concluding the crucial relationship between pore volume and EDLC capacitance. Several other capacitor properties are expected to affect EDLCs behaviour, porosity being a fundamental one. However, quantitatively depicting the double layer effect remains a challenge [25].

2.3.6. Electrode carbon-based materials

Carbon-based materials are the prime materials used to assemble EDLC electrodes. They are inexpensive products with very high specific surface areas (from 1000 to 3000 m^2/g) resulting in highly capacitive electrochemical responses. As carbon is a highly versatile material, and easy to manipulate, several different nanostructures can be synthesized with this element as well as further treatments and activation methods can transform carbon structures into more electrochemically enabling materials like activated carbon (AC), carbide derived carbons (CDC), carbon nanotubes (CNT) and graphene [26]. These different forms of carbon will be described below.

Activated carbons (AC)

ACs are amorphous carbons of very high surface area. They are synthesized through physical and/or chemical methods that convert natural precursors into elementary carbon powders with interesting properties that are considerably appealing for electrochemical and catalytic engineering applications. The production of ACs is referred to as an accessible and simple synthesis procedure of rewarding outcome which is self-evident in the fact that activated carbons are the most used choice in EDLC electrodes despite the existence of better performing carbon-based materials. The synthesis of ACs usually comprises a carbonization step (physical activation) followed by an oxidizing treatment (chemical activation). The physical process of carbonization consists in the combustion of a carbon-rich precursor at high temperatures (600 – 900 ºC) under an inert atmosphere (e.g. under N_2). The product of carbonization, and its quality, are influenced by the operating conditions of the process like temperature and carbonization time. Afterwards, chemical activation can be conducted to optimize the pore size distribution of the AC by extending the porous volume and surface area of the nanostructure. This is accomplished through redox reactions between the carbonized material and oxidizing agents such as bases and acids (e.g. KOH, H_2SO_4, alkalis, and carbonates) [27]. Temperature, treatment time, and oxidant concentration are some of the most studied operating conditions used to optimize the pore sizes and to adjust the density of more uniform micro/mesopore-sized frameworks that result in different electrochemical properties which are consequently dependent of the associated electrolytes and current/potential settings imposed in the AC electrode. The effect that physical and chemical activation processes have in the end-product's properties are well known for decades [28] as chemical activation allows for a more effective and desirable pore size distribution than purely physical activation. However, even though chemical activation manages to create a high surface area within a porous framework, the pore size distribution is mostly broad and rarely able to be further optimized. This lack of consecutive optimization opportunities is a known drawback of AC synthesis. The AC precursors can be obtained from a wide range of natural materials. Recently, the focus on precursors based on biomass raw materials such as grapefruit, rice husk, straw, aloe vera, fruit skins, eucalyptus-bark, soya, among others [29] have attracted large interest. To produce activated carbon, the raw biomass material must be

subject to the activation processes. A general overview of AC production processes can be seen in Figure 21.

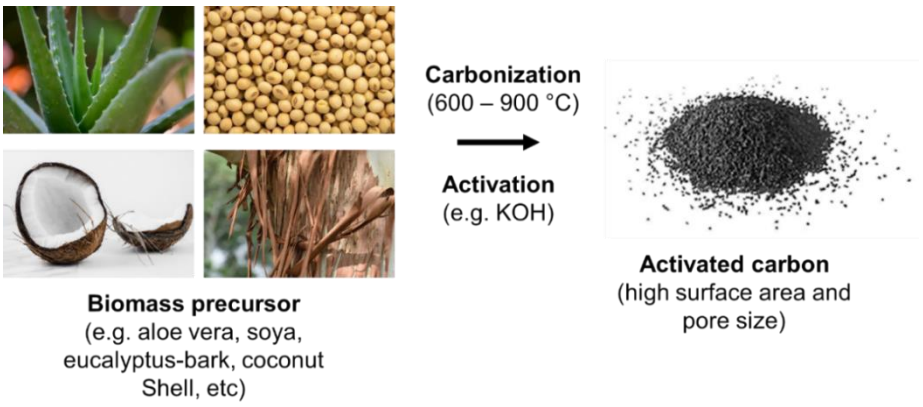

Figure 21 - Synthesis of activated carbon

Carbide derived carbons (CDC)

As the name reveals, these carbons are obtained from carbide precursors (materials composed of carbon and a metal). CDCs are created by removing metals from a carbide's lattice (Figure 22) through thermal and chemical extractions. The most used carbide precursors are usually composed of tungsten, zirconium, silicon, and titanium. When combined with carbon, these metals (and semi-metals) form interesting lattice conformations which allow different porous structures to be created from carbides [30].

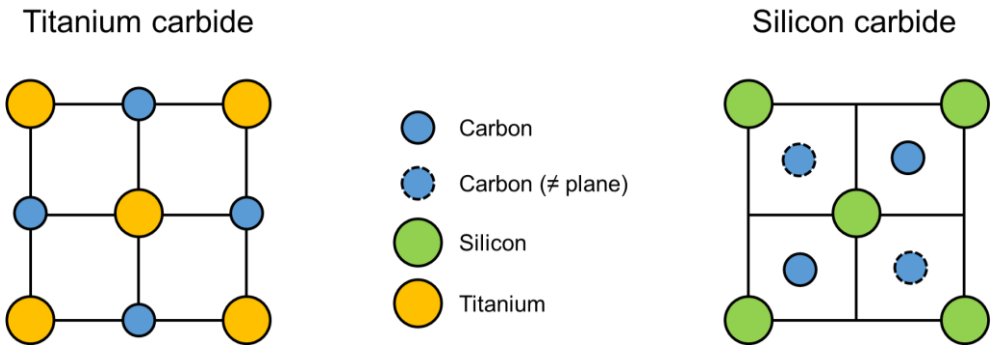

Figure 22 - 2D structure of Ti and Si carbide lattices

The metal extraction can vary in depth as the transformation process is able to define the intended percentage of removed metal from the carbon framework. This allows an accurate tune of functional groups at the structure's surface for improved electrochemical behaviour [31]. Usually, the processes that convert carbides into carbons consist of chemical treatments with halogens (e.g. chlorination) and physical treatments under vacuum (e.g. vacuum decomposition). These are often executed under very

high temperatures (300 – 1200 ºC) which weakens the bonds between the metal and the carbon in the bulk of the carbide. Halogen treatment is usually performed via chlorination due to the high reactivity of chlorine with metals. The process consists in the dissociation of the metal from the carbon framework by reacting with chlorine and consecutively extracting the metal in its chlorinated form. This reaction transforms the carbide into a metal free lattice of whichever degree of extraction intended which can be appropriately manipulated due to the linear kinetic behaviour of the chlorination step [31]. Reaction (VI) summarizes the halogenic treatment.

$$MC_{(s)} + nCl_{2(g)} \rightarrow M(Cl_2)_{n(g)} + C_{(s)} \quad \text{(VI)}$$

M is the metal present in the original carbide, MC. The metal is evaporated during this process in its chlorinated form of $M(Cl_2)_n$ while the lattice remains carbonic, $C_{(s)}$ (the CDC). It is long known that the formation of CDCs is linearly dependant of the kinetics of reaction (VI) with conclusions obtained in 1960 by Kirillova et al. in whose work was observed the thickness of produced CDC varying linearly with time, allowing the previously mentioned tuning of appealing accuracy [32]. Despite the chlorine treatment deeply affecting the conformation of the carbide lattice during the metal extraction, literature has often observed that CDCs maintain the shape of their original carbide lattices [33]. This shape stability is still not entirely understood. Regardless, this shape stability has created an incredible opportunity in the production of carbon-based electrodes for energy storage due to the possibility of fine-tuning the porosity by simple adjustments of kinetic and thermal nature, resulting in carbons with surface areas among the highest in the field (up to 3000 m^2/g).

Vacuum decomposition is a method of metal extraction at high temperatures (above 1200 ºC) under vacuum. The working principle is based around the high fusion and boiling points of carbons when compared to the lower volatility of metals. In this process, simple melting and evaporation of the metal atoms is conducted, separating the metal from the carbon (VII).

$$MC_{(s)} \rightarrow M_{(g)} + C_{(s)} \quad \text{(VII)}$$

The use of high temperatures also boosts the conformational ordering of carbon nanostructures. Therefore, more complex and ordered pore conformations can be achieved from vacuum decomposition, such as CNTs and graphene. It is also to be noted that, unlike halogen treatment, this process does not involve the insertion of alien molecules in the carbide lattice, thus avoiding the presence of residual material within the final carbon structure, contributing to the purity and uniformity of the pore distribution in the final carbon material.

Carbon nanotubes (CNT)

Carbon nanotubes are another creative set of materials that illustrates how the transformation of simpler carbon-based precursors, like hydrocarbons, can result in complex and peculiar nanostructures. CNTs are hollowed carbon nanocylinders structured perpendicularly to a metal conductor, giving rise to a valuable accessible surface area with high conductivity. They are usually classified by the layer density of the nanotubes: single-wall CNTs (SWCNTs) and multi-wall CNTs (MWCNTs). Due to the preparation of CNTs being highly dependent on the growth control of carbon's crystalline order, the purity of the carbon directly influences the morphology of the synthesized nanotubes and consequently affects the specific capacitance of electrodes. The well-ordered structures allow the conjugation of CNTs with other materials (through coating or other functionalization processes as shown in Figure 23) that increase the energy density of the system. Such is the case of pseudocapacitive materials like composites of metal oxides and polymers [34]. Pseudocapacitance will be a subject extensively covered in the next section when overviewing the working principles of pseudocapacitors.

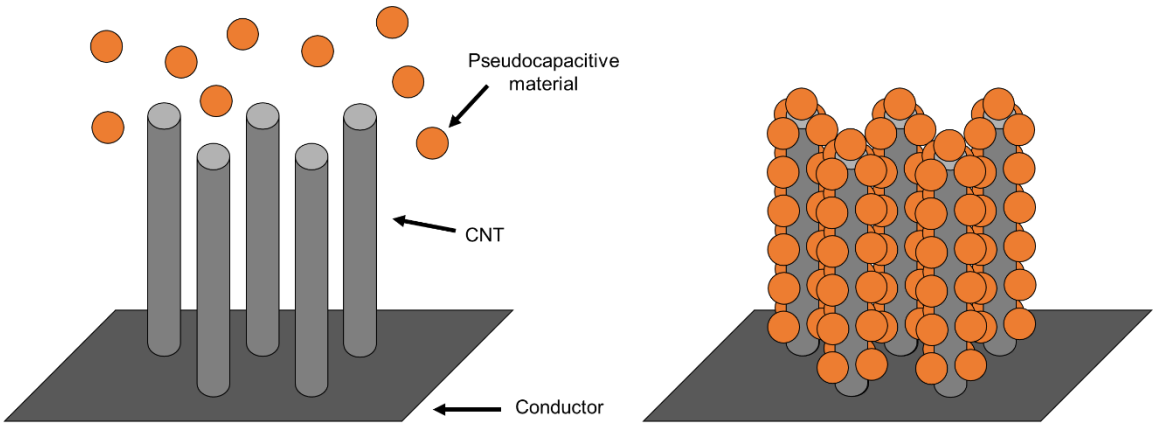

Figure 23 - Schematic of CNT coating (e.g. electrodeposition) with a pseudocapacitive material

The electrochemical behaviour of CNTs can be optimized by further chemical treatment with redox agents. Such strategy has been reported in MWCNTs which displayed higher specific areas when treated with nitric acid. CNT powders have also been observed with improved specific capacitances after being oxidized [35].

Graphene

Graphene is a pure carbon structure where each carbon bonds with three other carbon atoms, creating a hexagonal mesh monolayer (Figure 24). Graphene has the record of being both the thinnest and strongest material ever measured in materials science [36]. These two properties of graphene gave inherent value and research interest to this carbon-based material.

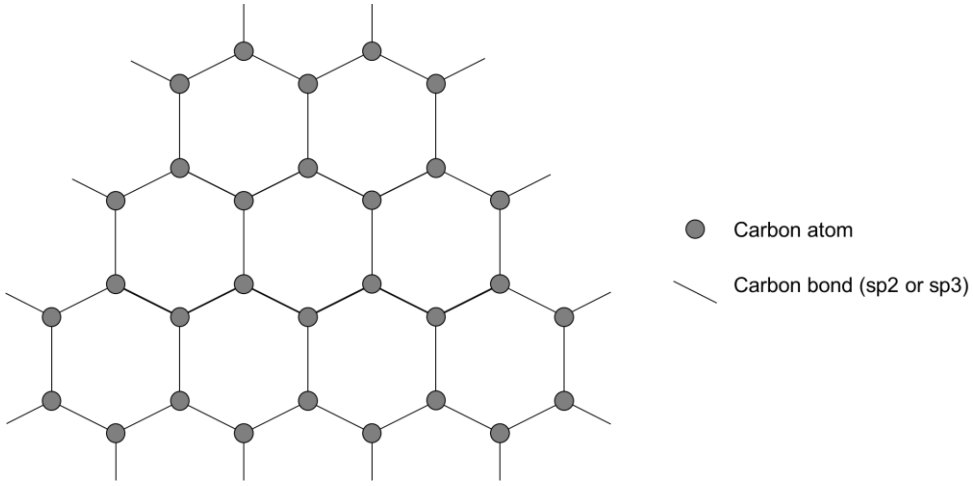

Figure 24 - Hexagonal mesh of graphene

Being a monolayer of atomic thickness (diameter of a carbon atom), graphene properties are very pertinent in electrochemistry. Moreover, its high thermal and electric conductivity, great high surface area (~2630 m^2/g, close to the usual ranges of activated carbon), and the ability for its 2D conformation favours to be manipulated into other carbon nanostructures. The preparation of graphene is a very delicate process. Any unwanted stacking of graphene sheets results in the irreversible formation of graphite: a bulk material composed of several bonded graphene layers that lacks the wanted and targeted properties of the isolated monolayer of graphene. Synthesis methods of graphene can be physical (mechanical exfoliation) or chemical (chemical vapor deposition, CDV) the latter one being significantly more used for graphene mass-production. Mechanical exfoliation consists in highly ordered graphite being peeled by a glue tape that is sensible enough to specifically peel a single carbon monolayer, thus extracting graphene. Thermal treatments are usually needed in order to purify the removed graphene from glue residues that may affect the properties of the monolayer [37]. This process for graphene extraction is represented in Figure 25.

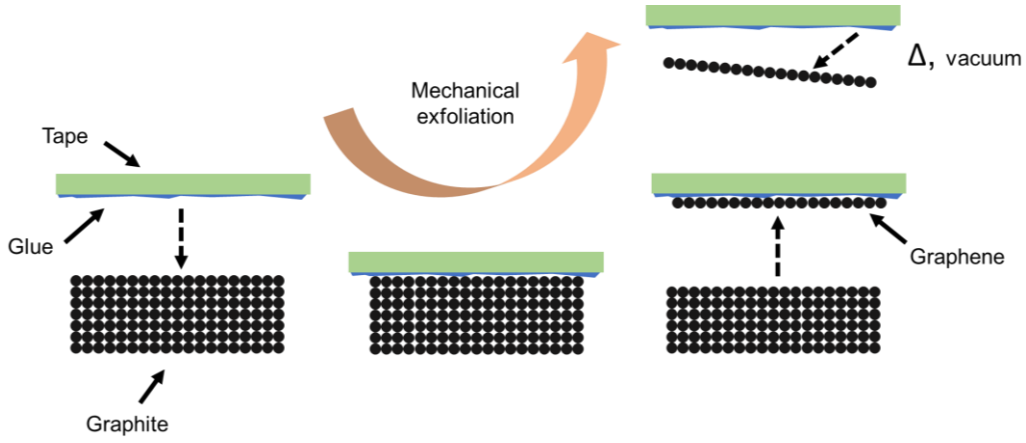

Figure 25 - Mechanical exfoliation of graphene

Chemical vapor deposition (CVD) is a chemical pathway of synthesising graphene. It comprises of decomposing a hydrocarbon gas in a pre-annealed (900 – 1000 ºC) transition-metal film, which is then cooled, enabling the diffusion of the dissolved carbon atoms through the film and into the surface where they bind and form graphene [38,39]. The process is schematically represented in Figure 26.

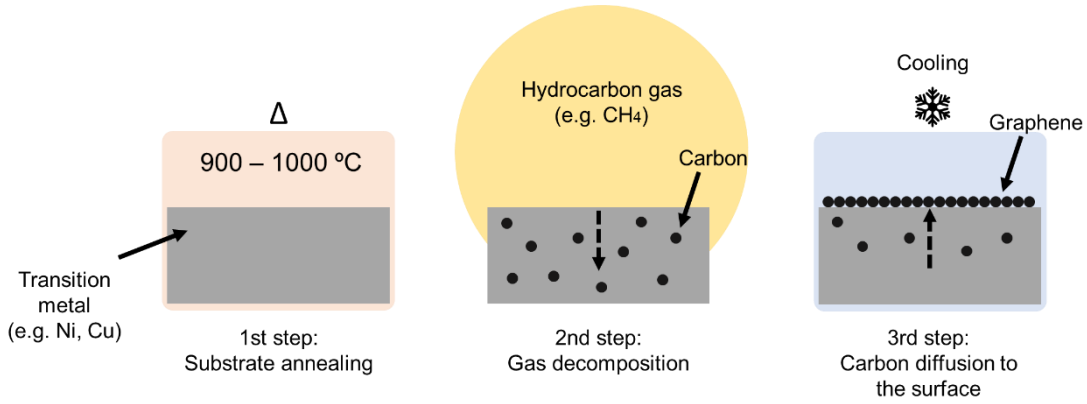

Figure 26 - CDV of graphene

Several studies in literature [40-42], are dedicated to reach record performing graphene electrodes by chemically treating graphene monolayers with reducing and oxidizing reactions. In a very recent study, Le Fevre et al. made an experimental comparison between different types of graphene electrodes like reduced graphene (rG), reduced graphene-oxide (rGO), graphene nanoribbons (GNR), among others [42]. The study reached the conclusion that reduced forms of graphene presented very high specific capacitances (~153 F/g for rG and ~119 F/g for rGO) when compared to the highest performing form of pure graphene (~44 F/g for anodic electrochemically exfoliated graphene – AEEC). The specific capacitance improvement of these graphene materials is believed to be result of the pseudocapacitive contribution of oxygen groups in the graphene framework, a contribution which will be further reviewed in this work's - pseudocapacitors section. Chemical optimizations such as these come with drawbacks related to the inherent insertion of new functional groups in the graphene monolayer. Degradation issues after galvanostatic tests and resistive losses are some of the reported disadvantages. Nevertheless, redox treatments of graphene can further be improved with other engineering pathways (like the addition of CNTs in the graphene structure).

Overall, it can be concluded that comparing carbon-based materials is not a straight-forward task. Each one of these electrodes differ in shape, synthesis pathways, and influencing factors in the electrochemical response of supercapacitors. But the true challenge of rating these materials lies in the ingenious, and, ultimately, almost infinite ways that carbon electrodes can be optimized by simple associations with other compounds, and sometimes, with other forms of carbon (e.g. graphene-CNT electrodes). Therefore, the present literature is overwhelmed with research studies that cover many specific types of carbons, which makes them too unique for a one-dimensional evaluation to state that one is better than the other. In their work, González et al. provided an extensive review of carbon-based electrodes and reported the most interesting values achieved by several studies [24]. Figure 27

represents the minimum and maximum values of important properties for three carbon-based materials when used for electrochemical energy storage applications.

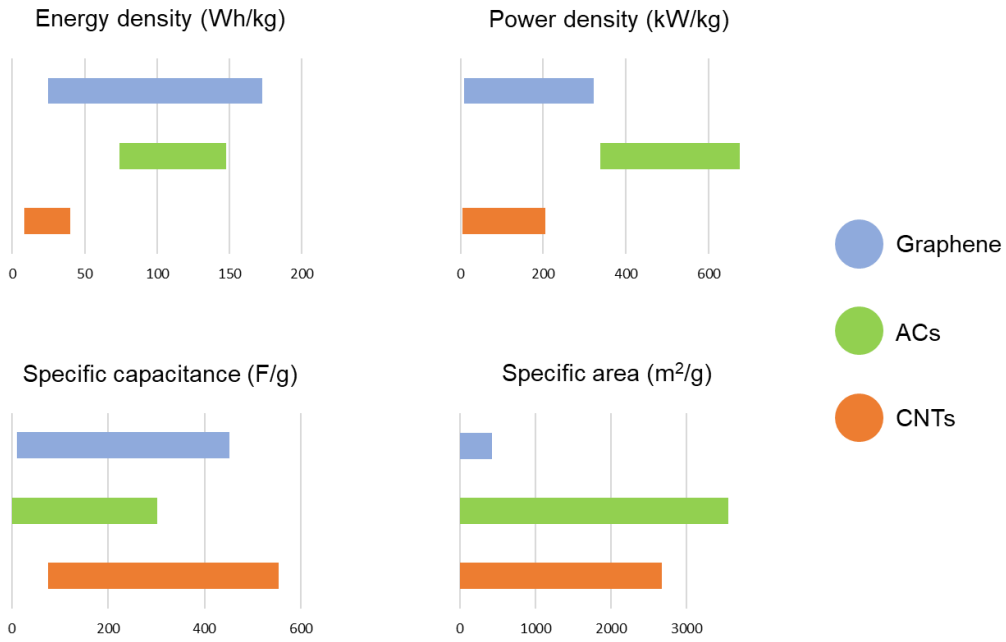

Figure 27 - Reported properties of graphene, ACs and CNTs based on (24)

It can be immediately observed that the performance ranges of carbon materials are wide enough to actually include the ranges of another materials (as it happens with the energy densities of graphene and ACs), hence exposing how subjective comparisons like these can be when several pathways of optimization are available for carbon electrodes. Note that these properties often suggest the challenges the synthesis of certain materials are subject to, such is the case of the low maximum of graphene's SSA which may be related to the difficulty of graphene's synthesis.

Nevertheless, promising carbon materials and, in particular, their composites with certain metal compounds, are widening the prospects for new generations of electrode materials: the hybrid electrode. This ultimately reaches the goal of supercapacitors research field of building a broad alternative that fills the gap between capacitors and batteries by increasing their applications and improving the knowledge of what defines the electrochemical behaviour.

2.4. Pseudocapacitors

2.4.1. Faradaic and non-faradaic processes

Unlike EDLCs, pseudocapacitors are faradaic electrochemical devices that store energy via highly reversible and fast redox-based reaction mechanisms that contribute to higher energy density without greatly compromising fast charge/discharge rates. In order to fully understand pseudocapacitors, and their distinctive features when compared to conventional EDLCs supercapacitors, it is important to make the convenient distinction between faradaic and non-faradaic processes. These two concepts derive from the validity of Faraday's laws of electrolysis in the interface between an electrode and an adjacent electrolyte phase, labelling the behaviour and movement of charge and chemical components involved in the energy storage process. Faraday's laws states that the composition of a material in the electrode-electrolyte interface is directly proportional to the amount of electricity passed. Equation [12] is the mathematical definition of this statement, where m is the mass of generated material in the electrode, Q is the total electric charge, M the molar mass of the material, F Faraday's constant and z the valency of the material.

$$m = \frac{QM}{Fz} \qquad [12]$$

Despite the simple mathematical definition, labelling a process as *faradaic* may not be as straightforward as expected. The dominant (and classical) criterion present in literature defines the faradaic process as the one that involves charge transfer processes, while a non-faradaic process occurs when the charge stays electrostatically stored at the electrode surface. However, according to some authors, the exact meaning of these definitions is not so simple regarding what the charge transfer phenomena actually consists of. When taken literally, the term *charge transfer* can represent very different systems. In their work, Biesheuvel and Dykstra gave pertinent examples of charge transfer phenomena occurring in both faradaic and non-faradaic systems while providing a very interesting critical discussion of these processes [43]. Whenever ions diffuse from an electrolyte phase, the external circuit compensates the ionic charge by moving electrons to the electrode phase, maintaining the interface neutrally charged, which occurs in redox reactions and adsorption processes alike. This notion of charge transfer starts off by assuming that any kind of local charge displacement consists of a charge transfer phenomenon. However, as seen in the bulk of electrochemical literature, charge transfer is mostly referred to situations where redox reactions occur, and electrons are respectively transferred. Still, considering the topic at hand, it is important to dwell on the exact meaning and defining traits of faradaic and non-faradaic processes if a comprehensive understanding of pseudocapacitive electrodes is to be conducted.

During charging and discharging sequences, electrons flow in and out of an external circuit to the electrode materials. Consequent to this electron transfer, charged species diffuse in and out of an electrolyte to the electronegative material. Once the polarized components (electrons and charged species) meet at the electrode-electrolyte interface, both faradaic and/or non-faradaic process may occur depending of the system's thermodynamic and kinetic properties. Biesheuvel and Dykstra

analysed the factors that differentiate faradaic from non-faradaic processes by considering the presence of the movement of charged species, and the location of the electrode-electrolyte interface. It is a long and profound discussion that goes beyond the objective aimed in this work. Therefore, it is hereby assumed that a faradaic process is one where any redox reaction occurs at the electrode-electrolyte interface. By opposition, a non-faradaic process is one that separation of charge (electrons in electrode side and cations in Helmholtz layer) in the electrode-electrolyte interface occurs as a result of the EDL phenomena (electrostatic storage). The comparison between both processes is schematically represented in Figure 28.

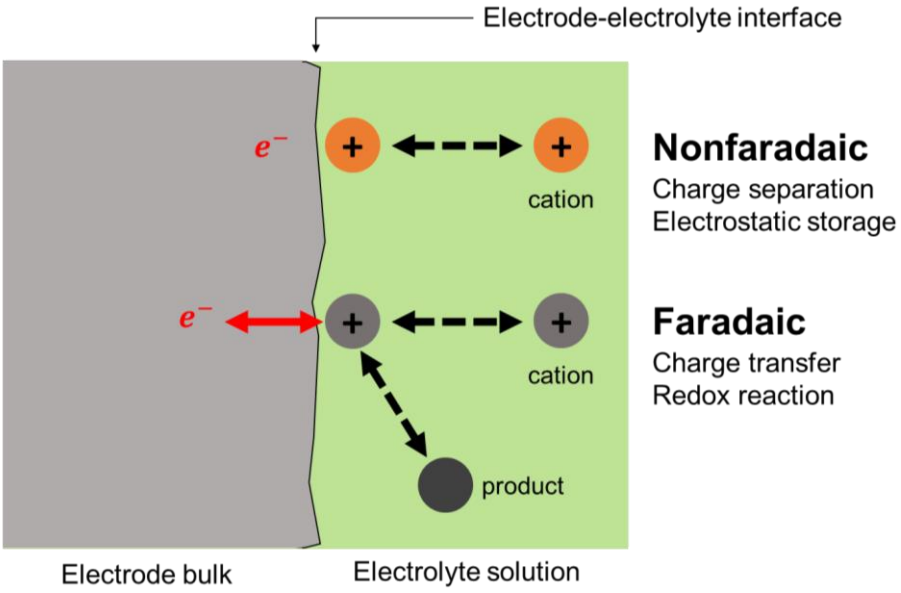

Figure 28 - Main difference between faradaic and non-faradaic processes

Situations and cases that involve highly segmented nanostructures (such as highly porous electrode materials) which make it difficult to outline the electrode-electrolyte interface and often involve solid-state diffusion (Figure 29) must be classified according to the processes that occur in the deepest interface accessible by the charged species.

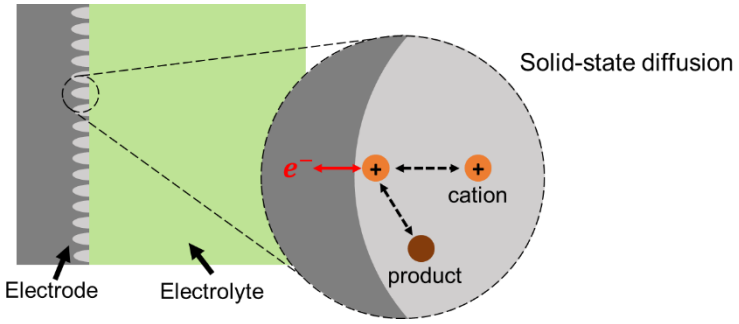

Figure 29 - Solid state diffusion in electrodes

This is also the case of intercalation processes where ions diffuse through a solid-state layered media and react in an interface between the electrode bulk and the electrode surface. During intercalation, the interface between the electrode and the electrolyte does not establish the conditions for a faradaic process to occur as a macroscopic analysis observes cations getting in and out of the electrode while the redox reaction occurs in its bulk.

2.4.2. Pseudocapacitance mechanisms

The battery-like features (i.e. charge transfer) of pseudocapacitors have origin in the fast-reversible redox reactions that take place in the surface or near-surface regions of the active material. Pseudocapacitance is the term that refers to the faradaic processes encompassed by this charge storage system. Depending on the properties of the electrode material, pseudocapacitance can be expressed as inherently intrinsic or extrinsic. Intrinsic pseudocapacitance is exhibited in a broad spectrum of morphologic conditions showcasing the same electrochemical pseudocapacitive behaviour regardless of the structure of the material. Extrinsic pseudocapacitance, contrary to the intrinsic one, manifests itself differently with the morphology of the active material as its behaviour is not the same in crystal conditions as it is in layered/porous structures. It is important to understand whether the pseudocapacitive behaviour of a material is intrinsic or extrinsic in order to efficiently optimize the electrochemical response to the intended goal values. There is no interest in trying to optimize the active material of an electrode through structural modifications (e.g. increasing porosity or tuning layers) if the pseudocapacitance mechanisms are purely intrinsic. There are three known mechanisms that create different pseudocapacitance behaviours: fast reversible redox reactions, intercalation processes, and underpotential deposition (Figure 30).

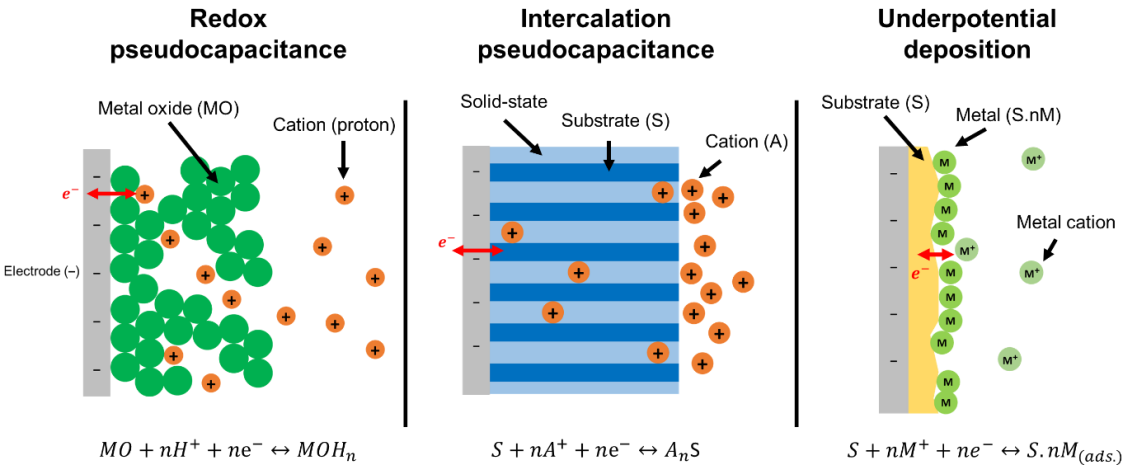

Figure 30 - Pseudocapacitive mechanisms

Each pseudocapacitive mechanism will be thoroughly explained in the upcoming sections, with special attention given to their energy storage capabilities, which are more relevant in redox and intercalation mechanisms.

Redox pseudocapacitance

What characterizes pseudocapacitors the most is their redox-like feature responsible for the high energy capacity at fast rechargeable rates. While batteries are full-fledged faradaic devices that store energy through redox bulk reactions involving the diffusion of ions through a solid-state electrode phase, thus allowing them to store great energy yields at the expense of the diffusion controlled low-power density, pseudocapacitors manage to hold redox reactions while maintaining an approximated rectangular-shaped CV, similar to their EDLC counterparts (Figure 31).

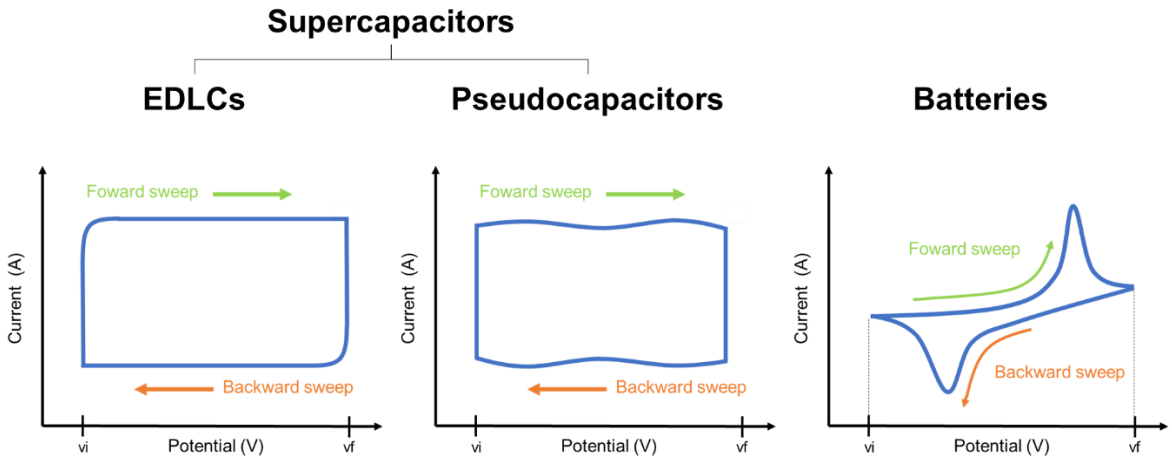

Figure 31 - Typical CV curve shapes of supercapacitors and batteries

The close proximity of EDLCs and pseudocapacitors CV curves suggests that the faradaic processes that occur in pseudocapacitors are not diffusion controlled (else the fast charge/discharge rates would not be as high) but rather based in surface or near-surface areas of the active material [44]. Therefore, the faradaic processes in pseudocapacitors consist of surface, or near-surface, fast reversible redox reactions. With these reactions occurring at the surface, the SSA is one of the most important factors liable to the optimization of the electrochemical response. This is where the creative combination of pseudocapacitive materials (e.g. metal oxides) with interesting 3D nanostructures takes place as seen before with CNTs in Figure 23.

The charge redox mechanism of pseudocapacitors is very similar to the one of batteries. During the charge process an external power supply injects electrons in the circuit forcing the current to flow from the positive to the negative electrode. The electronic density in the negative electrode attracts the cations from the electrolyte to be reduced in the electrode's active material. The most used and studied

pseudocapacitive materials are transition metal oxides (TMOs) which participate in the redox reactions by reacting with the electrolyte's protons (VIII) or eventually other ions.

$$\mathrm{MO} + \mathrm{nH^+} + \mathrm{ne^-} \leftrightarrow \mathrm{MOH_n} \qquad \text{(VIII)}$$

MO being the metal oxide and $\mathrm{MOH_n}$ its reduced form. During the discharge process, the inverse reaction occurs as the electrode surface is oxidized, releasing protons to the electrolyte while electrons are transferred to the external circuit. The process of opposite polarization can also occur, in which case, the pseudocapacitive material acts as a positive electrode in a basic solution where anions (e.g. OH^-) will participate in the reaction (IX).

$$\mathrm{MOH_x} + \mathrm{nOH^-} \leftrightarrow \mathrm{MOH_{(x-n)}} + \mathrm{nH_2O} + \mathrm{ne^-} \qquad \text{(IX)}$$

Both pseudocapacitive redox mechanisms with TMOs are represented in Figure 32.

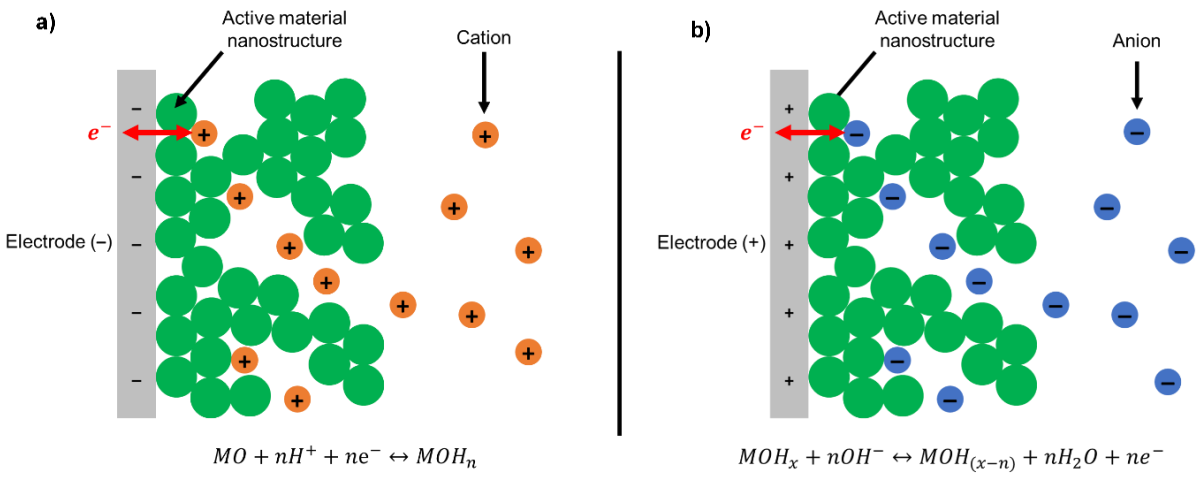

Figure 32 - Redox pseudocapacitance under acid (a) or alkaline (b) electrolyte

Intercalation pseudocapacitance

Intercalation pseudocapacitance is the insertion of ions (e.g. Li^+, Na^+, H^+) through layered nanostructures of an electrode. These ions react and provide an electron transfer across a solid-state interface within the active material. It is a case of a redox reaction occurring through a solid-state diffusion. During discharge, the opposite process occurs where the de-intercalation of the ions takes place after receiving the transferred electrons from the collector. This process requires a well-defined two-dimensional layered structure and large inter-layer spacing in order to enable the intercalation of ions within the active material [45]. Furthermore, intercalation pseudocapacitance allows the faradaic process to occur without phase changes in the crystalline structure which prolongs its cycling life at fast

charge/discharge rates, and, consequently, lowers its rates of degradation [46]. The generic reaction of this process, between a substrate and a cation, is represented by reaction (X).

$$S + nA^{+} + ne^{-} \rightarrow A_nS \qquad (X)$$

Where S represents a layered substrate, A^{+} the electrolyte cations and n the number of exchanged electrons during the reaction. Figure 33 shows a simple representation of the relationship between the ions and the active material.

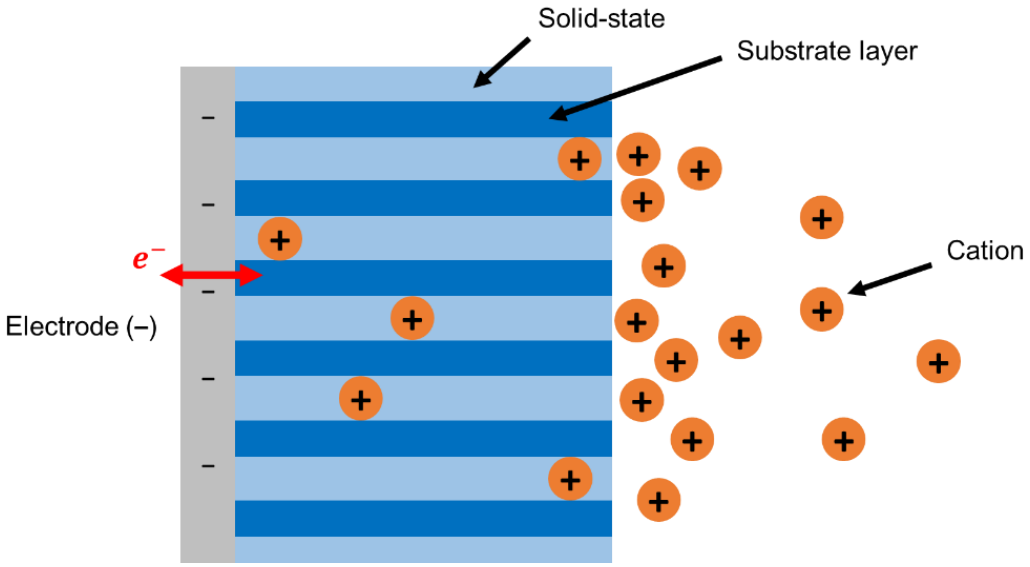

Figure 33 - Intercalation pseudocapacitance

Only certain transition metals are known to permit the preparation of the layered structures needed for pseudocapacitive intercalation to occur. The three most studied metals are molybdenum [47-49], vanadium [50-52], and tungsten [53-55], with some other studies covering titanium [56] and niobium [57]. The focus and interest in these transition metals comes from their high oxidation states which allows the formation of stable oxides that consequently result in weaker interactions of their oxygens with other adjacent transition metals. This weaker bonding promoted between the transition metal facilitates the formation of layers with convenient inter-spacing, creating openings that favour the intercalation of cations [58].

Underpotential deposition pseudocapacitance

As the name reveals, this pseudocapacitive mechanism relies on the deposition of a certain metal over another, under its own equilibrium potential. The metal onto which the deposition occurs, the substrate, serves as an inert support for interesting active materials. Reaction (XI) is a generalized form that represents the deposition (adsorption) of a metal cation M^{+} onto a metal substrate S.

$$S + nM^{+} + ne^{-} \leftrightarrow S.nM_{(ads.)} \quad \text{(XI)}$$

Underpotential deposition translates into a highly promising method for substrate coating that allows the manipulation of substrate morphology without needing the direct synthesis of 3D structures of the active material itself, not only saving the quantity of active material needed for the system but also allowing the creation of other structures that might have not been initially possible with the active material alone. An overall schematic of the monolayer formation onto a metal substrate can be observed in Figure 34.

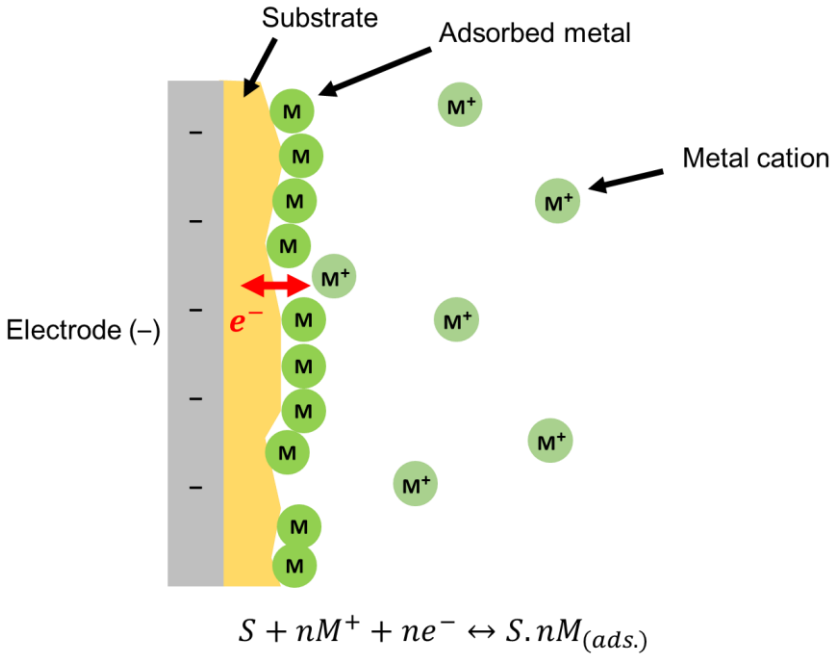

Figure 34 - Underpotential deposition

The study of UPD is mostly aimed towards the functionalization of electrode surfaces and optimization of the least quantity needed of a certain active material for the electrochemical behaviour to occur, rather than focusing on its role in pseudocapacitive energy storage. Known factors that are usually optimized in underpotential deposition studies are: deposition temperature and potential, crystallographic orientation, type and concentration of anions, nucleation, and grain growth [(59)].

2.4.3. Pseudocapacitive electrode materials

Among extrinsic factors such as the nanostructure of electrode materials, it is of utmost importance to understand which materials have intrinsic pseudocapacitance value. Electrode materials research can be divided between the study of nanostructures and composites. Optimizing nanostructures involves the improvement of morphological parameters such as surface area, active sites, and diffusion pathways that highly influence the ions' behaviour in relation to the electrode material, whereas in composites, the research aims at the optimization of electrical conductivity and structural stability [60]. Following next, a review will focus in the materials that exhibit the best properties when used in electrochemical devices: the metal oxides/hydroxides (MOHs).

MOHs are materials of high specific capacitance and electrical conductivity. A wide variety of these metals has been studied in the past decade, the most well-known metals used in electrodes being Ru, Ir, Mn, Ni, Co, Sn, V and Mo [24]. The evaluation of MOHs intrinsic pseudocapacitance cannot be completed if the metal costs are not taken into consideration. Ruthenium oxides (RuO_x), for example, remain heavily studied due to their amazing electrical conductivity, and in fact, RuO_x are believed to be the very first redox pseudocapacitive materials in which rectangular-shaped CV curves have been observed, similarly to capacitors [6]. However, Ru is an expensive metal and, thus, the research has evolved into MOHs based in cheaper metals like Mn, Ni and Co. In his work [61], Yi et al. compared the theoretical capacitances of several metal oxides (Figure 35) which assists in understanding and predicting their remarkable energy storage when used as electrode materials, more than carbon EDLCs whose capacitances are usually ranged around 100 – 300 F/g.

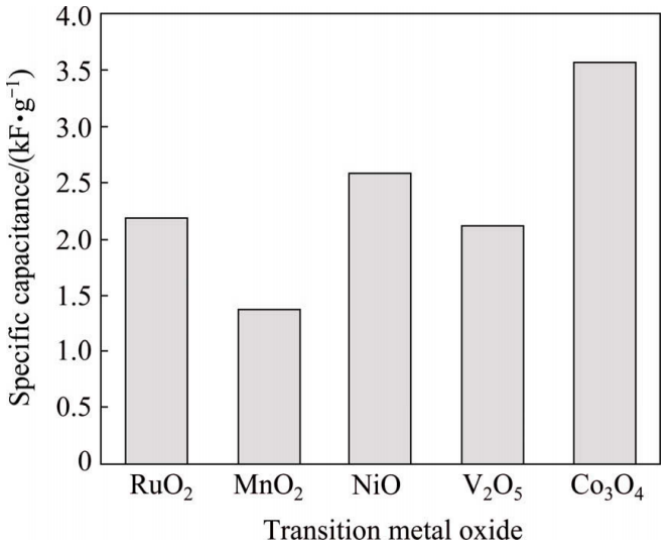

Figure 35 - Theoretical capacitance of different metal oxides [61]

Comparably to battery electrodes, using these metals alone results in morphological challenges as they shrink and swell during the extension of their cycle lives. This is a consequence of the redox

reactions that occur across the active material, reactions (VIII) and (IX), that gradually contribute to the damage of active sites of MOHs nanostructures. This electrode shrinking and swelling compromises the devices ability to store faradaic energy and is considerably common in batteries since the charge process is diffusion-controlled within the bulk of the electrode. Having pseudocapacitive materials exhibiting this hazard behaviour defeats the point of creating a pseudocapacitor altogether if the power and cycling performances are to be as limited as in batteries. Therefore, it is crucial to combine the highly valuable kinetics of MOHs with structurally stable carbon-based materials, like CNTs (as previously seen in Figure 23).

Metal oxides (MOs)

The high capacitance observed in metal oxides is a consequence of the multiple oxidation states that these metals exhibit during proton exchange, which, alongside the fact these redox processes occur in the surface and/or near-surface electrode regions, greatly facilitates ion adsorption [22]. Figure 35 also presents an interesting observation regarding the materials themselves: the most inexpensive metal oxides (nickel and cobalt oxides) exhibit the highest theoretical capacitances. This observation is present in the work [34] of Fisher et al. as well, who also compared the specific capacitances of different metal oxides (Figure 36).

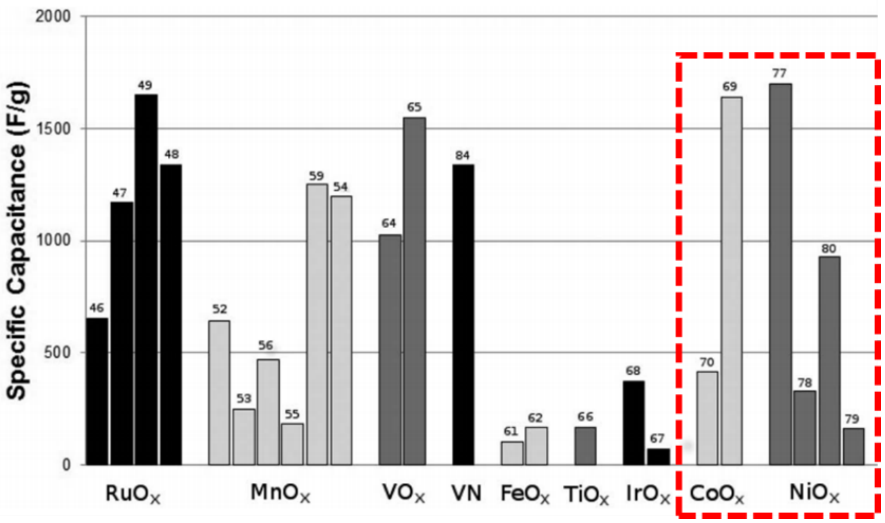

Figure 36 - Specific capacitance of different metal oxides (34)

It is clear from the comparison made by Fisher et al. that ruthenium, cobalt, and nickel oxides are the metal oxides with highest reported capacitance, and hence, the most interesting to explore. To further support the observations made by Fisher et al. (2013), and to better understand the effect that different composite-combinations may result in the capacitance of MOs, a review in this work has been made dedicated to the comparison of multiple capacitance studies of ruthenium, cobalt and nickel oxide

electrodes (Figure 37) with the objective of providing a newer and more diverse insight including the latest articles in the metal oxides (MOs).

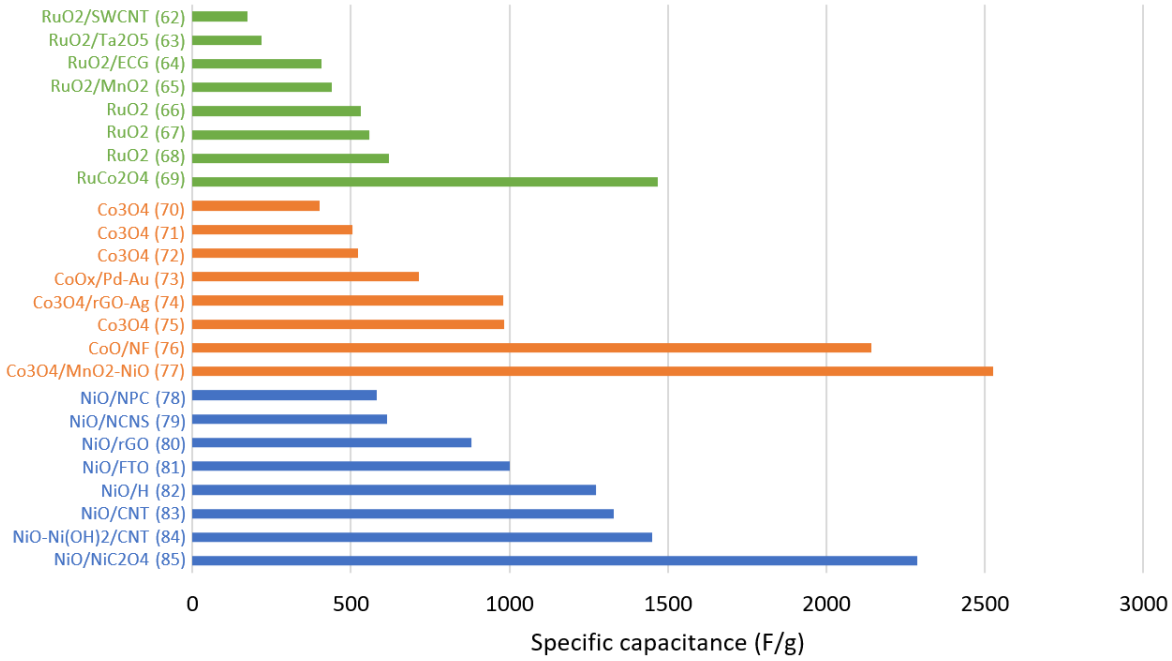

Figure 37 - Specific capacitance of reported studies about Ru, Co and Ni based oxides

As it is evident in Figure 37, even though none of the metal oxides is able to reach as far as their predicted theoretical capacitance states (Figure 35), the recently reviewed literature logically suggests that cobalt and nickel oxides clearly surpass ruthenium oxide capacitance under most conditions. In fact, as it can be observed by the values of reference (77), the best ruthenium oxide result (1469 F/g) is an interesting combination with cobalt which is approximately >100% greater than RuO_2 in its solo electrode oxide form. Therefore, it is hereby suggested that nickel and cobalt oxides are promising options among the known MOs previously mentioned. Nevertheless, it is to be noted that the ultimate choice of which MOHs electrodes should be used is considerably dependent of the operating conditions that the device is intended to be submitted to, as different redox materials exhibit changes of oxidation states at different voltage windows [86].

Metal hydroxides (MHs)

If nickel and cobalt oxides are already promising electrode materials, their hydroxides can go even further. Nickel hydroxide, $Ni(OH)_2$, manages to exhibit a greater theoretical capacitance of 3650 F/g, considerably surpassing its oxide counterpart, NiO_x (~2500 F/g). The amazing specific capacitance of $Ni(OH)_2$ is believed to be deeply related to its loosely crystalline structure, assisting in the intercalation of ions during the charge/discharge process which consequently results in a greater electrochemical

performance [60]. The behaviour of cobalt hydroxide, $Co(OH)_2$, is practically analogous to its nickel counterpart. The two elements are usually seen as electrochemical twins, with similar layered hexagonal nanostructures that are often combined in literature for improved responses [87-90].

As explained in the previous section covering the pseudocapacitive mechanisms, the fast redox pseudocapacitance showcased in MOH electrodes can be conducted in acid or alkaline electrolytes, as well as neutral or nonaqueous. Just like the electrode material itself, choosing the right electrolyte is crucial to ensure the intended electrochemical response. The electrolyte's nature will greatly influence the working potential window of the overall device including its operating lifetime [86]. In contrast to acid electrolytes that often result in unwanted corrosion and damage of electrodes, alkaline electrolytes are the most used in MOHs supercapacitors, KOH usually being the preferred species followed by NaOH and LiOH [91]. The energy storage mechanisms of Ni and Co hydroxides are not entirely understood yet, but Shi et al. [92] exposed two interesting theories concerning the species involved in the change of oxidation states of Ni hydroxide electrodes. One theory states that the charge storage occurs between NiO and NiOOH molecules through reactions (XII) and (XIII).

$$NiO + H_2O \leftrightarrow NiOOH + H^+ + e^- \quad \text{(XII)}$$

$$NiO + OH^- \leftrightarrow NiOOH + e^- \quad \text{(XIII)}$$

Another theory states that the charge storage actually occurs with the middle-term hydroxide, $Ni(OH)_2$, being present through reactions (XIV) and (XV).

$$Ni(OH)_2 \leftrightarrow NiOOH + H^+ + e^- \quad \text{(XIV)}$$

$$Ni(OH)_2 + OH^- \leftrightarrow NiOOH + H_2O + e^- \quad \text{(XV)}$$

Both reaction pairs are accepted and studied in literature, but special attention should be given to the ones that involve hydroxides as reactants and products of the charge storage, given that the spontaneous formation of $Ni(OH)_2$ occurs by combination of water and hydroxyl molecules with NiO [93]. Furthermore, the $Ni(OH)_2$/NiOOH redox pair is known to establish a multi-phase system (Figure 38) that further clarifies the processes happening during the aging and overcharge of a Ni hydroxide electrode, as well as explaining which phases contribute to better specific capacitance (α-$Ni(OH)_2$/γ-NiOOH).

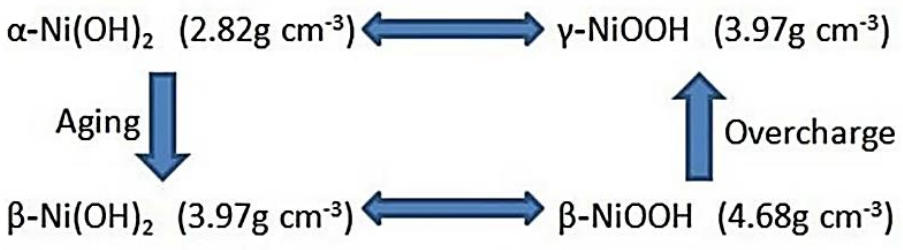

Figure 38 - Phase transformations of $Ni(OH)_2$/NiOOH redox pair [92]

Fully understanding the scope of how these electrode materials react and contribute to energy storage is a challenging task that requires considerable experimental articulation in order to grope the parameters that ultimately define the charge storage mechanisms. In the next chapters, this work will further explore how cobalt hydroxide nanostructures can be synthesized and optimized. Therefore, a clear exposition of the production process of highly segmented nanostructures, the nanofoams, will be conducted with the objective of understanding the crucial parameters involved in their characterization and consequent electrochemical performance.

3. Electrode 3D nanofoams

3.1. From 2D to 3D architecture

When electrochemical energy storage is concerned, the balance between power and energy capacity often converges in the conclusion that electrode surface area is a paramount factor in the achievement of outstanding electrochemical performance. The traditional layout of electrochemical devices consists of an architecture in which the base components of the system (current collector, electrode, electrolyte, and separator) abide to a planar layout where each component is a layer adjacent to another (Figure 39).

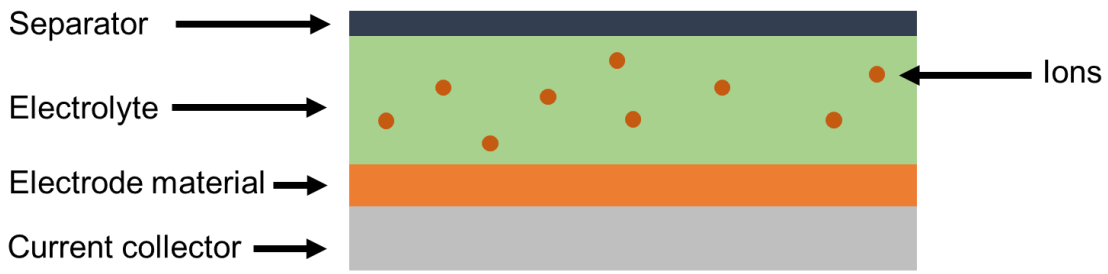

Figure 39 - 2D planar electrode architecture

It has been widely reported that devices with this simple 2D structure result in considerable difficulty in reaching the targeted high performances. Researchers' initial answer to this challenge was synthesising ultra-thin active materials onto the current collectors, which allowed an easier and efficient charge storage. However, the commercial reality of these devices requires a higher mass load than the electrode investigation field usually takes into consideration. Sun et al. have made an interesting review [94] concerning the evolution of electrode's architecture. The higher mass load of commercial assemblies of electrochemical devices results in the overshadowing of the electrode performance due to the passive contribution that the other components of the device have in the overall energy capacity. Therefore, the electrode's mass loads must necessarily increase within the overall mass of the device in order for its contribution to be highlighted. To avoid the consequent decrease of energy capacity that results from thicker electrode materials, charge must be more efficiently delivered across said material (Figure 40).

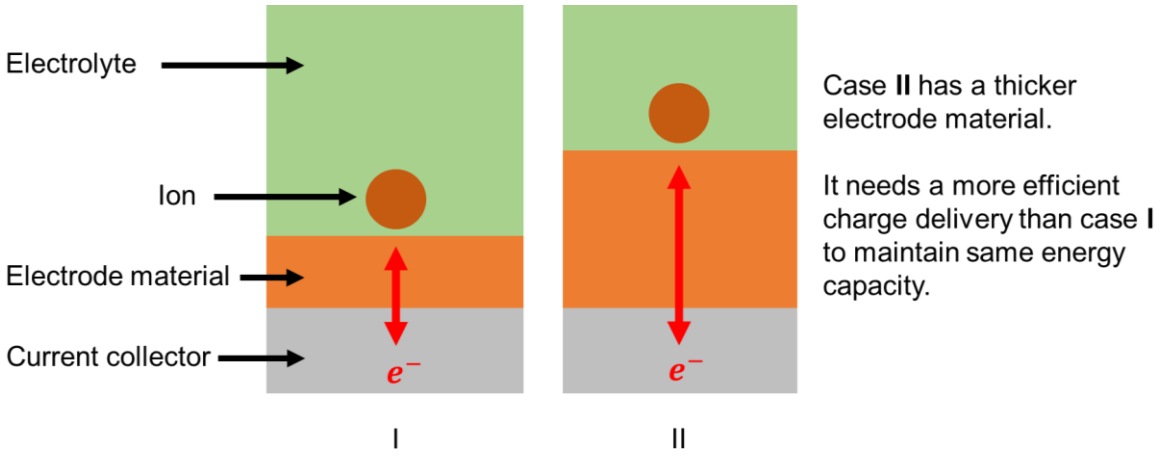

Figure 40 - Influence of planar electrode thickness

The way science addressed this challenge was with the creation of 3D nanostructures which allow access to active sites present within the bulk of the electrode. The development of 3D architectures can vary incredibly depending on the chemical building blocks that are used to synthesize the nanostructures with enough SSA that allows a much more efficient performance of the device. These nanostructures can also be functionalized as current collectors and not directly related to the active material. Metal foams are often used as highly porous 3D current collectors which enable the deposition of interesting active materials such as carbons, polymers, and metal oxides. Metal foams are known to have a higher electrical conductivity than carbon-based 3D structures as well as an easier manipulation of their morphology [95]. Figure 41 depicts a schematical representation of how metal foams can be used as current collectors to support MOH active materials onto its surface.

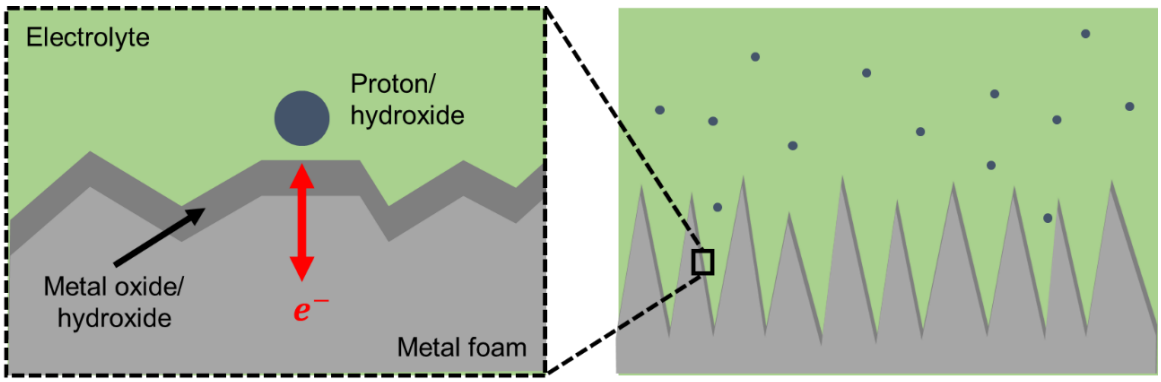

Figure 41 - Metal foam with a metal oxide/hydroxide as active material

With Figure 41 there is an interesting relationship between the electrode's current collector and active material. These two key components of an electrochemical device can be chemically related to the same metal, such is the case of cobalt hydroxide nanofoams. These nanostructures consist of a pure cobalt foam which acts as the metal conductor while its direct hydroxide acts as the active material that will

participate in the pseudocapacitive redox mechanism. Therefore, a pseudocapacitive electrode can be easily built by simply conducting an oxidative treatment of a cobalt nanofoam, thus producing the active material from the metal conductor itself. This is not only an ingenious method of creating 3D electrode materials but also an outstanding way to extensively bind two major components of the device that will greatly facilitates the charge transport phenomena during the electrochemical processes. But before addressing the intrinsic pseudocapacitive character of nanofoams, this work will now explain the process behind the creation of 3D metal nanostructures: electrodeposition.

3.2. Synthesis by electrodeposition

Electrodeposition is a fast and simple method of a metal's deposition onto another metal substrate. This process is practically identical to UPD, covered in the previous chapter, with the exception that electrodeposition occurs at an overpotential voltage, which, in contrast, allows the deposition of several layers of metal ions onto the substrate.

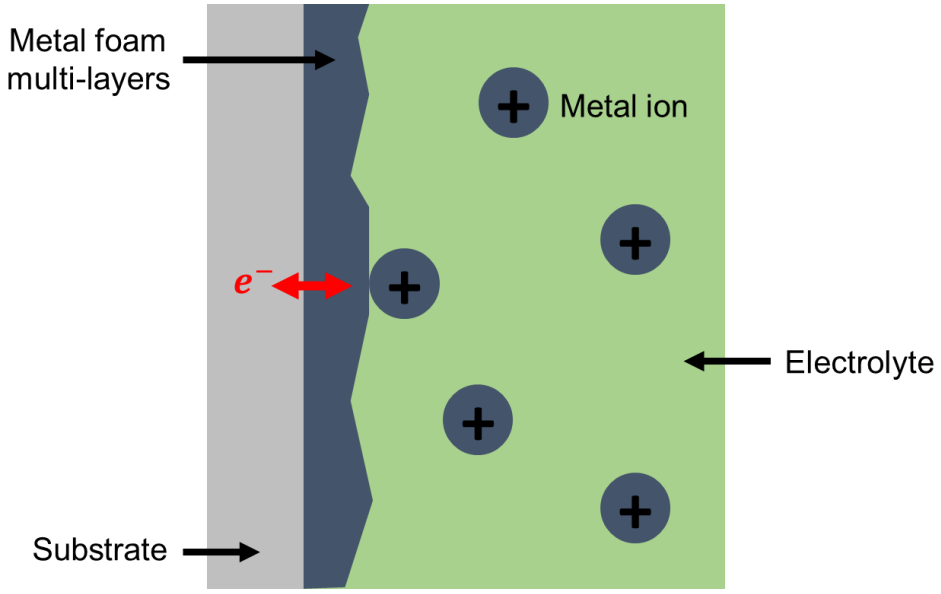

Figure 42 - Electrodeposition

Some nanostructures, such as nanofoams, are synthesized by electrodeposition with high SSA as a result of the series of reactions between metal ions and hydrogen molecules that compete at the electrode's surface. As the solubilized metals deposit onto the substrate, adsorbed hydrogen in its surface (XVI) reacts with the protons in solution to form H_2 (XVII) which will desorb from the metal substrate and diffuse through the metal ions as their deposition occurs simultaneously (XVIII). Reactions (IX) to (XI) contribute to the production of H_2 and the process they define is referred to as *H_2 evolution*, crucial to the formation of highly porous metal nanostructures by utilizing the formation of H_2 at the substrate surface and its following desorption to the solution's bulk as a pathway creator of nano-scale spaces within the depositing metal atoms.

$$H^+_{(aq)} + e^- \rightarrow H_{(ads)} \quad \text{(XVI)}$$

$$2H_{(ads)} \rightarrow H_2 \quad \text{(XVII)}$$

$$M^{n+}_{(aq)} + ne^- \rightarrow M_{(s)} \quad \text{(XVIII)}$$

The production of metal nanofoams by electrosorption is known as dynamic hydrogen bubble template (DHBT). The diffusion of H_2 bubbles creates tunnels that grow from the substrate surface to the bulk of the solution, forcing a porous framework of the deposited metal. Arévalo-Cid et al. (96) experimentally showed the influence of electrodeposition duration in the pore sizes of cobalt nanofoams, suggesting that consecutive layers of cobalt are built with increasing pore size overtime.

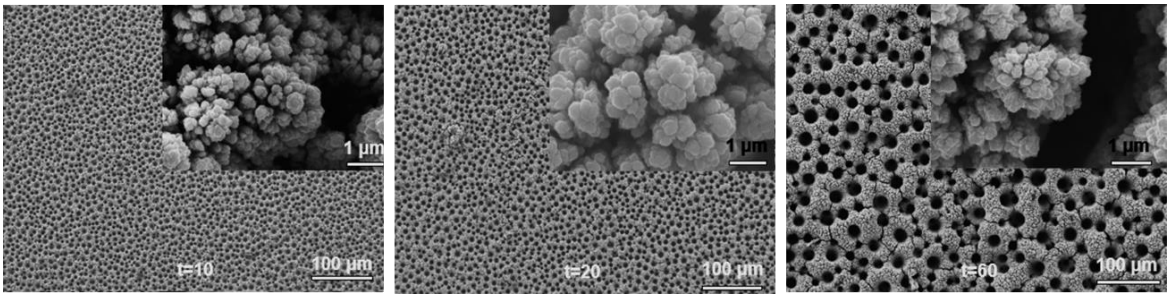

Figure 43 - SEM images of cobalt nanofoams under different deposition times (96)

It can also be observed in Figure 43 that nanofoam synthesis by DHBT results in widely uniform pore distribution with what initially may appear cylindrical geometry. However, and considering that hydrogen is the responsible factor for the circular geometry of the pores, the increasing pore size suggests that the H_2 bubbles increase in size as well, which Arévalo-Cid et al. thereby concluded that this phenomena is a consequence of coalescing hydrogen bubbles (Figure 44) within the metal deposit, resulting in a continuously increasing bubble size as H_2 diffuses farther away from the metal substrate. The presence of this coalescence allows the formation of peculiar tunnels in the 3D structure.

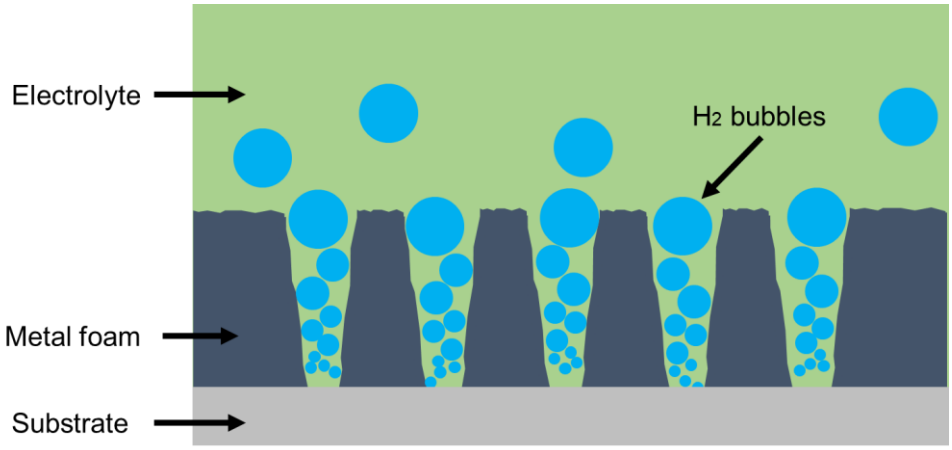

Figure 44 - Influence of H2 coalescence in DHBT electrodeposition

Therefore, electrodeposition time is a fundamental factor of electrodeposition in order to obtain metal nanostructures with the intended pore sizes and depths. The experimental procedure (Figure 45) to produce nanofoams through DHBT electrodeposition is relatively simple by using two electrodes: a working electrode that will support the nanofoam; and a counter-electrode usually made of Pt or Ag.

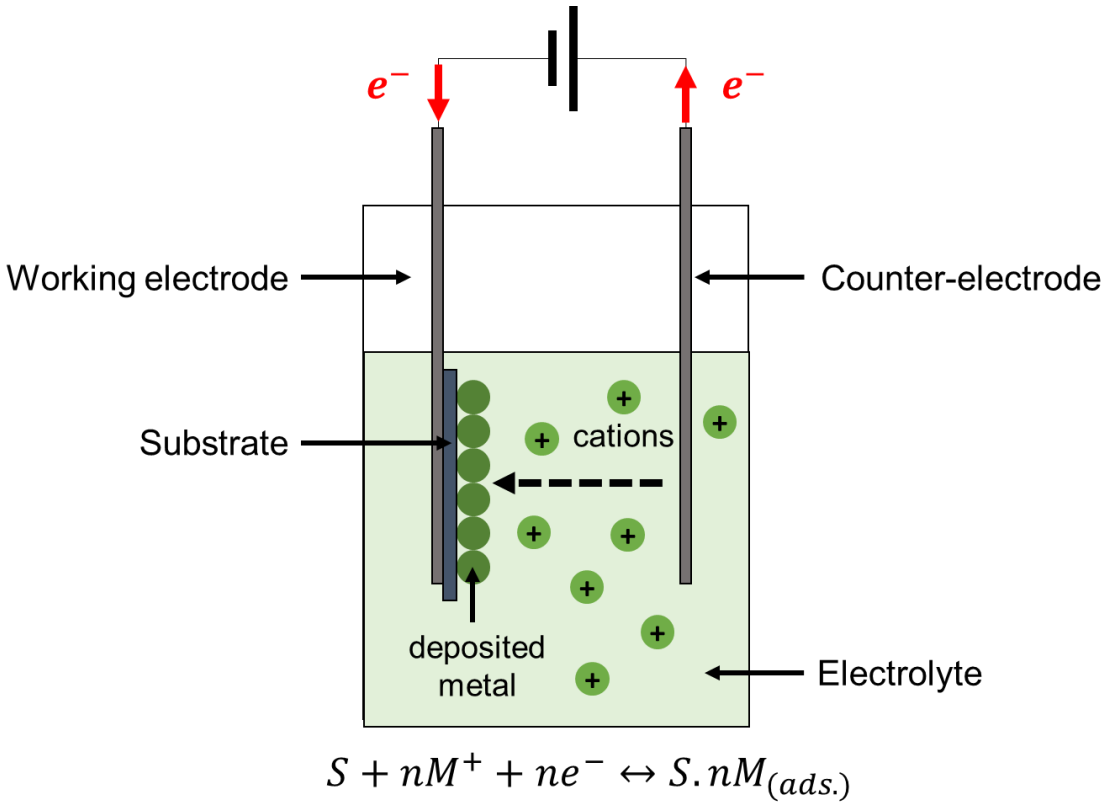

Figure 45 - Experimental setup of DHBT electrodeposition

Thermal treatments are often conducted as a follow up of the electrodeposition process as it can deeply influence the electrochemical behaviour of the electrode. In the work of Naureen, K. [97] an optimization study of Co nanofoams was conducted, and one of the considered factors was the effect of temperature. In Figure 46 (left) , Naureen has demonstrated that the electrochemical behaviour of Co nanofoams can drastically change from pseudocapacitive behaviour to a more faradaic-intensive one, as it can be seen when the temperature, under the conditions experimentally imposed, increases from 200 to 250 ºC.

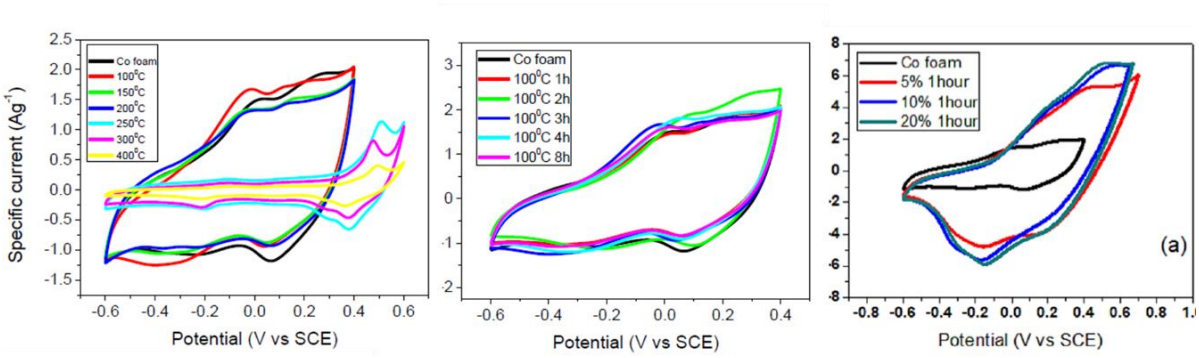

Figure 46 – Thermal and oxidative treatment of Co nanofoams (97)

Complementing the referenced work (97), it is suggested that the increasing faradaic behaviour may be related to the formation of cobalt MOHs which cover the pure metallic nanostructure and create different conglomerates within the 3D architecture. The formation of cobalt oxides at high temperatures decreases capacitance due to the loss of electrical conductivity across the bulk of the nanofoam, thus posing an unwanted influence in the electrochemical response. It is important that the capacitance and integrity of the pure cobalt nanostructure is maintained given that the active phase is often intended to be coated with the active material through an oxidative treatment or by the addition of polymers (even though MOHs result in the highest specific capacitances). Therefore, it is vital for a temperature treatment to be adjusted before a chemical activation can be carried out. Functionalization treatments can result in different electrochemical responses depending on its duration and degree, as seen in Figure 46 for thermal (left graph) and oxidative activation (middle and right graphs of the figure) of cobalt nanofoams.

4. CV simulation in MATLAB

This present chapter is dedicated to the mathematical understanding of the governing mechanisms that create pseudocapacitive electrochemical responses. For this end, computational simulations of cyclic voltammetry were developed in order to observe the current and voltage values as well as the shape of the CV curves and draw conclusions regarding the behaviour of the system. A critical discussion will follow the simulated CV curves to analyse how well or poorly simple mathematical models correlate to reality. Therefore, a comparative study will be presented as well, comparing the curves of simulated and experimentally obtained CV curves.

In order to cover the mentioned objectives, this chapter is hereby organized in three sections:

- **Setup** – exposition of electrochemical models and parameters used.
- **Simulation** – display of simulated CV curves and influence of operating conditions
- **Simulation vs. reality** – comparative study between simulated and empirical data

4.1. Setup

4.1.1. Introduction

Cyclic Voltammetry (CV) is an important method of electrochemical analysis, capable of revealing key characteristic behaviours by quantitative and qualitative interpretation of its curves – cyclic voltammograms. In CV, current is measured across a potential sweep which covers a forward and backward stage across a well-defined voltage window that depends on the nature of the electrode active material. The mathematical relationships between the current and voltage are not straight-forwardly obtained. Other variables such as electrolyte concentration, electron-transfer rate, time, and distance to the electrode's surface are among the main parameters that vary when conducting a CV. It is vital to understand the mathematics between these variables to effectively relate the current with the potential. During a CV test, the behaviour of the active material is tested as the potential sweep enables oxidation and reduction reactions that translate in the charge and discharge mechanisms, respectively. The current work will attempt to simulate the case of energy storage in a cobalt hydroxide electrode.

4.1.2. Potential sweep (ψ vs. t)

The potential sweep, just like it is conducted in the laboratorial execution, varies linearly with time under a specific scan rate (ν) measured in Vs^{-1}. Higher the scan rate, higher the speed at which the experiment's voltage varies. The overall potential sweep will increase from an initial value to a final value upon which the sweep will be reversed (backward sweep) back to the initial voltage value. The minimum and maximum potential, ψ_{min} and ψ_{max}, define the potential window ($\Delta\psi$) and the shape of a potential sweep (Figure 47) can be observed by plotting it in function of time. The total duration of the sweep (t_{CV}) can be trivially obtained with $\Delta\psi$ and ν by using equation [13]. The potential throughout time can then be defined in two domains by equation [14].

$$t_{CV} = \frac{2(\psi_{max} - \psi_{min})}{\nu} \quad [13]$$

$$\psi(t) = \begin{cases} \psi_{min} + \nu t, & t \in \left[0, \frac{t_{CV}}{2}\right] \\ \psi_{max} - \nu t, & t \in \left]\frac{t_{CV}}{2}, t_{CV}\right] \end{cases} \quad [14]$$

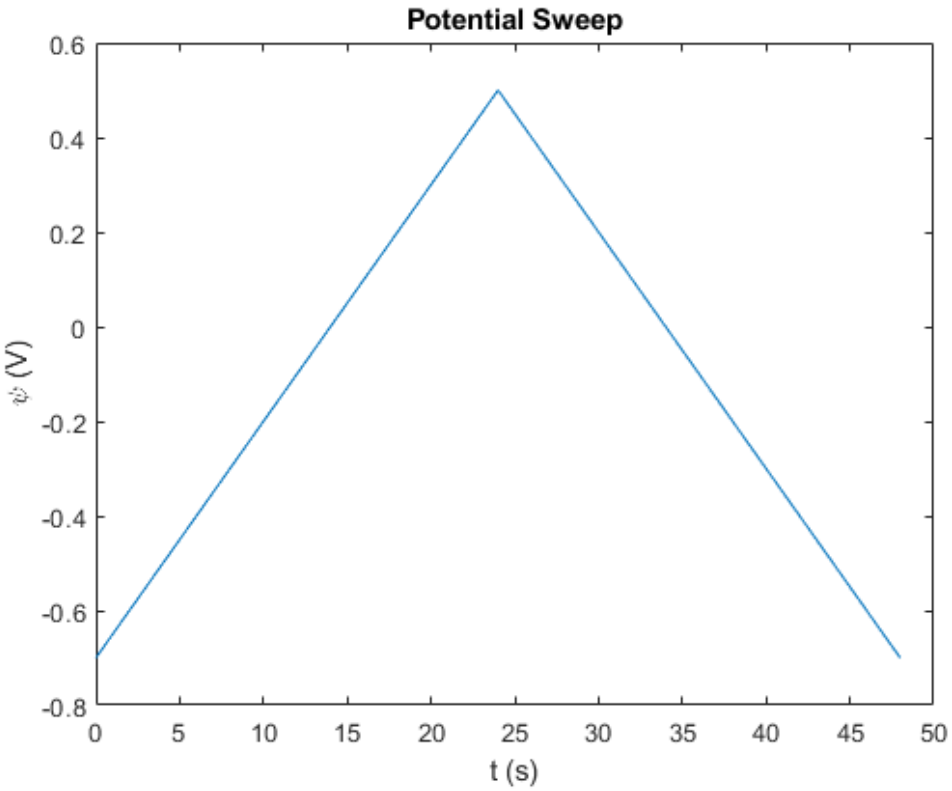

Figure 47 - Simulated potential sweep for a window of 1,2 V and a scan rate of 50 mV/s

The classical triangle-shaped graph (Figure 47) of a potential sweep displays the forward and backward sweeps set by a positive and negative slope (which modules is the scan rate) that intersect in the maximum potential value. With the potential sweep established, it is now pertinent to develop the electrochemical kinetics of the system.

4.1.3. Butler-Volmer kinetics

The Butler-Volmer equation [15] describes the behaviour of current intensity in an electrode with the overpotential present in the system. It is considered to be one of the most important equations in electrochemistry.

$$j_F = j_0 \left[\exp\left(\frac{\alpha z F \eta}{RT}\right) - \exp\left(\frac{-(1-\alpha) z F \eta}{RT}\right) \right] \quad [15]$$

Where j_F and j_0 are the faradaic current density and the exchange current density (A/m^2), respectively, α the system's transfer coefficient, z the number of transferred electrons, R the gas law constant (J/K mol), T the temperature (K), and η the overpotential (V) which can be defined by equation [16].

$$\eta(\psi) = \psi(t) - \psi_0 \quad [16]$$

Where ψ_0 is the equilibrium potential of the system and $\psi(t)$ the potential sweep. There are several inherent parameters inside the Butler-Volmer equation that will vary during the cathodic and anodic reactions of the electrode. These variables will change depending of the order of the reactions occurring at the electrode active material. Therefore, for the system of cobalt hydroxide, the fast and reversible redox reaction (XIX) will be the ruling mechanism of the faradaic response.

$$\mathrm{Co(OH)_2 + OH^- \leftrightarrow CoOOH + H_2O + e^-} \qquad \text{(XIX)}$$

The direct reaction is the oxidation sweep and the inverse is the reduction. It is hereby being assumed that the simulation's system will consist of a cobalt electrode with a cobalt hydroxide active surface that will react with a basic electrolyte as its main energy storage mechanism. The oxidant in the system is the anion $\mathrm{OH^-}$ and the reductant will be water molecules while the electrode's surface will change its composition from $Co(OH)_2$ to CoOOH during oxidation, and vice-versa during reduction. A few further assumptions were made in order to simplify the problem at hand:

- No solid-state diffusion occurs in the bulk of the active material
- The reaction will follow a heterogeneous zero order (i.e. catalytic behaviour)
- There is no secondary reaction or accumulation of species occurring in the system

With these assumptions the problem is thereby initiated with the heterogeneous electron-transfer rate constant, k_0. This approximation is made taking into consideration the surface (and/or, in reality, near-surface) region in which pseudocapacitive redox reactions occur, unlike batteries where the storage mechanism is processed in the bulk of the active material. Therefore, the system is not limited by the concentration of reactants but by the active material itself, generating concentration gradients that will ultimately result in diffusion gradients in the near regions of the electrode surface. The insertion of this constant will further breakdown the Butler-Volmer equation into two analogous terms, one for the oxidation [17] and one for the reduction [18] reaction [98].

$$k_{ox} = k_0 \exp\left(\frac{\alpha z F \eta}{RT}\right) \qquad [17]$$

$$k_{red} = k_0 \exp\left(\frac{-(1-\alpha) z F \eta}{RT}\right) \qquad [18]$$

With varying η, the oxidative and reductive constant rates will change exponentially throughout the duration of the simulation. They will later be used to determine the mass flux at the surface of the active material, but firstly, the concentration gradient of the oxidant and reductant (OH^- and H_2O, respectively) needs to be determined.

4.1.4. Diffusion gradients

The generated diffusion gradients formed in the electrolyte adjacent to the electrode surface will follow Fick's 2nd Law, expressed by [19] and [20].

$$\frac{\partial}{\partial t} = D_{ox} \frac{\partial^2 C_{ox}}{\partial x^2} \quad [19]$$

$$\frac{\partial}{\partial t} = D_{red} \frac{\partial^2 C_{red}}{\partial x^2} \quad [20]$$

Where D_{ox} and D_{red} are the diffusion coefficients of the oxidant and the reductant, respectively, C_{ox} and C_{red} the concentration of oxidant and reductant, respectively, and x the distance of the redox species to the electrode's surface. This differential equation is well-known in chemical engineering and adds to the problem a new dimension, the distance to the electrode. Therefore, the simulation has now two independent dimensions (time and space) that will define the concentration gradients through solving Fick's 2nd Law of diffusion. In his work [98], Brown used a point-cell method to solve the diffusion gradient problem for a binary redox system, aimed at the application of Microsoft Excel for the interpretation of cyclic voltammetry. This work will provide MATLAB simulations coded like the method that Brown applied in Excel, the point method. The point method consists in the approximation of the concentration gradient to a cell-based grid defined by a time and a distance axis. Spatial and temporal indexes were defined as i and j, respectively, and create a cell-grid constituted by those same dimensions (Figure 48). The aim is to conduct a discretization of the differential equation to obtain an expression that will calculate the concentration of a cell based on the prior concentrations in space and time. The discretization of Fick's 2nd Law is presented with expressions [21] and [22].

$$\frac{C_j - C_i}{\Delta t} = D \frac{C_{i-1} - 2C_i + C_{i+1}}{\Delta x^2} \quad [21]$$

$$C_j = C_i + \lambda(C_{i-1} - 2C_i + C_{i+1}) \quad [22]$$

$$\lambda = \frac{D\Delta t}{\Delta x^2} \quad [23]$$

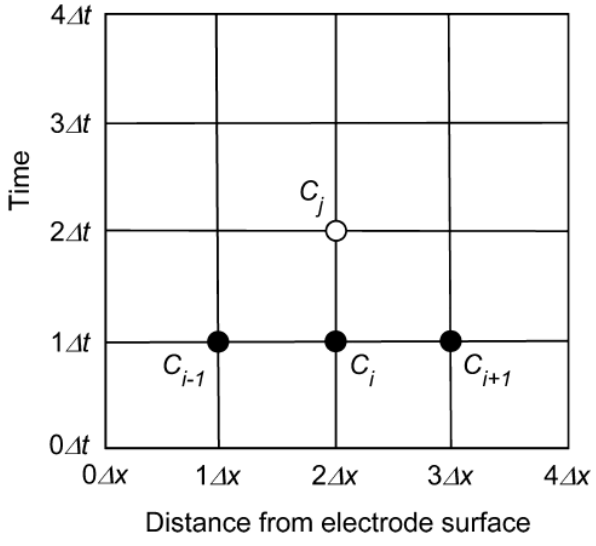

Figure 48 - Point method grid [98]

Equation [22] is the fully discretized form of Fick's 2nd Law of diffusion including the point concentrations presented in Figure 48 and λ (cm^{-1}) as an auxiliary factor [23] that groups up the diffusion coefficient of the species, D (cm^2/s), and the time and distance increments, Δt (s) and Δx (cm), respectively obtained by dividing t_{CV} and L by the total number of increments of those dimensions, n_t and n_x, [24] and [25].

$$\Delta t = t_{CV}/n_t \quad [24]$$

$$\Delta x = L/n_x \quad [25]$$

Equation [23] is applied to both oxidant and reductant concentration gradients by taking initial and boundary conditions that will respectively be the first values used by equation [22]. This system can be observed in Figure 49.

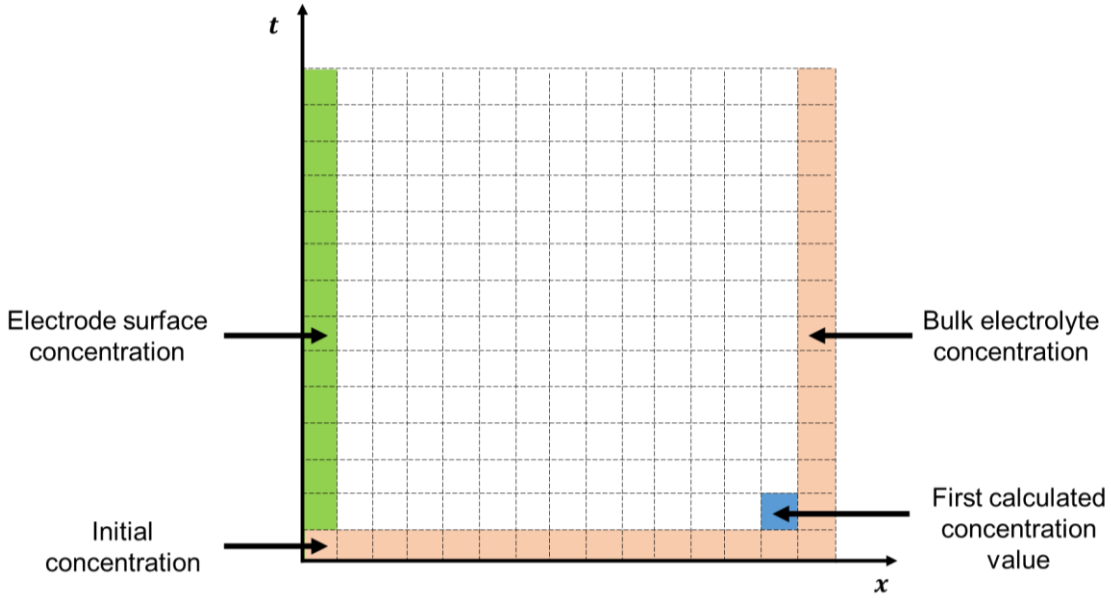

Figure 49 - Concentration grid with initial and border conditions

It is observed in Figure 49 that the point method requires three boundary conditions (first and last column, and bottom row). These conditions are stated below from expression [26] to [29] for both oxidant and reductant concentrations.

$$C_{ox}(x,0) = C_{ox}(L,t) = C_{ox}^{b} \quad [26]$$

$$C_{red}(x,0) = C_{red}(L,t) = C_{red}^{b} \quad [27]$$

$$C_{ox}(0,t) = C_{ox}^{*} \quad [28]$$

$$C_{red}(0,t) = C_{red}^{*} \quad [29]$$

Where C_{ox}^{b} and C_{red}^{b} are the concentrations of the oxidant and reductant at the bulk of the electrolyte, and C_{ox}^{*} and C_{red}^{*} in the electrode's surface, respectively, L being the thickness of the diffuse layer that is calculated with expression [30] which corresponds to six times the distance the species are expected to diffuse during the experiment.

$$L = 6\sqrt{Dt_{CV}} \quad [30]$$

Unlike the initial and bulk conditions, the concentrations at the electrode surface (green column in the figure and explicit by [28] and [29]) are unknown at the start of the simulation. Therefore, the point method will not be able to provide these concentrations and an extra calculation step including the molar flux of the redox species must be conducted afterwards. In order to circumvent this degree of freedom in the system, the fluxes, J_{ox} and J_{red} (mol cm^{-2} s^{-1}) will be rewritten from its classical definition to an expression that includes the available concentrations one distance-increment away of the electrode surface, $C_{ox}(1\Delta x, t)$ and $C_{red}(1\Delta x, t)$.

$$J_{ox} = -\frac{k_{ox}C_{ox}(1\Delta x, t) - k_{red}C_{red}(1\Delta x, t)}{1 + \frac{k_{ox}\Delta x}{D_{ox}} + \frac{k_{red}\Delta x}{D_{red}}} \quad [31]$$

$$J_{red} = -J_{ox} \quad [32]$$

With the fluxes defined, the concentrations at the electrode surface can be further calculated with equations [33] and [34].

$$C_{ox}^{*} = C_{ox}(1\Delta x, t) + \frac{J_{ox}\Delta x}{D_{ox}} \quad [33]$$

$$C_{red}^{*} = C_{red}(1\Delta x, t) + \frac{J_{red}\Delta x}{D_{red}} \quad [34]$$

The flux can be calculated again with the surface concentrations by equations [35] and [36].

$$J_{ox} = -\frac{D_{ox}[C_{ox}(1\Delta x, t) - C_{ox}^{*}]}{\Delta x} \quad [35]$$

$$J_{red} = -\frac{D_{red}[C_{red}(1\Delta x, t) - C_{red}^{*}]}{\Delta x} \quad [36]$$

With the fluxes fully determined in function of the concentration gradients governed by Butler-Volmer kinetics and Fick's 2nd Law of diffusion, the faradaic current density, i_F (A/g) can be finally obtained with equation [37], where m is the mass of the electrode's active material.

$$i_F = -nFSJ_{ox}/m \quad [37]$$

The capacitive contribution of the double-layer effect in the pseudocapacitor can be included and approximated to the behaviour of an ideal capacitor [38] with the sum of the capacitive current density, i_C (A/g) to i_F, obtaining the total current density, i_T, in equation [39].

$$i_C = C\frac{\partial \psi}{\partial t} \quad [38]$$

$$i_T = i_F + i_C \quad [39]$$

4.2. Simulation

4.2.1. Objectives

In this section the models and methods previously explained will be applied in the development of a simulated cyclic voltammogram intended to showcase the electrochemical behaviour of a cobalt hydroxide electrode, typically constructed by DHBT electrodeposition and oxidative functionalization. Once the CV curve is obtained, a comprehensive analysis of the influence of certain parameters over the shape of the voltammogram will be conducted, before the final comparison with a real, experimentally obtained, CV curve of cobalt hydroxide nanofoam is analysed.

4.2.2. Operating conditions

The parameters necessary to conduct the simulation are present in Table 1.

Table 1 - Operating conditions of cobalt hydroxide nanofoam's CV simulation (calc. – calculated value)

Parameter	Definition	Value	Units	Reference
z	Number of transferred electrons	1	-	-
α	Charge transfer coefficient	$0{,}5$	-	-
R	Gas law constant	8.31451	J mol^{-1} K^{-1}	-
F	Faraday's constant	96485	C/mol	-
T	Temperature	$298{,}15$	K	(99)
$\boldsymbol{\psi_0}$	Standard potential	$0{,}25$	V	(99)
$\boldsymbol{\psi_{min}}$	Minimum potential	$-0{,}7$	V	(99)
$\boldsymbol{\psi_{max}}$	Maximum potential	$0{,}5$	V	(99)
$\boldsymbol{\nu}$	Scan rate	$0{,}05$	V/s	(99)
$\boldsymbol{t_{CV}}$	CV duration	24	s	calc. [13]
S	Electrode area	$0{,}154$	cm^2	(100)
m	Mass of $Co(OH)_2$ nanofoam	$0{,}01$	g	(96)
$\boldsymbol{L}$	Diffuse layer thickness	$0{,}3019$	cm	calc. [30]
$\boldsymbol{H}$	Helmholtz layer	1×10^{-7}	cm	(101)
$\boldsymbol{\Delta t}$	Time increment	$0{,}08$	s	calc. [24]
$\boldsymbol{\Delta x}$	Distance increment	$0{,}0062$	cm	calc. [25]
$\boldsymbol{D_{ox}}$	Diffusion coefficient of OH^-	$5{,}27 \times 10^{-5}$	cm^2/s	(102)
$\boldsymbol{D_{red}}$	Diffusion coefficient of H_2O	$2{,}23 \times 10^{-5}$	cm^2/s	(103)
$\boldsymbol{C_{ox}^b}$	Bulk concentration of OH^-	$0{,}001$	mol/cm^3	(99)
$\boldsymbol{C_{red}^b}$	Bulk concentration of H_2O	0	mol/cm^3	(99)
$\boldsymbol{k_0}$	Heterogeneous rate constant	$0{,}01$	cm/s	(104)

The exposed conditions in Table 1 intend to represent the cobalt hydroxide nanofoam system. Although the nanoporous framework is not modelled for the simulation, the assumption that the redox reactions purely occur at the surface of the active material approximates the properties of the nanofoam structure to the simple definition of the electrode surface area.

4.2.3. Simulated Cyclic Voltammetry

Using the models and parameters previously stated, the resulting CV curve for the cobalt hydroxide system was obtained and displayed in Figure 50.

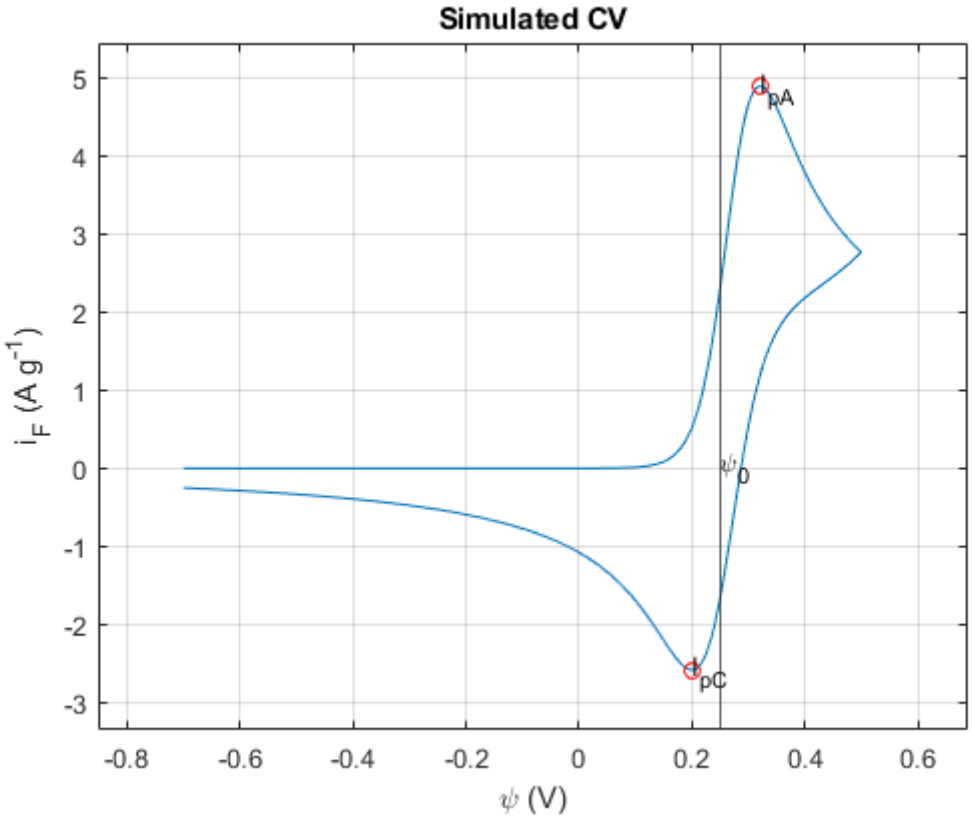

Figure 50 - Simulated CV of the cobalt hydroxide nanofoam system

It is immediately observed two well defined peaks in the obtained CV curve, classic indication of the faradaic behaviour of the system. In Figure 50 the anodic and cathodic current peaks are highlighted by i_{pA} and i_{pC}, respectively defining the oxidation and reduction reactions.

According to the simulated CV curve, the electrochemical response starts, as intended, from the minimum/starting potential (ψ_{min}) of -0,7 V from where the current intensity remains null until a steep increase is noted at 0,5 V. At this stage the active material is behaving as an anode onto which the oxidation is governed by the Butler-Volmer kinetics until it reaches the anodic current peak of 0,32 V

which represents the maximum that the active material is able to oxidize at the given conditions. The once $Co(OH)_2$ covered surface is now fully oxidized into CoOOH as there is no more OH^- being required by the active material to react. With the oxidative step completed, the current intensity will decrease until the potential sweep is reversed or until a secondary oxidation is activated by a higher potential. Considering the construction of this system and its limitations, no more reactions will occur during the forward sweep and the electrochemical response will be diffusion controlled. Upon reaching the maximum/ending potential (ψ_{max}) of 0,5 V, the potential sweep is reversed, and the backward step begins. With the potential now decreasing linearly over time under a constant rate of -ν, the Butler-Volmer kinetics govern again and force the active material to be reduced from CoOOH to $Co(OH)_2$. The current decreases to the cathodic current peak of 0,2 V representing the full reduction of the active material. Analogous to the forward sweep, the backward sweep is then controlled by diffusion and increases gradually as the negative current density increases until the potential reaches ψ_{min} again.

The simulated CV curve displays a marked faradaic redox behaviour which shape, and values, will be later studied and analysed with the objective of understanding their influence in the overall response of the electrochemical system of cobalt hydroxide. The concentration gradients can also demonstrate the behaviour of the redox species across the diffuse layer throughout time and distance to the active material surface. These gradients are represented by Figure 51 and Figure 52 for the oxidant and reductant, respectively.

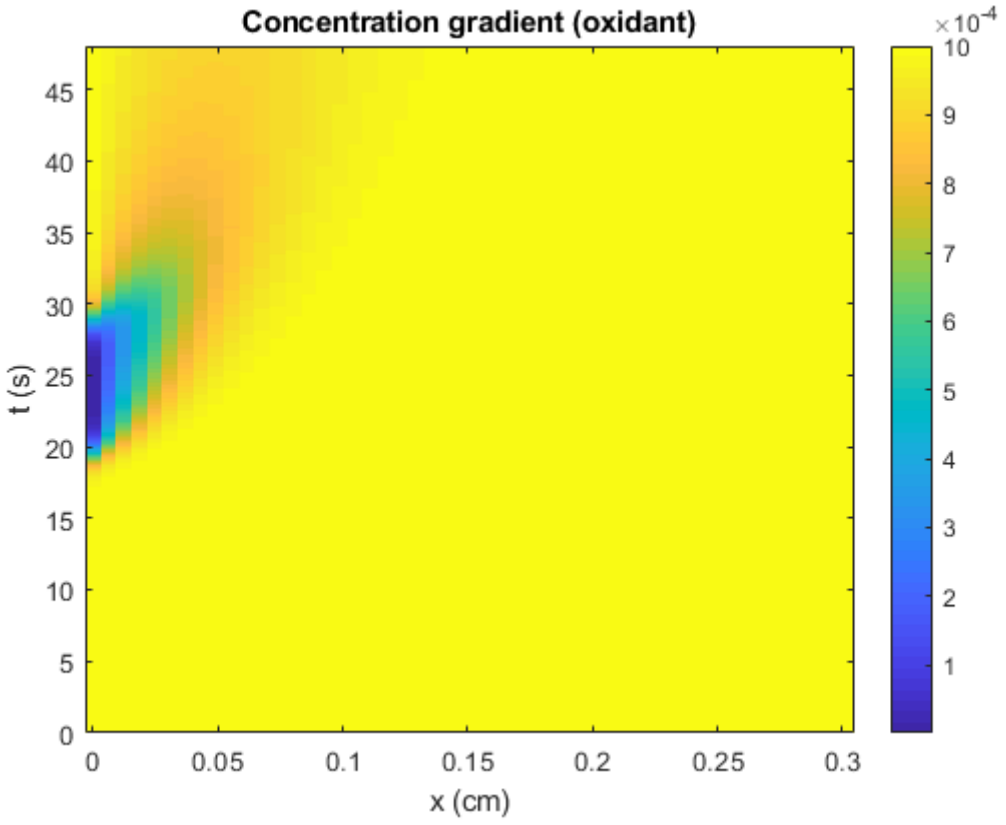

Figure 51 - Simulated concentration gradient of oxidant

It can be immediately observed that the oxidant's concentration changes at the surface of the electrode ($x = 0\ cm$), displaying a coloured stain in the gradient. According to the simulated data of the oxidant at the surface and near surface areas, its concentration remains unchanged over time until the maximum potential is reached, $\psi_{max} = \psi(t = \frac{t_{CV}}{2} = 24\ s)$, concluding the oxidative/forward sweep and after which the reduction begins when the potential decreases and the reductive/backward sweep takes place. This simulates the diffusion of oxidant molecules to the surface of the active material that they oxidize to CoOOH (thus decreasing their concentration) and then being generated again when the active material is reduced back to $Co(OH)_2$. It is a simple comprehensive way of observing how Butler-Volmer kinetics can demonstrate the electrochemical behaviour of a redox couple like $Co(OH)_2$/CoOOH when combined with Fick's 2nd Law of diffusion. The concentration gradient of the reductant occurs in a relatively analogous process to the oxidant's, but with contrary driving force. Considering the different diffusion coefficients that define the diffusion behaviour of the electrolyte species, the gradients will differ slightly in the shape of the coloured stain evidently visible.

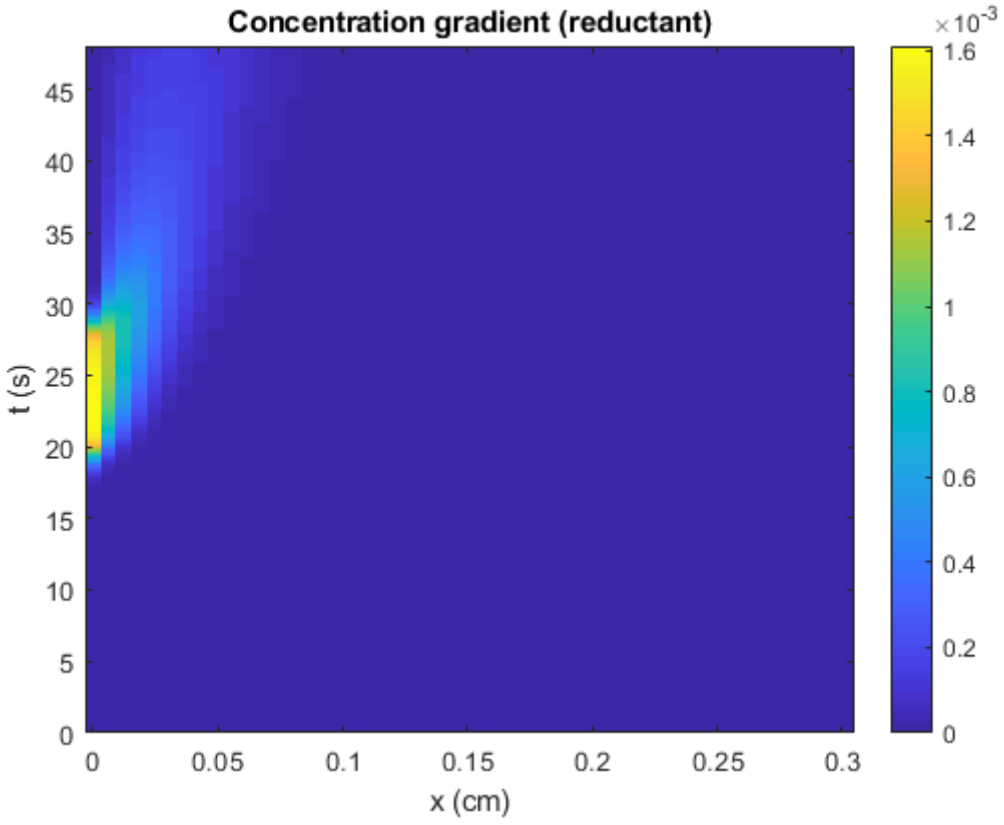

Figure 52 - Simulated concentration gradient of reductant

The concentrations are also displayed across the distance planes in Figure 53 and Figure 54.

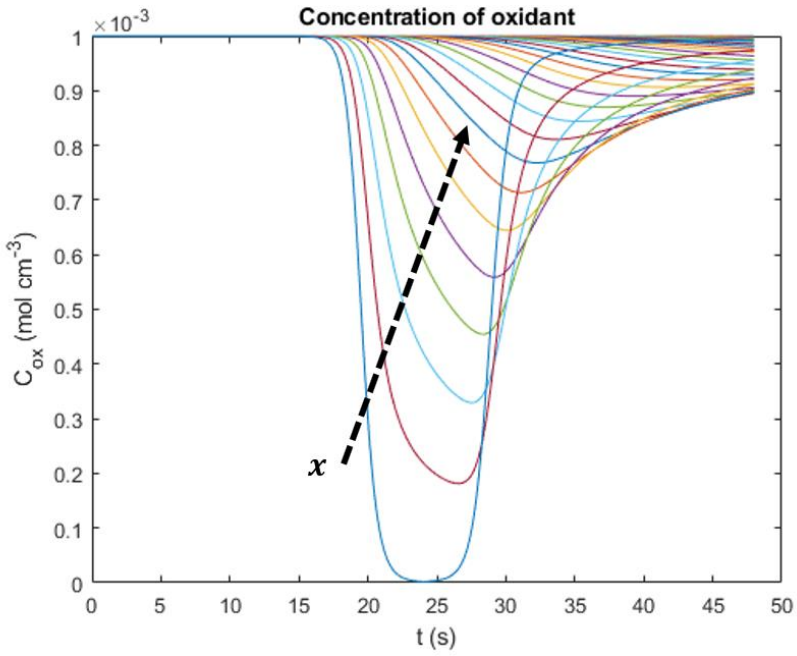

Figure 53 - Concentration of oxidant over time for different distance planes

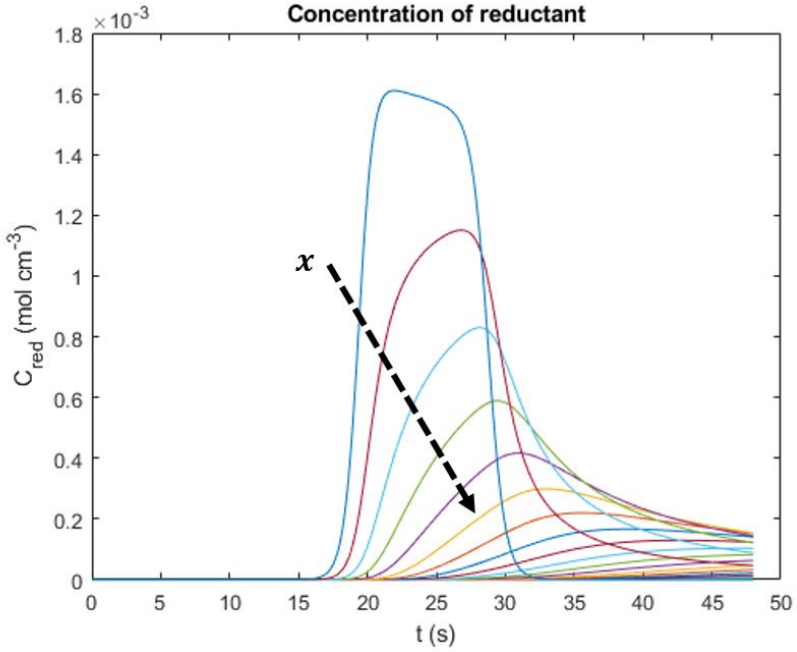

Figure 54 - Concentration of reductant over time for different distance planes

The peaks of each concentration curve correspond to the maximum or minimum of the oxidant and reductant's concentration, respectively, at ψ_{max}. In the case of the oxidant (Figure 53) the minimum concentration is higher as the distance to the electrode increases because the redox processes only occur at the active material's surface or its near surface. The opposite situation occurs for the reductant (Figure 54).

4.2.4. Sensitivity analysis

In this section some of the key ruling parameters (scan rate, temperature and reaction rate constant) of the simulation will be subject to a sensitivity analysis in which they will be varied in defined windows as the electrochemical response of the CV will be observed and conclusions regarding the simulation's approach to reality will be taken.

Scan rate (ν)

Scan rates of 50, 100, 150, 200, 250 and 300 mV/s were imposed in the simulation and the respective CV curves were obtained. The results are present in Figure 55.

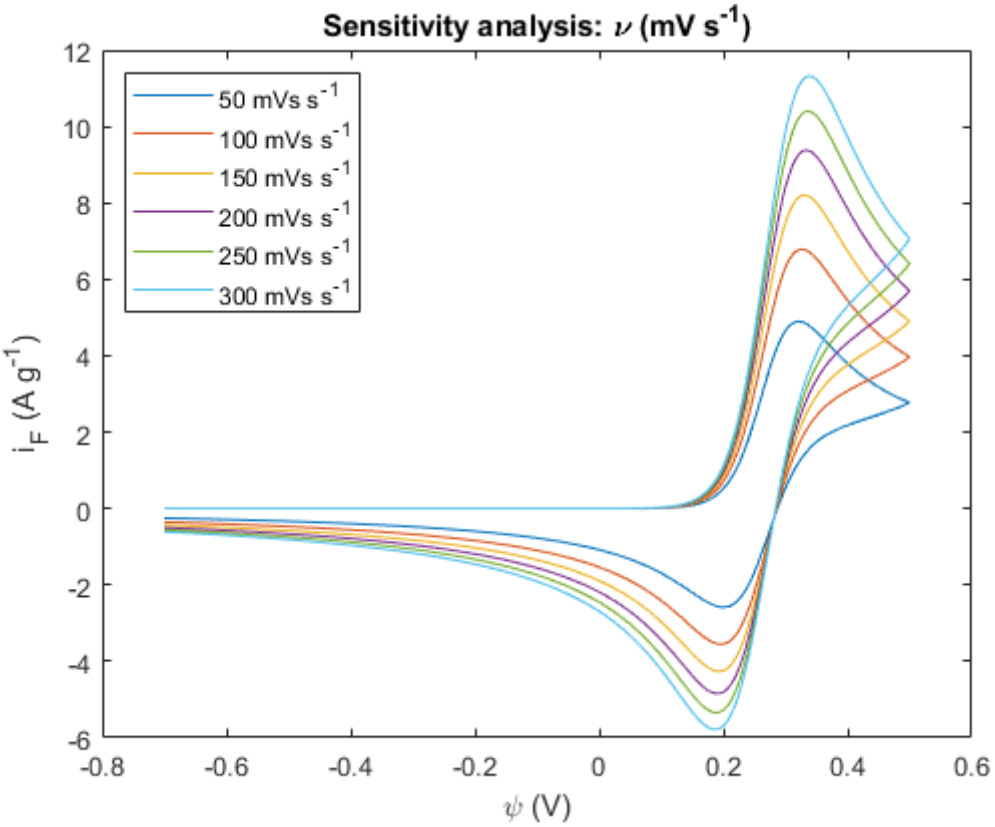

Figure 55 - Sensitivity analysis of scan rate

Increasing scan rates results in more positive anodic current peaks and more negative cathodic current peaks, extending the maximum and minimum of the cyclic voltammograms. This relationship between ν and the current peaks is described by the Randles-Sevcik equation which states that the current peaks are highly dependent on the diffusion properties of the system and of its scan rate.

$$i_p = 2{,}69 \times 10^5 n^{2/3} A D^{1/2} C \nu^{1/2} \quad [40]$$

Randles-Sevcik equation essentially describes that with a higher scan rate the concentration gradient will be higher near the electrode's surface, which abides by the kinetics of Nernst equation. Note that the Nernst equation is not defined in the present simulation setup, but instead, the Butler-Volmer kinetics is. Nernst model is a subset of the Butler-Volmer equation for the particular case of a system in equilibrium. This can be mathematically demonstrated [105] as explicitly shown by the work of Kulikovsky et al.

Temperature

Temperatures of 25, 100, 200, 300 and 400 ºC were imposed in the simulation's parameters and the following sensitivity analysis present in Figure 56 was conducted.

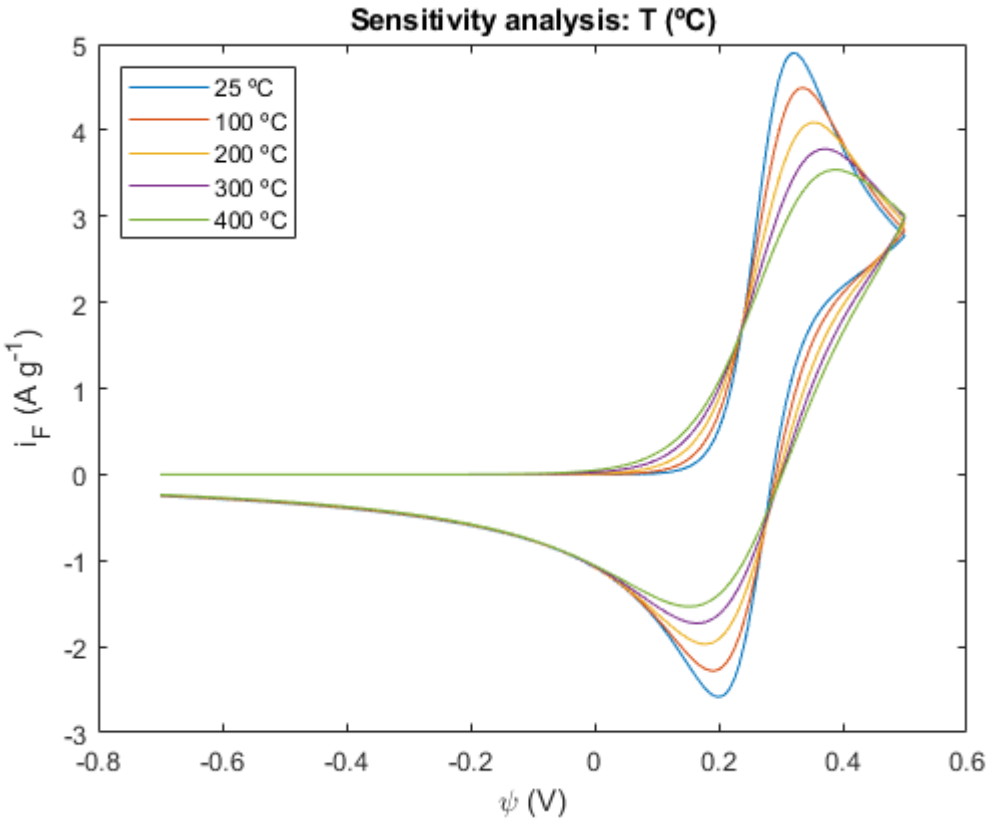

Figure 56 - Sensitivity analysis of temperature

As the temperature increased, the distance between peaks decreased as the CV curves flatten. This behaviour is mathematically expected within the scope of the simulation considering the placement of the temperature term in the Butler-Volmer expressions [17] and [18] that translate in an Arrhenius-type of exponential response that will always decrease with higher temperatures. In an experimental perspective, it is well reported in literature [106] that the increasing temperature will facilitate the overcoming of the activation energy necessary for the exchange of charged species, reducing the

hysteresis of the electrochemical response. This smoothing of the CV curve peaks is noticeable in Figure 56 by the less steep current intensity evolution to the peaks, indicating the involvement of more easily achieved energetic states.

Reaction rate constant

The heterogeneous reaction rate constant was changed from the initial 0,01 to a final 0,0001 cm/s, and the respective electrochemical behaviour of the CV curve was observed in Figure 57.

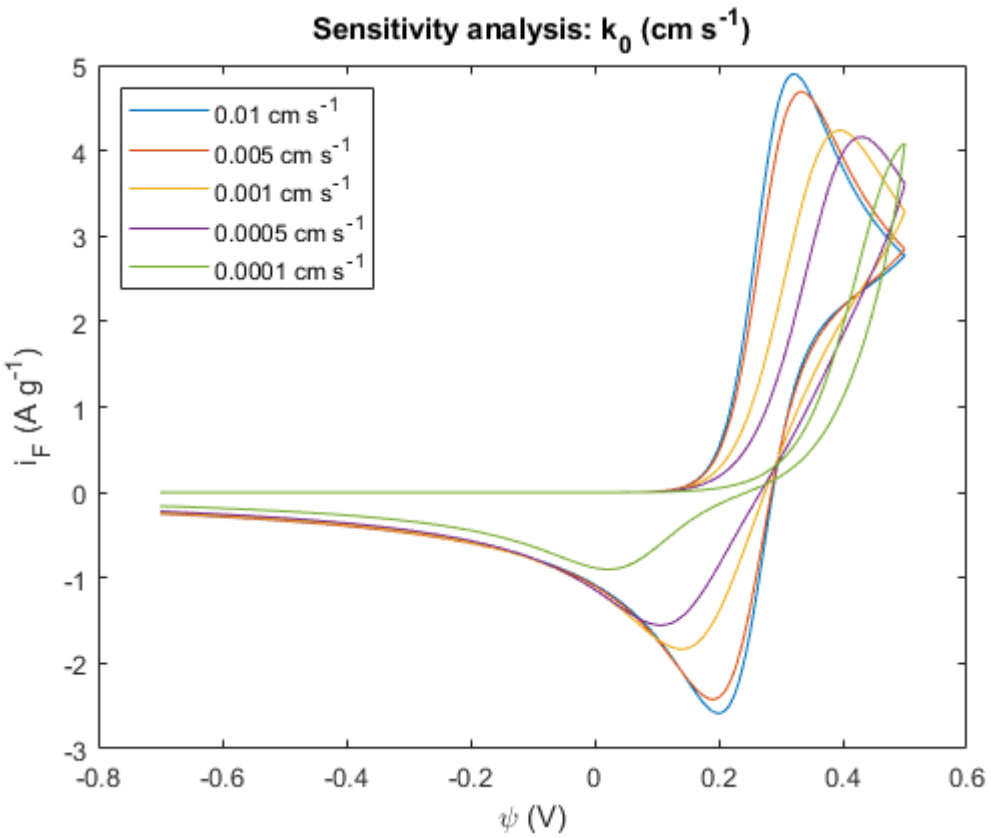

Figure 57 - Sensitivity analysis of the reaction rate constant

The variation of the reaction rate constant resulted in interesting curve shapes which can be summarized with the considerable increase of the distance between the oxidation and reduction potentials as the reaction constant decreases. Slower kinetics result in the oxidation requiring higher potentials in order to be achieved, and in reduction requiring more negative potentials, respectively. It can also be observed that as the module of the current peaks decreases, the rate at which they decrease is slower for the same pace of decreasing rate constants. This suggests that the system has a limit to which the kinetics are so slow that the diffusion is then full dominant of its response, requiring a higher potential window as a consequence of lack of kinetic contribution.

4.2.5. Capacitive behaviour

The double-layer effect is present in every pseudocapacitor as an effect of the charge separation at the electrode-electrolyte interface. To evaluate the EDLC contribution in the system, an extra step of the simulation was added in which the ideal capacitor approximation stated by equation [38] is assumed and the pure EDLC CV curve observed. This curve is present in Figure 59.

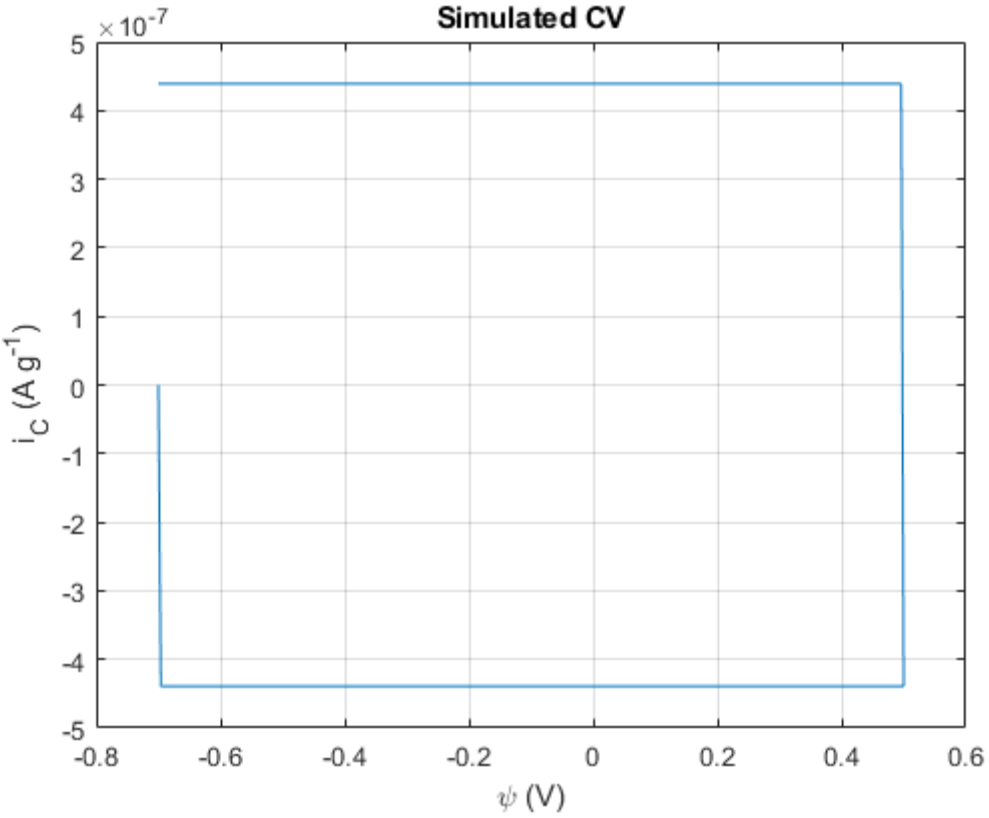

Figure 58 - Simulated EDLC CV curve

The classic rectangular shaped CV curve is clearly observed in the simulation as well as its considerably low contribution. The simulated capacitance is calculated to be approximately 8 μF which falls in line to the expected capacitance range of EDLC contribution in pseudocapacitors. This contribution is not noticed when added to the full simulation of the cobalt hydroxide system, thus neglected.

4.3. Simulation vs reality

4.3.1. Overview

In this section a qualitative comparison between the simulated CV curves and curved experimentally obtained for the cobalt hydroxide nanofoam system will be conducted. The simulation showcased in Figure 50 has approximated inputs (Table 1) that were used in the experimentally obtained CV curve of a electrodeposited (by DHBT method) cobalt nanofoam for 45 s and chemically treated with H_2O_2 before being submitted to a CV test in 1 M KOH at 25 ºC and 50 mV s^{-1}.

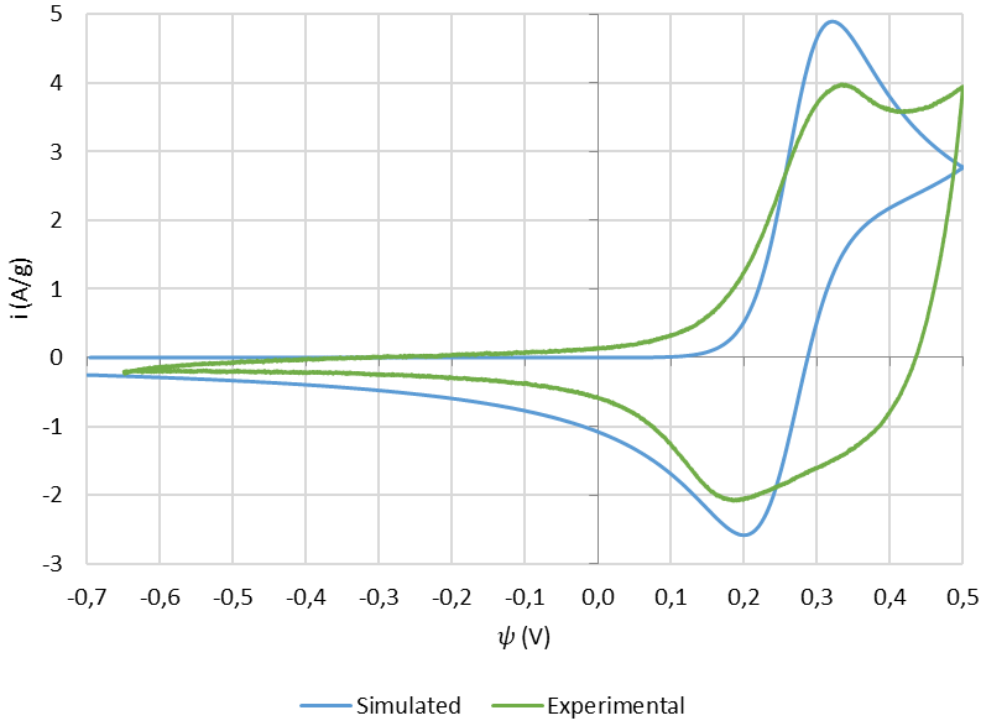

Figure 59 - Simulated and experimental CV curves of the cobalt hydroxide nanofoam system

It is immediately observed that both simulated and experimentally obtained curves share the same potential placement for the cathodic and anodic current peaks at around 0,20 V and 0,32 V, respectively. This suggests that the simulated Butler-Volmer kinetics are a good fit to the real kinetics in nature, respecting the expected $Co(OH)_2$/CoOOH redox potentials. A similar approach to the current peaks is also visible at those potentials, with the distance between peaks being more extensive in the simulated curve than the experimental one. This may have to do with the effectively activated surface of the electrode that participates and enables the redox reactions, usually experimentally obtained through the functionalization methods such as oxidative treatment of the metal foam, as described in the previous chapter. Additionally, the overall area of the experimental curve is considerably wider than the simulation's most likely as a consequence of other diffusion, and possibly other reactions and kinetic

phenomena that are not covered within the simulation model. Unconsidered secondary reactions are also known to occur in these types of pseudocapacitive systems. In fact, the small current peak noticeable at the end of the forward sweep of the experimental curve is possibly related with water electrolysis usually under the form of oxygen evolution reaction (OER). This reaction is essentially the effective oxidation of water under one of possible four mechanisms for alkaline media [107]. Therefore, the addition of the OER was included in the simulation as an extra reaction. According to the Pourbaix diagram of water, for a highly alkaline solution such as the simulation's and experiment's case of 1 M (KOH), the standard potential for the oxidation of water is set at ψ_0 of 0,401 V. The resulting simulation is in Figure 60.

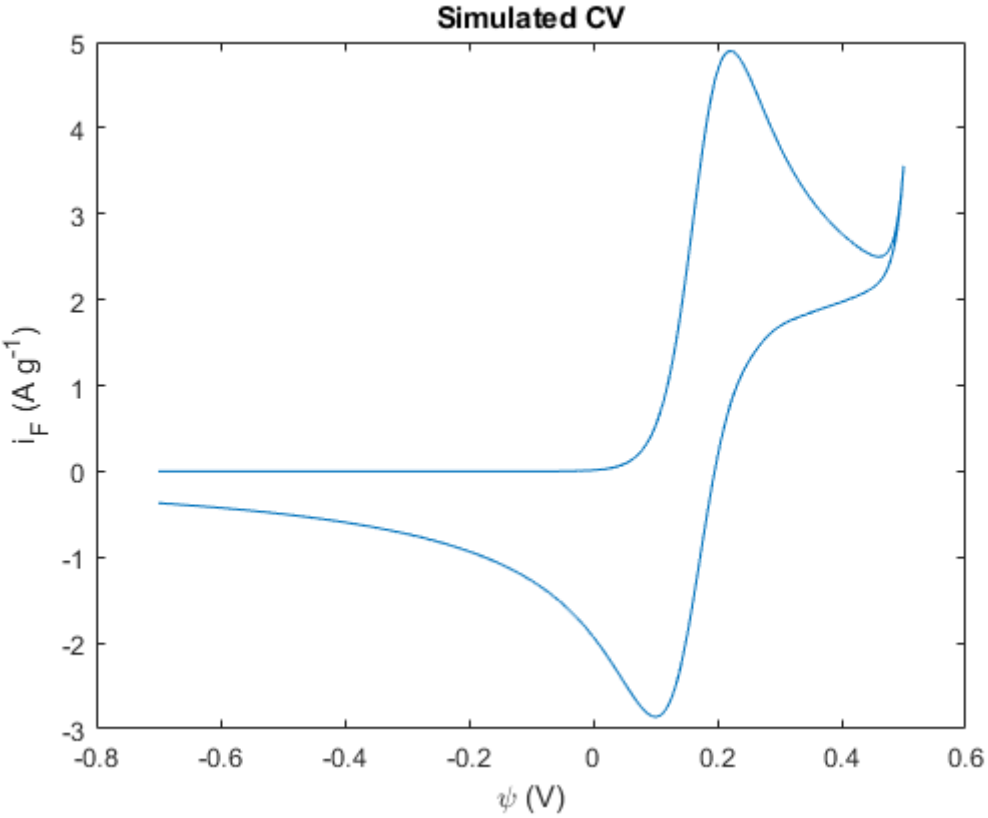

Figure 60 - Simulated CV with the presence of OER considered

The results present in Figure 60 showcase the OER occurring at around 0,4 V as expected. The current density would continue to increase until another peak would be established as the limit of the OER. The simulation can thereby include more than one reaction within its kinetics and diffusion models, contributing to a more accurate representation of the reactions that truly occur in the electrode. It is to be noted that the simulated curve is considerably thinner than the experimentally obtained curve. This indicates the presence of other charged species within the electrolyte contributing with diffusion phenomena that are usually associated with intercalation mechanisms or other processes. It is difficult

to consider the entirety of these processes but not impossible as the simulation's parameters, models, and code can be simpler or more extensive, depending of the system's complexity.

Nevertheless, the cobalt hydroxide nanofoam system can be decently simulated with all the parameters and models previously considered, especially when it comes to pinpoint the placement of the redox current peaks, current density, and potentials.

5. Conclusions

Pseudocapacitors are promising devices capable of placing a new class of electrochemical capacitors in the gap between electrical capacitors and batteries by providing high power and energy capacities alike, creating solutions for a wide range of applications with their continuous research. Furthermore, understanding the energy storage methods of pseudocapacitors is of utmost importance in the academic scope due to the presence of a wide array of mechanisms that can be practically localised in the functioning of every other electrochemical device. Out of the possible conjugation of pseudocapacitive electrodes, MOHs are clearly the pathway of most interest regarding increasing power and energy densities. Furthermore, among these functionalized metals, cobalt and nickel hydroxide electrode materials pose remarkable electrochemical performances considering their more economic value. The use of these metals in nanoporous frameworks extensively increase the performance with their higher surface areas, which with methods such as DHBT electrodeposition allow the synthesis of complex and highly optimized nanofoam structures through an easy and simple process.

By simulating the electrochemical response of a cobalt hydroxide nanofoam approximated system, it has been concluded that the simple mathematical modelling based in the well-known Butler-Volmer kinetics and Fick's laws of diffusion are precise enough to achieve a decent level of accuracy when the pertinent parameters and operating conditions are well defined and adjusted. The simulated CV curves evidenced good accuracy of the current and potential placement of the anodic and cathodic peaks of the system as well as being able to include secondary reactions occurring parallel to the energy storage redox couple such as the OER. The sensitivity analysis of key parameters like scan rate, reaction rate constant, and temperature, demonstrated that the simulation's model abides by the expected behaviour of the CV curve when these parameters are varied.

6. Future work

Future work and research should definitely focus in the optimization of these models towards more accurate reflection of real electrode response by extending to as many processes as are possibly believed and expected to be taking place in an electrochemical cell. Among these processes it is important to highlight the importance of simulating intercalation pseudocapacitance, underpotential deposition, secondary redox reactions (oxidations and reductions occurring inside or outside of the defined potential window) and possible physical and chemical events that influence the diffusion and kinetics of the involved species. To this end, simulation should be focused in understanding the mathematical models that govern these systems and the dominions in which they occur. It is hereby encouraged the use of other discretization methods that simplify and adapt the complex models behind the real processes. Modelling some parameters more thoroughly like the variation of diffusion coefficients with the state of charge is also recommended considering that such treatment will add up to even more accurate simulations.

Bibliografia

1. IEA, Annual storage deployment, 2013-2018, IEA, Paris https://www.iea.org/data-and-statistics/charts/annual-storage-deployment-2013-2018 (access date: 8/10/2020).

2. IEA. (2019) World Energy Investment.

3. IEA, Investment in renewable power, a) Renewable power investment, b) Renewable power investment at constant 2018 costs, 2010-2018, IEA, Paris https://www.iea.org/reports/world-energy-investment-2019/power-sector.

4. IEA, Change in global weighted average capital costs for newly commissioned power capacity, 2010-2018, IEA, Paris https://www.iea.org/reports/world-energy-investment-2019/power-sector.

5. World Energy Council. (2019) Energy Storage Monitor. Latest trends in energy storage 2019 (access date: 8/10/2020).

6. Chen, G. Z. (2016). Supercapacitor and supercapattery as emerging electrochemical energy stores. International Materials Reviews, 62(4), 173–202. doi:10.1080/09506608.2016.1240914. International Materials Reviews.

7. Brousse, T., Crosnier, O., Bélanger, D., & Long, J. W. (2017). Capacitive and Pseudocapacitive Electrodes for Electrochemical Capacitors and Hybrid Devices. Metal Oxides in Supercapacitors, 1–24. doi:10.1016/b978-0-12-810464-4.00001-2 . .

8. https://medium.com/supplyframe-hardware/what-exactly-is-inside-that-capacitor-inside-your-smartphone-computer-or-tesla-270a4ee45e5b (access date: 8/10/2020).

9. https://www.globalspec.com/learnmore/manufacturing_process_equipment/manufacturing_equipment_components/capacitor_assembly_machines (access date: 29.10.2020).

10. Jensen, F., Gudla, V. C., Kongstad, I., & Ambat, R. (2019). High frequency pulse anodising of aluminium: Anodising kinetics and optical appearance. Surface and Coatings Technology, 360, 222–231. doi:10.1016/j.surfcoat.2018.12.117 . .

11. Elabar, D., La Monica, G. R., Santamaria, M., Di Quarto, F., Skeldon, P., & Thompson, G. E. (2017). Anodizing of aluminium and AA 2024-T3 alloy in chromic acid: Effects of sulphate on film growth. Surface and Coatings Technology, 309, 480–489. doi:10.1016.

12. Nickel, D., Dietrich, D., Morgenstern, R., Scharf, I., Podlesak, H., & Lampke, T. (2016). Anodisation of Aluminium Alloys by Micro-Capillary Technique as a Tool for Reliable, Cost-Efficient, and Quick Process Parameter Determination. Advances in Materials.

13. Salman, S. A., & Okido, M. (2013). Anodization of magnesium (Mg) alloys to improve corrosion resistance. Corrosion Prevention of Magnesium Alloys, 197–231. doi:10.1533/9780857098962.2.197.

14. Song, G.-L., & Shi, Z. (2013). Anodization and corrosion of magnesium (Mg) alloys. Corrosion Prevention of Magnesium Alloys, 232–281. doi:10.1533/9780857098962.2.232. .

15. Cipriano, A. F., Lin, J., Miller, C., Lin, A., Cortez Alcaraz, M. C., Soria, P., & Liu, H. (2017). Anodization of magnesium for biomedical applications – Processing, characterization, degradation and cytocompatibility. Acta Biomaterialia, 62, 397–417. doi.

16. Choi, J., Lim, J. H., Lee, S. C., Chang, J. H., Kim, K. J., & Cho, M. A. (2006). Porous niobium oxide films prepared by anodization in HF/H3PO4. Electrochimica Acta, 51(25), 5502–5507. doi:10.1016/j.electacta.2006.02.024.

17. Karlinsey, R. L. (2005). Preparation of self-organized niobium oxide microstructures via potentiostatic anodization. Electrochemistry Communications, 7(12), 1190–1194. doi:10.1016/j.elecom.2005.08.027.

18. Kollender, J. P., Mardare, A. I., & Hassel, A. W. (2017). Direct observation of metal dissolution during anodization of niobium. Electrochemistry Communications, 74, 5–8. doi:10.1016/j.elecom.2016.11.011 . .

19. Narayanan, R., & Seshadri, S. K. (2007). Phosphoric acid anodization of Ti–6Al–4V – Structural and corrosion aspects. Corrosion Science, 49(2), 542–558. doi:10.1016/j.corsci.2006.06.021.

20. Indira, K., Ningshen, S., Mudali, U. K., & Rajendran, N. (2012). Effect of anodization parameters on the structural morphology of titanium in fluoride containing electrolytes. Materials Characterization, 71, 58–65. doi:10.1016/j.matchar.2012.06.005.

21. Delplancke, J.-L., Degrez, M., Fontana, A., & Winand, R. (1982). Self-colour anodizing of titanium. Surface Technology, 16(2), 153–162. doi:10.1016/0376-4583(82)90033-4.

22. Simon, P., & Gogotsi, Y. (2008). Materials for electrochemical capacitors. Nature Materials, 7(11), 845–854. doi:10.1038/nmat2297. Nature Materials.

23. Selvamani, V. (2019). Stability Studies on Nanomaterials Used in Drugs. Characterization and Biology of Nanomaterials for Drug Delivery, 425-444. .

24. González, A., Goikolea, E., Barrena, J. A., & Mysyk, R. (2016). Review on supercapacitors: Technologies and materials. Renewable and Sustainable Energy Reviews, 58, 1189–1206. doi:10.1016/j.rser.2015.12.249.

25. Huang, J., Qiao, R., Feng, G., Sumpter, B. G., & Meunier, V. (2013). Modern Theories of Carbon-Based Electrochemical Capacitors. Supercapacitors, 167–206. doi:10.1002/9783527646661.ch5 . .

26. Dubey, R., & Guruviah, V. (2019). Review of carbon-based electrode materials for supercapacitor energy storage. Ionics. doi:10.1007/s11581-019-02874-0.

27. Vijayakumar, M., Santhosh, R., Adduru, J., Rao, T. N., & Karthik, M. (2018). Activated carbon fibres as high performance supercapacitor electrodes with commercial level mass loading. Carbon. doi:10.1016/j.carbon.2018.08.052.

28. ACs - physical vs. chemical activation 26 Ahmadpour, A., & Do, D. D. (1996). The preparation of active carbons from coal by chemical and physical activation. Carbon, 34(4), 471–479. doi:10.1016/0008-6223(95)00204-9.

29. M, K., AG, K. R., Kaipannan, S., Sundaramoorthy, S., & Marappan, S. (2020). Fascinating the Supercapacitive Performance of Activated Carbon Electrodes with Enhanced Energy Density in Multifarious Electrolytes. Sustainable Energy & Fuels.

30. Gudavalli, G. S., & Dhakal, T. P. (2018). Simple Parallel-Plate Capacitors to High–Energy Density Future Supercapacitors. Emerging Materials for Energy Conversion and Storage, 247–301. doi:10.1016/b978-0-12-813794-9.00008-9.

31. Stout, D. A., Durmus, N. G., & Webster, T. J. (2013). Synthesis of carbon based nanomaterials for tissue engineering applications. Nanomaterials in Tissue Engineering, 119–157. doi:10.1533/9780857097231.1.119.

32. G.F. Kirillova, G.A. Meerson, and A.N. Zelikman, (1960), Kinetics of chlorination of titanium and niobium carbides, Izvestiya vuzov, Tsvetnaya. Metallurgiya., 3, 90–96.

33. Yushin, G., Nikitin, A., & Gogotsi, Y. (2006). Carbide-Derived Carbon. Nanomaterials Handbook. doi:10.1201/9781420004014.ch8.

34. Fisher, R. A., Watt, M. R., & Jud Ready, W. (2013). Functionalized Carbon Nanotube Supercapacitor Electrodes: A Review on Pseudocapacitive Materials. ECS Journal of Solid State Science and Technology, 2(10), M3170–M3177. doi:10.1149/2.017310jss.

35. Gao, G., Pan, M., & Vecitis, C. D. (2015). Effect of the oxidation approach on carbon nanotube surface functional groups and electrooxidative filtration performance. Journal of Materials Chemistry A, 3(14), 7575–7582. doi:10.1039/c4ta07191c.

36. Lee, C., Wei, X., Kysar, J. W., & Hone, J. (2008). Measurement of the Elastic Properties and Intrinsic Strength of Monolayer Graphene. Science, 321(5887), 385–388. doi:10.1126/science.1157996.

37. Lemine, A. S., Zagho, M. M., Altahtamouni, T. M., & Bensalah, N. (2018). Graphene a promising electrode material for supercapacitors-A review. International Journal of Energy Research. doi:10.1002/er.4170.

38. Cortijo-Campos, S., Álvarez-Fraga, L., Gonçalves, G., Vila, M., Álvarez, P., Menéndez, R., … Prieto, C. (2019). In-situ carboxylation of graphene by chemical vapor deposition growth for biosensing. Carbon, 141, 719–727. doi:10.1016/j.carbon.2018.10.033.

39. Zhang, Y., Zhang, L., & Zhou, C. (2013). Review of Chemical Vapor Deposition of Graphene and Related Applications. Accounts of Chemical Research, 46(10), 2329–2339. doi:10.1021/ar300203n.

40. Liu, C., Yu, Z., Neff, D., Zhamu, A., & Jang, B. Z. (2010). Graphene-Based Supercapacitor with an Ultrahigh Energy Density. Nano Letters, 10(12), 4863–4868. doi:10.1021/nl102661q.

41. Li, G., Li, Y., Deng, J., Lin, H., Hou, X., & Jia, L. (2020). Ultrahigh rate capability supercapacitors based on tremella-like nitrogen and phosphorus co-doped graphene. Materials Chemistry Frontiers. doi:10.1039/d0qm00392a.

42. Le Fevre, L. W., Cao, J., Kinloch, I. A., Forsyth, A. J., & Dryfe, R. A. W. (2019). Systematic Comparison of Graphene Materials for Supercapacitor Electrodes. ChemistryOpen, 8(4), 418–428. doi:10.1002/open.201900004.

43. Biesheuvel, P. M., & Dykstra, J. E. (2018). The difference between Faradaic and Non-faradaic processes in Electrochemistry. arXiv: Chemical Physics.

44. Jiang, Y., & Liu, J. (2019). Definitions of Pseudocapacitive Materials: A Brief Review. Energy & Environmental Materials. doi:10.1002/eem2.12028.

45. C. Niu, G. Han, H. Song, S. Yuan, W. Hou, Intercalation pseudo-capacitance behavior of few-layered molybdenum sulfide in various electrolytes, Journal of Colloid and Interface Science (2019), doi: https://doi.org/10.1016/j.jcis.2019.11.107.

46. Thalji, M. R., Ali, G. A. M., Algarni, H., & Chong, K. F. (2019). Al3+ ion intercalation pseudocapacitance study of W18O49 nanostructure. Journal of Power Sources, 438, 227028. doi:10.1016/j.jpowsour.2019.227028.

47. Yoo, H. D., Li, Y., Liang, Y., Lan, Y., Wang, F., & Yao, Y. (2016). Intercalation Pseudocapacitance of Exfoliated Molybdenum Disulfide for Ultrafast Energy Storage. ChemNanoMat, 2(7), 688–691. doi:10.1002/cnma.201600117.

48. Lu, Q.-L., Zhao, S.-X., Chen, C.-K., Wang, X., Deng, Y.-F., & Nan, C.-W. (2016). A novel pseudocapacitance mechanism of elm seed-like mesoporous MoO3−x nanosheets as electrodes for supercapacitors. Journal of Materials Chemistry A, 4(38), 14560–14566. doi.

49. Yoo, H. D., Li, Y., Liang, Y., Lan, Y., Wang, F., & Yao, Y. (2016). Intercalation Pseudocapacitance of Exfoliated Molybdenum Disulfide for Ultrafast Energy Storage. ChemNanoMat, 2(7), 688–691. doi:10.1002/cnma.201600117.

50. Hosseini, H., & Shahrokhian, S. (2018). Vanadium dioxide-anchored porous carbon nanofibers as a Na + intercalation pseudocapacitance material for development of flexible and super light electrochemical energy storage systems.doi:10.1016/j.apmt.2017.11.011.

51. Dong, J., Jiang, Y., Wei, Q., Tan, S., Xu, Y., Zhang, G., … Mai, L. (2019). Strongly Coupled Pyridine-V 2 O 5 · n H 2 O Nanowires with Intercalation Pseudocapacitance and Stabilized Layer for High Energy Sodium Ion Capacitors. Small, 1900379. doi:10.1002/.

52. Fleischmann, S., Zeiger, M., Jäckel, N., Krüner, B., Lemkova, V., Widmaier, M., & Presser, V. (2017). Tuning pseudocapacitive and battery-like lithium intercalation in vanadium dioxide/carbon onion hybrids for asymmetric supercapacitor anodes. Journal of Materials Chemistry A, 5(25), 13039–13051. doi:10.1039/c7ta02564e.

53. Zhu, M., Meng, W., Huang, Y., Huang, Y., & Zhi, C. (2014). Proton-Insertion-Enhanced Pseudocapacitance Based on the Assembly Structure of Tungsten Oxide. ACS Applied Materials & Interfaces, 6(21), 18901–18910. doi:10.1021/am504756u.

54. Yang, P., Sun, P., Du, L., Liang, Z., Xie, W., Cai, X., … Mai, W. (2015). Quantitative Analysis of Charge Storage Process of Tungsten Oxide that Combines Pseudocapacitive and Electrochromic Properties. The Journal of Physical Chemistry C, 119(29), 16483–16489. doi:10.1021/acs.jpcc.5b04707.

55. Jo, C., Hwang, I., Lee, J., Lee, C. W., & Yoon, S. (2011). Investigation of Pseudocapacitive Charge-Storage Behavior in Highly Conductive Ordered Mesoporous Tungsten Oxide Electrodes. The Journal of Physical Chemistry C, 115(23), 11880–11886. doi:10.1021/jp2036982.

56. Han, J., Hirata, A., Du, J., Ito, Y., Fujita, T., Kohara, S., … Chen, M. (2018). Intercalation pseudocapacitance of amorphous titanium dioxide@nanoporous graphene for high-rate and large-capacity energy storage. Nano Energy, 49, 354–362. doi:10.1016/j.nanoen.2018.04.063.

57. Augustyn, V., Come, J., Lowe, M. A., Kim, J. W., Taberna, P.-L., Tolbert, S. H., … Dunn, B. (2013). High-rate electrochemical energy storage through Li+ intercalation pseudocapacitance. Nature Materials, 12(6), 518–522. doi:10.1038/nmat3601.

58. Augustyn, V. (2016). Tuning the interlayer of transition metal oxides for electrochemical energy storage. Journal of Materials Research, 32(01), 2–15. doi:10.1557/jmr.2016.337.

59. Liu, J., Xu, Z., Zhu, B., Du, X., Yang, Y., Yi, C., … Li, J. (2018). Effects of anions on the underpotential deposition behavior of Cu on polycrystalline Pt. RSC Advances, 8(34), 19103–19115. doi:10.1039/c8ra00921j.

60. Shi, F., Li, L., Wang, X., Gu, C., & Tu, J. (2014). Metal oxide/hydroxide-based materials for supercapacitors. RSC Adv., 4(79), 41910–41921. doi:10.1039/c4ra06136e.

61. Yi, C., Zou, J., Yang, H., & Leng, X. (2018). Recent advances in pseudocapacitor electrode materials: Transition metal oxides and nitrides. Transactions of Nonferrous Metals Society of China, 28(10), 1980–2001. doi:10.1016/s1003-6326(18)64843-5.

62. Jha, N., Bekyarova, E., Ramesh, P., Itkis, M. E., & Haddon, R. C. (2013). . Ruthenium oxide - single walled carbon nanotube composite based high energy supercapacitor. International Conference on Advanced Nanomaterials & Emerging Engineering Technologies. doi:10.1109/icanmeet.2013.6609338.

63. Xie, J.-D., Hsu, K.-H., Patra, J., Su, C.-Y., Lee, S.-W., Ashraf Gandomi, Y., … Chang, J.-K. (2020). Hydrous ruthenium oxide-tantalum pentoxide thin film electrodes prepared by thermal decomposition for electrochemical capacitors. Ceramics International. doi:10.1016/j.ceramint.2020.03.236.

64. Xie, J.-D., Patra, J., Muhammad, A. T. I., Gandomi, Y. A., Wu, T.-Y., Lee, S.-W., & Chang, J.-K. (2020). . Graphene induced crystallinity and hydrous state variations of ruthenium oxide electrodes for superior energy storage performance. Electrochimica Acta, 360, 136995. doi:10.1016/j.electacta.2020.136995.

65. Lei, J., & Chen, X. (2015). RuO2/MnO2 composite materials for high-performance supercapacitor electrodes. Journal of Semiconductors, 36(8), 083006. doi:10.1088/1674-4926/36/8/083006.

66. Wang, X., Ruan, D., Wang, P., & Lu, Y. (2008). Pseudo-capacitance of ruthenium oxide/carbon black composites for electrochemical capacitors. Journal of University of Science and Technology Beijing, Mineral, Metallurgy, Material, 15(6), 816–821. doi:10.1016/s1005-8850(08)60293-5.

67. Wang, P., Liu, H., Tan, Q., & Yang, J. (2014). Ruthenium oxide-based nanocomposites with high specific surface area and improved capacitance as a supercapacitor. RSC Adv., 4(81), 42839–42845. doi:10.1039/c4ra07044e.

68. Sugimoto, W. (2014). Ruthenium Oxides as Supercapacitor Electrodes. Encyclopedia of Applied Electrochemistry, 1813–1821. doi:10.1007/978-1-4419-6996-5_511.

69. Dubal, D. P., Chodankar, N. R., Holze, R., Kim, D.-H., & Gomez-Romero, P. (2017). Ultrathin Mesoporous RuCo2 O4 Nanoflakes: An Advanced Electrode for High-Performance Asymmetric Supercapacitors. ChemSusChem, 10(8), 1771–1782. doi:10.1002/cssc.201700001.

70. Cao, L., Zhou, Y., Lu, M., & Li, H. (2003). Preparation of nanocrystalline Co3O4 and its properties as supercapacitors. Chinese Science Bulletin, 48(12), 1212–1215. doi:10.1007/bf03183939.

71. Kalyani M., Emerson R.N. (2018). High-performance Supercapacitor Cobalt Oxide thin films by the Influence of Copper Substrate. International Journal of Pure and Applied Physics.

72. Liu, F., Su, H., Jin, L., Zhang, H., Chu, X., & Yang, W. (2017). Facile synthesis of ultrafine cobalt oxide nanoparticles for high-performance supercapacitors. Journal of Colloid and Interface Science, 505, 796–804. doi:10.1016/j.jcis.2017.06.058.

73. El-Nowihy, G. H., & El-Deab, M. S. (2020). Boosted electrocatalytic oxidation of formic acid at CoOx/Pd/Au nanoparticle-based ternary catalyst. International Journal of Hydrogen Energy. doi:10.1016/j.ijhydene.2020.05.175.

74. Deepi, A., Srikesh, G., & Nesaraj, A. S. (2018). One pot reflux synthesis of reduced graphene oxide decorated with silver/cobalt oxide: A novel nano composite material for high capacitance applications. Ceramics International. doi:10.1016/j.ceramint.2018.08.049.

75. Aloqayli, S., Ranaweera, C. K., Wang, Z., Siam, K., Kahol, P. K., Tripathi, P., … Gupta, R. K. (2017). Nanostructured cobalt oxide and cobalt sulfide for flexible, high performance and durable supercapacitors. Energy Storage Materials, 8, 68–76. doi:10.1016/j.ensm.2017.05.006.

76. Kumar, Y. A., Reddy, A. E., Bak, J.-S., Cho, I.-H., & Kim, H.-J. (2019). Facile synthesis of NF/ZnOx and NF/CoOx nanostructures for high performance supercapacitor electrode materials. RSC Advances, 9(37), 21225–21232. doi:10.1039/c9ra01809c.

77. Singh, A. K., Sarkar, D., Karmakar, K., Mandal, K., & Khan, G. G. (2016). High-Performance Supercapacitor Electrode Based on Cobalt Oxide–Manganese Dioxide–Nickel Oxide Ternary 1D Hybrid Nanotubes. ACS Applied Materials & Interfaces, 8(32), 20786–20792. doi:10.1021/acsami.6b05933.

78. Al-Enizi, A. M., Ubaidullah, M., Ahmed, J., Ahama, T., Ahmad, T., Shaik, S., & Naushad, M. (2019). Synthesis of NiOx@NPC composite for high-performance supercapacitor via waste PET plastic-derived Ni-MOF. Composites Part B: Engineering, 107655. doi:10.1016/j.compositesb.2019.107655.

79. Chen, K., Liu, J., Bian, H., Wei, J., Wang, W., & Shao, Z. (2020). Ingenious preparation of N/NiOx co-doped hierarchical porous carbon nanosheets derived from chitosan nanofibers for high performance supercapacitors. Nanotechnology. doi:10.1088/1361-6528/ab8f4f.

80. Sun, X., Lu, H., Liu, P., Rufford, T. E., Gaddam, R. R., Fan, X., & Zhao, X. S. (2018). A reduced graphene oxide–NiO composite electrode with a high and stable capacitance. Sustainable Energy & Fuels, 2(3), 673–678. doi:10.1039/c7se00420f.

81. Ghalmi, Y., Habelhames, F., Sayah, A., Bahloul, A., Nessark, B., Shalabi, M., & Nunzi, J. M. (2019). Capacitance performance of NiO thin films synthesized by direct and pulse potentiostatic methods. Ionics. doi:10.1007/s11581-019-03159-2.

82. Singh, A. K., Sarkar, D., Khan, G. G., & Mandal, K. (2014). Hydrogenated NiO Nanoblock Architecture for High Performance Pseudocapacitor. ACS Applied Materials & Interfaces, 6(7), 4684–4692. doi:10.1021/am404995h.

83. Lin, P., She, Q., Hong, B., Liu, X., Shi, Y., Shi, Z., … Dong, Q. (2010). The Nickel Oxide/CNT Composites with High Capacitance for Supercapacitor. Journal of The Electrochemical Society, 157(7), A818. doi:10.1149/1.3425624.

84. Hakamada, M., Moriguchi, A., & Mabuchi, M. (2014). Fabrication of carbon nanotube/NiOx(OH)y nanocomposite by pulsed electrodeposition for supercapacitor applications. Journal of Power Sources, 245, 324–330. doi:10.1016/j.jpowsour.2013.06.144.

85. He, D., Liu, G., Pang, A., Jiang, Y., Suo, H., & Zhao, C. (2017). A high-performance supercapacitor electrode based on tremella-like NiC2O4@NiO core/shell hierarchical nanostructures on nickel foam. Dalton Transactions, 46(6), 1857–1863. doi:10.1039/c6dt04500f.

86. Nguyen, T., Montemor, M. de F. (2019). Metal Oxide and Hydroxide-Based Aqueous Supercapacitors: From Charge Storage Mechanisms and Functional Electrode Engineering to Need-Tailored Devices. Advanced Science, 1801797. doi:10.1002/advs.201801797.

87. Salunkhe, R. R., Jang, K., Lee, S., & Ahn, H. (2012). Aligned nickel-cobalt hydroxide nanorod arrays for electrochemical pseudocapacitor applications. RSC Advances, 2(8), 3190. doi:10.1039/c2ra01220k.

88. Huang, L., Chen, D., Ding, Y., Feng, S., Wang, Z. L., & Liu, M. (2013). Nickel–Cobalt Hydroxide Nanosheets Coated on NiCo2O4 Nanowires Grown on Carbon Fiber Paper for High-Performance Pseudocapacitors. Nano Letters, 13(7), 3135–3139. doi:10.1021/nl401086t.

89. Zhang, W., Zhang, X., Tan, Y., Wu, J., Gao, Y., Tang, B., & Wang, Y. (2014). An amorphous nickel–cobalt–boron alloy as advanced pseudocapacitor material. New J. Chem., 38(10), 4666–4669. doi:10.1039/c4nj00912f.

90. Xu, C., Feng, Y., Mao, Z., Zhou, Y., Liu, L., Cheng, W., … Liu, X. (2019). Electronics. doi:10.1007/s10854-019-02313-w, Binary nickel–cobalt metal–organic frameworks as electrode for high performance pseudocapacitor. Journal of Materials Science: Materials in.

91. Carmezim, M. J., & Santos, C. F. (2017). Electrolytes in Metal Oxide Supercapacitors. Metal Oxides in Supercapacitors, 49–78. doi:10.1016/b978-0-12-810464-4.00003-6.

92. Shi, F., Li, L., Wang, X., Gu, C., & Tu, J. (2014). Metal oxide/hydroxide-based materials for supercapacitors. RSC Adv., 4(79), 41910–41921. doi:10.1039/c4ra06136e.

93. Vaidyanathan, S., Cherng, J.-Y., Sun, A.-C., & Chen, C.-Y. (2016). Bacteria-Templated NiO Nanoparticles/Microstructure for an Enzymeless Glucose Sensor. International Journal of Molecular Sciences, 17(7), 1104. doi:10.3390/ijms17071104.

94. Sun, H., Zhu, J., Baumann, D., Peng, L., Xu, Y., Shakir, I., et al. (2018). Hierarchical 3D electrodes for electrochemical energy storage. Nature Reviews Materials. doi:10.1038/s41578-018-0069-9.

95. Yu, Z., Tetard, L., Zhai, L., & Thomas, J. (2015). Supercapacitor electrode materials: nanostructures from 0 to 3 dimensions. Energy & Environmental Science, 8(3), 702–730. doi:10.1039/c4ee03229b.

96. Arévalo-Cid, P., Adán-Más, A., Silva, T. M., Rodrigues, J. A., Maçôas, E., Vaz, M. F., & Montemor, M. F. (2020). On the growth and mechanical properties of nanostructured cobalt foams by dynamic hydrogen bubble template electrodeposition. Materials Characterization, 110598. doi:10.1016/j.matchar.2020.110598.

97. Naureen, K. (2019). Production and Functionalization of cobalt nanofoams for energy storage. Instituto Superior Técnico, Universidade de Lisboa.

98. Brown, J. H. (2015). Development and Use of a Cyclic Voltammetry Simulator To Introduce Undergraduate Students to Electrochemical Simulations. Journal of Chemical Education, 92(9), 1490–1496. doi:10.1021/acs.jchemed.5b00225.

99. Adán-Más, A., Duarte, R. G., Silva, T. M., Guerlou-Demourgues, L., & Montemor, M. F. G. (2017). Enhancement of the Ni-Co hydroxide response as Energy Storage Material by Electrochemically Reduced Graphene Oxide. Electrochimica Acta, 240, 323–340. doi:10.1016/j.electacta.2017.04.070.

100. Santos, Cleverson S.; de Oliveira, Rafaela D.; Marchesi, Luís F.Q.P.; Pessôa, Christiana A. (2018). Electrodeposited cobalt hydroxide in expanded carbon graphite electrode obtained from exhausted batteries applied as energy storage device. Arabian Journal of Chemistry, (), S1878535218302478–. doi:10.1016/j.arabjc.2018.11.017.

101. Brown, M. A., Goel, A., & Abbas, Z. (2016). Effect of Electrolyte Concentration on the Stern Layer Thickness at a Charged Interface. Angewandte Chemie International Edition, 55(11), 3790–3794. doi:10.1002/anie.201512025.

102. Samson, E., Marchand, J., Snyder, K. A. (2003). Calculation of ionic diffusion coefficients on the basis of migration test results. NIST.

103. D.E. O'Reilly, E.M. Peterson. Self-diffusion coefficients and rotational correlation times in polar liquids. II. The Journal of Chemical Physics, Vol. 55, No. 5, 2155–2163 (1971). DOI: 10.1063/1.1676386.

104. Fawcett, W. R., & Opallo, M. (1994). The Kinetics of Heterogeneous Electron Transfer Reaction in Polar Solvents. Angewandte Chemie International Edition in English, 33(21), 2131–2143.

105. Kulikovsky, Andrei A. (2019). Analytical Modeling of Fuel Cells || Fuel cell basics. , (), 1–33. doi:10.1016/B978-0-44-464222-6.00008-3.

106. E. M. Gavilán-Arriazu et al 2020 J. Electrochem. Soc. 167 013533.

107. Wang, F, Shifa, T. A., et al., (2015). Recent Advances in transition metal dichalcogenide based nanomaterials for water splitting. Nanoscale, (), 10.1039.C5NR06718A–. doi:10water splitting. Nanoscale, (), doi:10.1039.C5NR06718A.

108. https://medium.com/supplyframe-hardware/what-exactly-is-inside-that-capacitor-inside-your-smartphone-computer-or-tesla-270a4ee45e5b (access date: 8/10/2020). https://medium.com/supplyframe-hardware/what-exactly-is-inside-that-capacitor-inside-your-smartphone-computer-or-tesla-270a4ee45e5b.

Attachment – MATLAB code

```
%% SIMULATION PARAMETERS

F = 96485;              % Faraday's constant (C/mol)
R = 8.31451;            % gas law constant (J/K.mol)
T = 298.15;             % temperature (K)
m = 0.01;               % mass of electrodeposited active material (g)
A = 0.154;              % area (cm2)
Cbox = 0.001;           % bulk concentration of oxidized species (mol/cm3)
Cbred = 0;              % bulk concentration of reduced species (mol/cm3)
E1  = -0.7;             % start potential (V)
E2  = 0.5;              % end potential (V)
v = 0.05;               % scan rate (V/s)
E0 = 0.25;              % standard potential (V)
n = 1;                  % no. transferred electrons
k0 = 0.01;              % heterogeneous rate constant (cm/s)
alpha = 0.5;            % charge transfer coefficient
Dox = 5.27e-5;          % diffusion coefficient of oxidant (cm2/s)
Dred = 2.23e-5;         % diffusion coefficient of reductant (cm2/s)
nt = 600;               % total time steps
nx = 49;                % total distance steps
ttotal = 2*(E2-E1)/v;   % duration of simulation (s)
dt = ttotal/nt;         % time step (s)
L = 6*sqrt(Dox*ttotal); % max distance from electrode (cm)
dx = L/nx;              % distance step (cm)
H = 1e-7;               % Helmholtz layer (cm)
e0 = 8.854e-14;         % free space permittivity (F/cm)
er = 80;                % relative permittivity of material
S = 1;                  % macroscopic electrode area (cm2)

lambdaOx = (Dox*dt)/(dx^2);     % auxiliary coefficient of oxidized species
lambdaRed = (Dred*dt)/(dx^2);   % auxiliary coefficient of reduced species
```

```
%% SIMULATION TIME

t = zeros(1,nt+1);
t(1)=0;
for j = 2:nt+1
t(j) = t(j-1) + dt;
end
```

```
%% DISTANCE FROM ELECTRODES

x = zeros(1,nx+1);
x(1) = L;
for i = 2:nx+1
x(i) = x(i-1) - dx;
end
```

```
%% POTENTIAL SWEEP

E_e = zeros(1,nt+1);
E_e(1)=E1;
for i = 2:(nt/2)+1
E_e(i) = E_e(i-1) + ((E2-E1)/(nt/2));
end
for i = (nt/2)+2:nt+1
E_e(i) = E_e(i-1) - ((E2-E1)/(nt/2));
end
```

```
%% RATE CONSTANT OF SPECIES

for j = 2:nt+1
kox(j) = k0*exp((alpha*n*F*(E_e(j)-E0))/(R*T));
end

for j = 2:nt+1
kred(j) = k0*exp((-(1-alpha)*n*F*(E_e(j)-E0))/(R*T));
end
```

```
%% CONCENTRATION GRADIENTS

Cox = zeros(nt+1,nx+1);
Cred = zeros(nt+1,nx+1);

for i = 1:nx+1
j = 1; %initial concentration
Cox(j,i) = Cbox;
Cred(j,i) = Cbred;
end

for j = 2:nt+1
i = 1; %bulk or counter-electrode concentration
Cox(j,i) = Cbox;
Cred(j,i) = Cbred;
end

for j = 2:nt+1

for i = 2:nx

Cox(j,i) = Cox(j-1,i) + lambdaOx*(Cox(j-1,i+1)-2*Cox(j-1,i)+Cox(j,i-1));
Cred(j,i) = Cred(j-1,i) + lambdaRed*(Cred(j-1,i+1)-2*Cred(j-1,i)+Cred(j,i-1));

end

Jox(j) = -(kox(j)*Cox(j,nx)-kred(j)*Cred(j,nx))/(1+(kox(j)*dx/Dox)+(kred(j)*dx/Dred));
Jred(j) = -Jox(j);

Cox(j,nx+1) = Cox(j,nx)+(Jox(j)*dx/Dox);
Cred(j,nx+1) = Cred(j,nx)+(Jred(j)*dx/Dred);

end
```

```
%% CURRENT DENSITY

i_F = -n*F*A*Jox/m;
```